Observations of Carbon Monoxide in the Starburst Galaxy M82 with a 690 GHz Wide Spectral Bandwidth Receiver

Thesis by

John Strawn Ward

In Partial Fulfillment of the Requirements

for the Degree of

Doctor of Philosophy

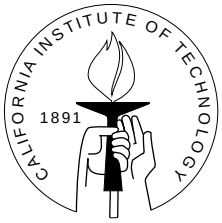

California Institute of Technology

Pasadena, California

2002

(Submitted December 18, 2001)

This thesis is dedicated to my wife, Frédérique,
for her patience and support throughout this long endeavor.

Acknowledgements

First of all, I would like to thank my advisor, Jonas Zmuidzinas, whose thorough understanding of physics from first principles, love of teaching, and general enthusiasm serve as a model that all scientists should seek to emulate.

Other people from Downs Laboratory deserving thanks include Todd Hunter and Dominic Benford, who not only introduced me to the CSO, but also provided the entertainment and camaraderie that made Downs feel like a second home. I thank Tom Phillips for introducing me to submillimeter astronomy. I enjoyed the many conversations we had over breakfast (or was it supper?) at Hale Pohaku. Darek Lis uncomplainingly answered scores of questions about submillimeter astronomy and especially the GILDAS software package. Jacob Kooi introduced me to the basics of microwave amplifiers and noise measurement, and helped with HFSS simulations. I thank David Miller for teaching me so many of the hundreds of techniques required to get anything done in a microwave lab, and for all the wire bonding. Goutam Chattopadhyay was kind enough to fill in many gaps in my physicist's perspective of microwave electronics with sound engineering principles. Mick Edgar's invaluable contribution consisted of daily inquiring, "So, how many pages?" SuperMix would have never seen the light of day if it weren't for the dedication of Frank Rice. Our many hours of heated debate over each and every design detail of the SuperMix library seldom failed to result in something better than either of us could have done separately.

I thank Andy Harris, not only for sharing his spectrometer, but also for his enthusiasm and guidance with submillimeter astronomy. Many were the times when Andy reminded Jonas and me of the reason why we were in an observatory when Jonas and I might have been content to test and fine-tune hardware all night long. I would also like to thank Weiß, Neininger, Hüttemeister, and Klein for providing access to their Plateau de Bure Interferometer data cubes.

Parts of this thesis would not have been possible without the support of several people from JPL. Peter Smith and Lorene Samoska introduced me to QMMICs and showed me how to lay out a mask. John Pearson supported the QMMIC development effort. Sandy Weinreb always found time to answer questions, show me his designs, and offer a lot of good advice about my own. Peter O'Brien spent months fabricating QMMIC substrates in the MDL, keeping an aggressive schedule to finish in time for an observing run at the CSO. Todd Gaier provided the transistors that were used in the amplifiers.

Finally, I would like to thank my parents for instilling in me the love of learning that got me to Caltech in the first place.

This research was supported in part by the NSF CSO grant AST-9980846. The development of the SIS mixers and HEMT amplifiers was supported in part by grants from NASA (NAG5-4890, NAG5-9493), and the NASA/USRA SOFIA instrument program (grant 8500-98-011).

Abstract

A 690 GHz wide spectral bandwidth heterodyne receiver was developed to observe the J=6→5 rotational emission line of carbon monoxide (CO) in extragalactic sources. This receiver is based on a niobium superconductor-insulator-superconductor (SIS) mixer with a twin-slot antenna in a superconducting NbTiN ground plane. A 4-8 GHz low-noise amplifier was developed to amplify the intermediate frequency (IF) signal from the mixer with a spectral bandwidth of 1,700 km/s, enough to comfortably observe the entire emission line of the broadest extragalactic submillimeter sources with a single receiver tuning. This amplifier is a quasi-monolithic microwave integrated circuit (QMMIC); three 160 μm gate InP high-electron-mobility transistors (HEMTs) were bump-bonded to a thin-film GaAs substrate containing passive tuning and DC bias circuitry. The measured amplifier gain is 32 dB and the noise is approximately 8 Kelvin from 4 to 8 GHz at a physical temperature of 4 Kelvin. The complete receiver achieves a measured uncorrected double-sideband noise temperature of 180 Kelvin.

Prior to this development effort, a versatile microwave simulation package was written to calculate and optimize the signal and noise performance of high-frequency circuits, especially those containing superconductors and superconducting tunnel junctions. Using this package, called SuperMix, C++ programs can be written to simulate and optimize circuits of arbitrary size, complexity, and topology. SuperMix was used to simulate the complete 690 GHz SIS receiver.

The receiver was used at the Caltech Submillimeter Observatory (CSO) to map the ^{12}CO J=6→5 emission line in the central kiloparsec of the nearby starburst galaxy M82 at a resolution of 14 arc seconds. Hot spots were found on either side of the dynamical center. A novel deconvolution technique was used to compute a ^{12}CO J=6→5 / ^{12}CO J=2→1 line ratio map based on high-resolution J=2→1 interferometer data. The ^{12}CO J=6→5 map, along with observations of ^{12}CO J=4→3, ^{12}CO J=3→2, ^{13}CO J=3→2, an upper limit for ^{13}CO J=6→5, and five other mea-

sured CO lines from the literature, were analyzed in the context of a two-component large velocity gradient (LVG) excitation model. Likelihood curves were calculated for each of the model parameters as well as a variety of related physical quantities for the two hot spots based on the measured line intensities and their associated uncertainties. This approach reveals in an unbiased way how well various quantities can be constrained by the CO observations. The results of this analysis suggest that the warm gas is less dense than the cool gas, and that over half of the total molecular gas mass in these nuclear regions is warmer than 50 K.

Contents

List of Figures

List of Tables

Chapter 1 Introduction

1.1 A Nearby Starburst Galaxy

On a clear, dark night, the black sky dazzles with thousands of twinkling stars. Stretching from horizon to horizon, the Milky Way winds its way through the constellations. Our sun is only one of about a hundred billion stars that make up the Galaxy, an immense spiral disk we see as the Milky Way. Our Galaxy is in turn only one of the billions of island-universes scattered throughout the vastness of space.

Toward the north, we spot the familiar Big Dipper. Looking above the cup of the dipper with a pair of binoculars, we can find a pair of fuzzy patches about a degree apart in the sky. One of these patches is M82. Figure 1.1 shows these fuzzy patches as viewed with a large amateur telescope. The galaxy on the left, M81, has a spiral structure similar to that of our own Galaxy. M82, on the other hand, has a confused appearance. At a distance of 12 million light years (Freedman et al. 1994), this pair of galaxies may seem vastly far away. But compared to the cosmic microwave background (CMB), which arrives from a distance of about 12 *billion* light years, M81 and M82 can be considered our close neighbors.

When we look at the nighttime sky, we see stars everywhere. We don't see the stuff between the stars. In some parts of the sky, cool, dark clouds of gas and dust are dense enough to block out the light of the stars behind them. These are molecular clouds. With typical densities of thousands or tens of thousands of hydrogen molecules per cubic centimeter, these "dense" clouds are far more rarified than the best vacuum achievable on earth. Yet the molecular gas alone in our Galaxy is billions of times more massive than our sun (Sanders et al. 1984).

Some galaxies have unusually large amounts of gas and dust. M82, a starburst galaxy, is one of them. In some ways a starburst is like a growth spurt. A large reservoir of molecular gas in the central few thousand light years of M82, perhaps

Figure 1.1 Nearby galaxies M81 (left) and M82 (right). Spiral structure can be clearly seen in M81, while M82 has a confused appearance. Gravity binds the two galaxies together despite a separation of over a hundred thousand light years. Imaged with a 32 cm Ritchey-Chrétien telescope, courtesy of Robert Gendler.

10% of the total mass of the region, is rapidly forming new stars. Many of the new stars are massive, hot, and very bright compared to our sun. This starburst can't be sustained because at the current rate of star formation, the molecular gas will be used up in only about 200 million years (Lord et al. 1996). This may sound like a long time, but it is really only a short phase in the life of the galaxy.

1.2 Carbon Monoxide

Astronomers would like to understand galaxies, including how they form and how they evolve. A starburst is an important event in the life cycle of a galaxy, and if we are to understand galaxies, it is critical to understand starbursts. Unfortunately, the dust that is present in all molecular gas obscures the starburst at optical wavelengths. The nucleus of M82 as viewed with the Hubble Space Telescope (Figure 1.2) shows how confused, billowing dust obscures the stars. Most of the tremendous power radiated by the newly formed stars heats the dust and gas and is reradiated in the infrared, making M82 the brightest IR galaxy in the sky.

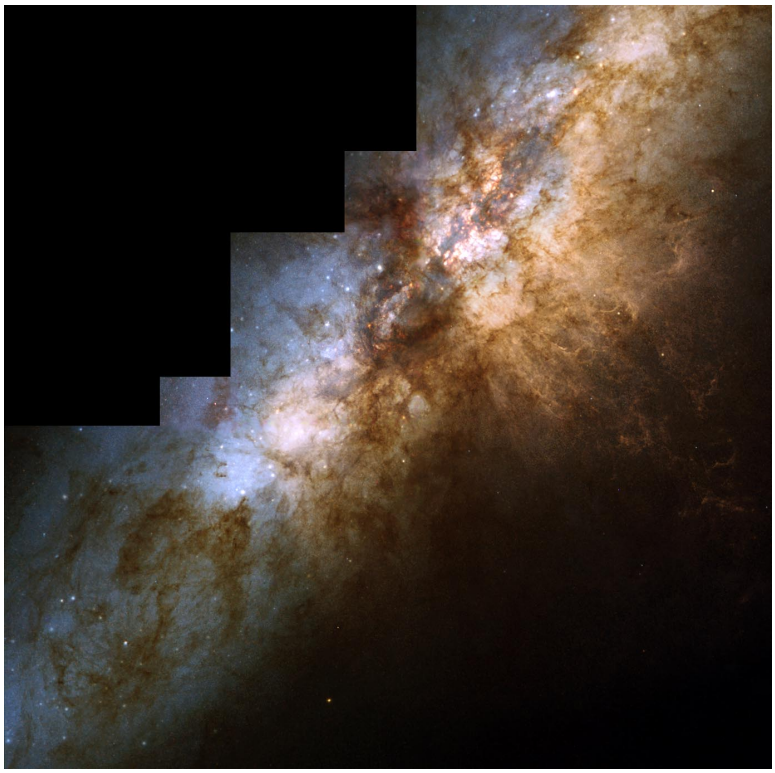

Figure 1.2 The nucleus of M82 as viewed with the Hubble Space Telescope. Image courtesy of NASA, ESA, and R. de Grijs.

Radio waves are much longer than interstellar dust grains, and can penetrate through the dust to allow us to see into the nucleus. We would like to study the gas that is fueling the starburst. Most of the gas in cool molecular clouds is H_2 and He. Because of the symmetry of the H_2 molecule (it has no dipole moment), cool H_2 is nearly invisible. Cool helium gas is also not easily observable. Although CO molecules are 10,000 times less common in molecular clouds than H_2 (Frerking et al. 1982), CO is still the second most abundant interstellar molecule and has the brightest emission lines. For example, we will find in Chapter 6 that the 691 GHz CO emission line radiated by M82 is about as bright as the total power radiated by a million suns.

A carbon monoxide molecule is like a spinning dumbbell. Its angular momentum is quantized such that angular momentum $L = \hbar\sqrt{J(J+1)}$, where J is a non-negative integer. CO molecules in interstellar clouds are typically set spinning by collisions with other molecules, usually H_2. The excited CO molecules can then emit photons

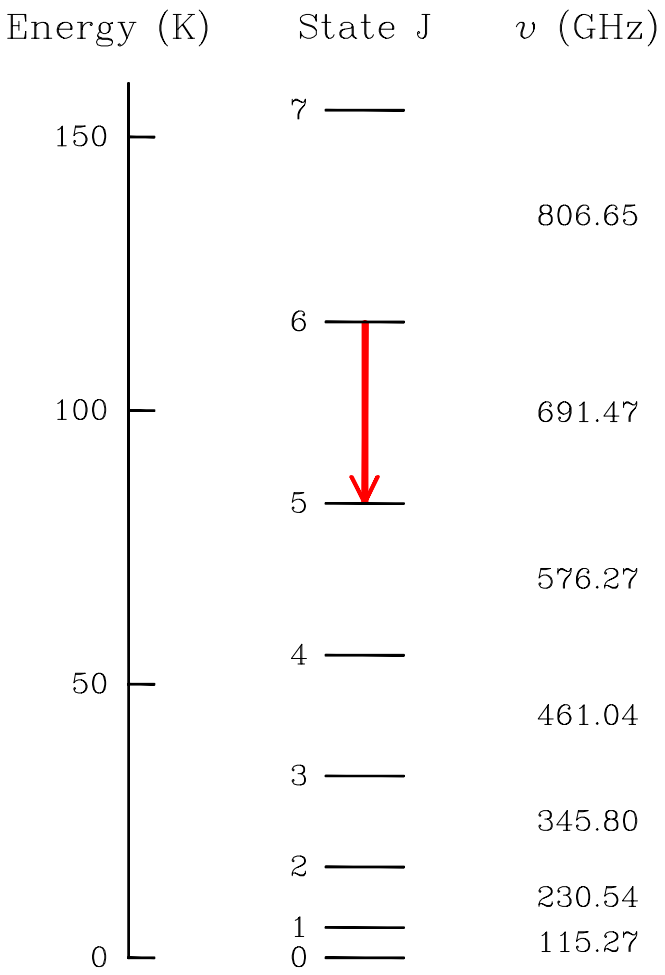

Figure 1.3 Rotational spectrum of carbon monoxide. The energies of the quantum states are expressed in Kelvin by dividing by Boltzmann's constant. The only allowed radiative transitions are for ΔJ=$\pm$1. The J=6$\rightarrow$5 transition is indicated by an arrow.

by decreasing their angular momenta by $\Delta J = -1$. The resulting spectrum has a line every 115 GHz, as shown in Figure 1.3. We refer to the different lines by the initial and final states J. For example, the transition in the figure indicated with an arrow is for the line J=6$\rightarrow$5. It is convenient to express the energies of the quantum states in terms of temperature by dividing by Boltzmann's constant. These temperatures give a rough idea of how warm the surrounding gas (i.e., H_2) must be to excite the CO into the given state. For example, the lower frequency J=1$\rightarrow$0 and J=2$\rightarrow$1 lines are easily excited by cool $\sim$10 K gas, whereas the J=6$\rightarrow$5 line at 691 GHz is excited by gas that is $\sim$50 K or warmer.

Although the initial reason for observing CO is that we can see it, the underlying

scientific justification is more broad. By studying the brightness of several CO lines in a molecular cloud, we can learn about the cloud's temperature, density, mass, and spatial distribution. Finding the temperature of the molecular gas lets us study heating and cooling mechanisms in the galaxy. In particular, we learn about the bright young stars that are heating the gas. The shapes of the lines are determined primarily by Doppler shifts, and give information about the dynamics of the molecular gas. These dynamics, when influenced by gravitational fields, can reveal the mass distribution of all matter in the region. Ultimately, we would like to understand where the gas came from, how stars are formed, and what triggered the starburst.

1.3 Radio Astronomy at 690 GHz

While dolphins play in the last rays of sunshine in Kealakekua Bay and tourists dine at the many beach-side restaurants of Kona, astronomers don gloves, coats, and wool hats to tune high frequency radio receivers at the Caltech Submillimeter Observatory (CSO). The observatory, shown in Figure 1.4, is located near the 4,200 meter (13,800 foot) summit of Mauna Kea on the Big Island of Hawaii. The telescope's 10.4 meter diameter dish was designed to study the heavens at wavelengths shorter than 1 millimeter, corresponding to frequencies above 300 GHz. Humidity is the submillimeter astronomer's greatest enemy since water vapor is opaque to submillimeter radio waves. Despite surrounding oceans and the high humidity of coastal Hawaii, the summit of Mauna Kea is very dry, making it a world-class site for submillimeter astronomy. The atmospheric transmission at the CSO on a good night is shown in Figure 1.5.

The millimeter CO lines (J=1→0 at 115 GHz and J=2→1 at 230 GHz) have been well studied in M82 with both single-dish radio telescopes and interferometers (Sutton et al. 1983; Lo et al. 1987; Shen and Lo 1995; Neininger et al. 1998); see Figure 1.6. The atmosphere is much more transparent in the millimeter lines than in shorter-wavelength transitions like J=6→5, and millimeter receivers are more sensitive. Since ∼10 K gas is sufficiently warm to excite CO into the lowest few

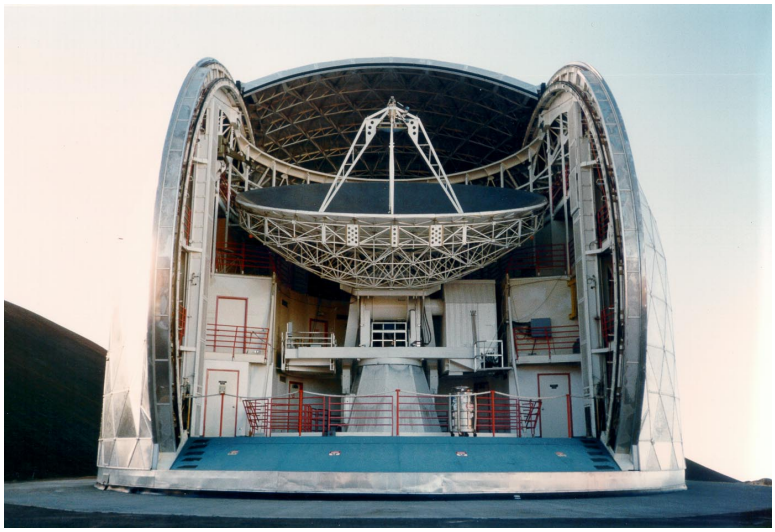

Figure 1.4 The Caltech Submillimeter Observatory near the summit of Mauna Kea in Hawaii. The dish is 10.4 meters in diameter.

rotational quantum states, essentially all interstellar CO emits in the J=1→0 and J=2→1 lines. The advantage of this is that nearly all molecular gas can be observed in the accessible millimeter CO lines. The disadvantage is that it may be difficult or impossible to distinguish warm gas from cool ∼10 K gas based exclusively on millimeter CO observations. Indeed, the relative intensity of the millimeter CO lines in M82 has been a source of substantial discussion (Knapp et al. 1980; Young and Scoville 1984; Loiseau et al. 1990) because it suggests the presence of warm gas but doesn't provide sufficient information to determine the warm-gas characteristics. Observations of the high-J CO lines are a good way to determine these characteristics because the high-J lines are only emitted by warmer gas and thus are not confused by cool-gas emission.

1.4 A Galaxy Receiver

Galaxies are held together by their own gravity. Stars and gas orbit in the gravity well of the galaxy in much the same way that the earth orbits the sun. Rotational velocities in a galaxy are typically hundreds of kilometers per second, creating large Doppler shifts that broaden spectral lines. The CSO has an excellent facility 565-690 GHz

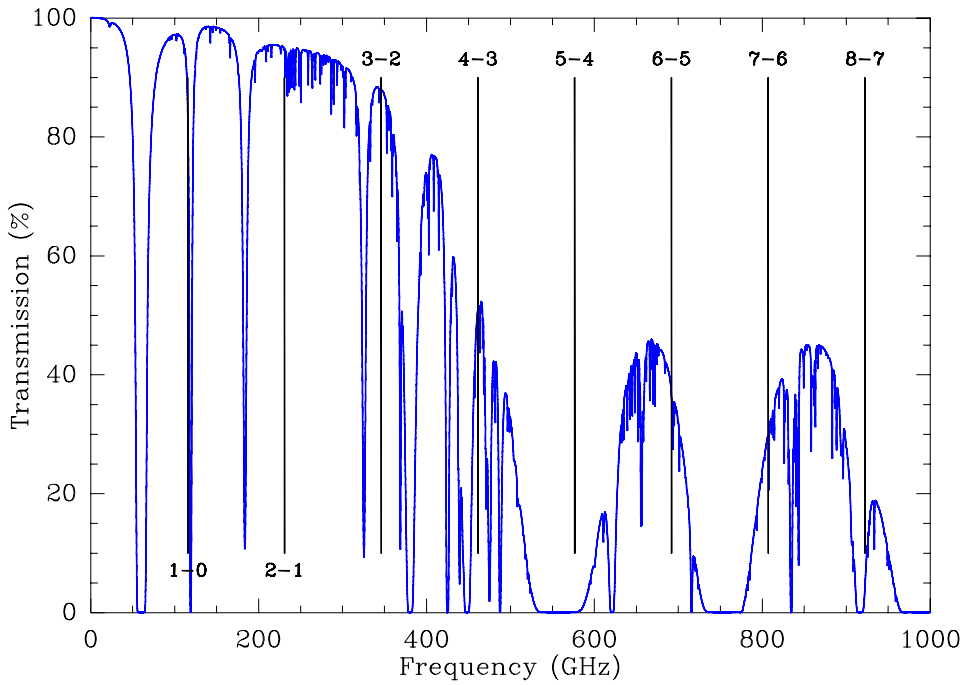

Figure 1.5 Atmospheric transmission at the CSO in very good weather shown with carbon monoxide spectral lines. Transmission of the J=6→5 line at 691.5 GHz is about 35%.

receiver (Kooi et al. 1994), but it is limited to observing 1 GHz of spectrum at a time. To observe a galaxy with this receiver, it is usually necessary to retune the receiver during the observations to observe the line in pieces. Doing so at least doubles the required integration time. Worse yet, optimum calibration requires the observation of substantial baseline on either side of the spectral line to correct for systematic errors in intensity. Observing the line in pieces hampers this correction, drastically decreasing measurement accuracy.

To overcome these problems, I have developed a 690 GHz receiver with 4 GHz of spectral bandwidth to study warm molecular gas in starburst galaxies. Submillimeter waves lie between what is normally thought of as radio waves and optical light. Sometimes submillimeter waves are best treated like optical light, using mirrors and lenses to focus the waves. The 10.4 meter dish at the CSO collects and focuses radio waves in the same way that the primary mirror of an optical telescope focuses light. Additional mirrors focus the radiation into a 4 K cryostat, where two lenses further focus it onto the actual antenna. The superconducting antenna is only 0.15 mm

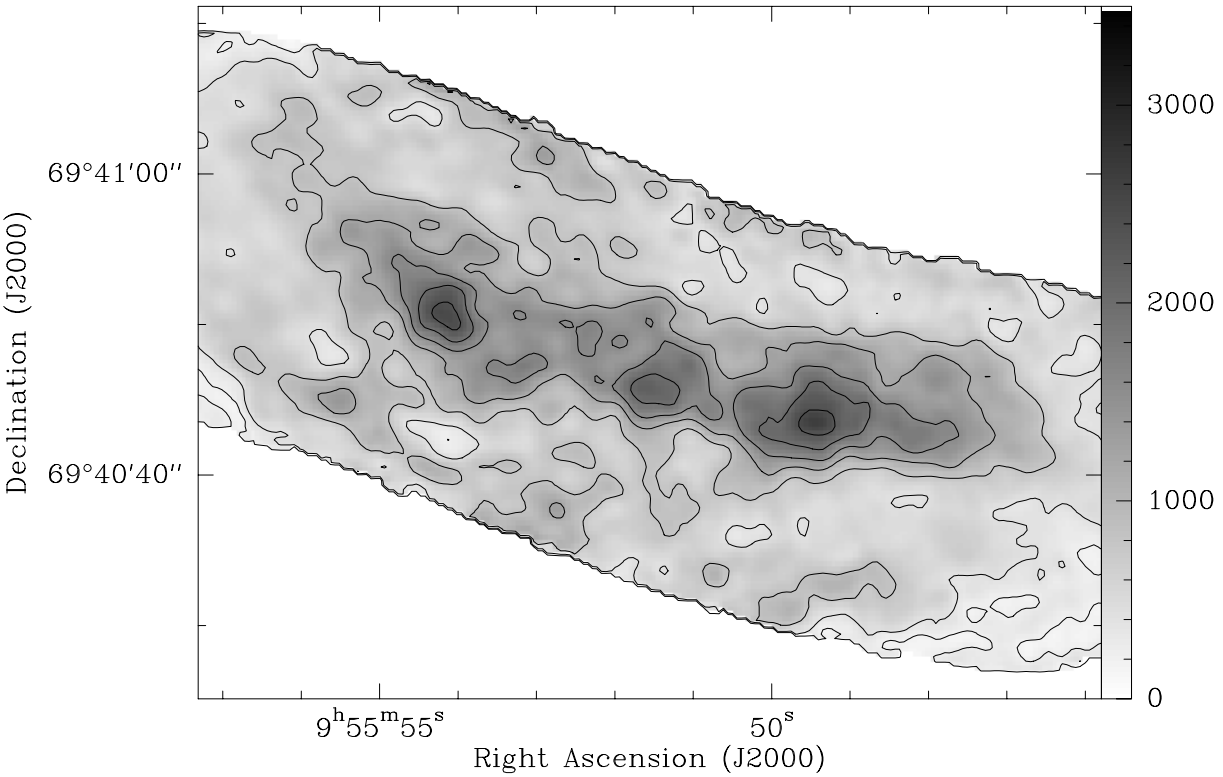

Figure 1.6 Carbon monoxide in M82 at 230 GHz. The integrated intensity is plotted in K km/s. Note the presence of three main bright spots. Courtesy of Axel Weiß.

across. We refer to this system as being "quasi-optical" since it uses a lens to focus the radio waves onto the antenna instead using a feedhorn.

Heterodyne receivers "mix" a sine-wave local oscillator, or LO, with the radio-frequency signal, sometimes called the RF, to reduce the signal to an intermediate frequency, called the IF. For example, a 691 GHz signal can be mixed with a 685 GHz LO to reduce the signal to the difference-frequency of 6 GHz. For this work, superconducting tunnel junctions were used as the mixing elements of the receiver. In a superconductor-insulator-superconductor (SIS) junction, the interaction of quantum tunneling through the insulating barrier with the energy levels of the superconductor creates a very strong nonlinearity in the DC current-voltage (IV) curve. This strong nonlinearity and the low loss of the superconductor enable SIS mixers to function with noise temperatures near the limit that quantum mechanics imposes on all coherent detectors (Tucker and Feldman 1985).

The 4-8 GHz IF signal from the SIS mixer is still very weak. In fact, its power has

been greatly reduced by losses in the atmosphere, telescope, optics, and mixer. At this point, a typical extragalactic signal will be only about a femtoWatt. A low-noise amplifier (LNA) is therefore a critical component needed to boost this signal up to manageable levels. The LNA is run inside the cryostat since amplifiers have optimum noise performance when cooled to very low temperatures and to minimize the loss from cabling between the mixer and the amplifier. The LNA increases the signal power by more than a factor of 1,000 before the signal is brought out of the cryostat through a coaxial cable. The signal is then further amplified and downconverted before being fed into a spectrometer.

1.5 Thesis Overview

Designing an SIS receiver involves substantial calculation. The performance of the antenna, superconducting microstrip impedance transformers, the IF amplifier, and especially mixing in the SIS junctions must all be carefully calculated. The ideal way to do this would be to have a single computer-aided design package to simulate and optimize a complete receiver design. Prior to this work, this was not possible despite a wide variety of excellent commercially available EE computer-aided design programs. In particular, the commercially available packages don't calculate superconductors or SIS junctions. Additionally, few if any of these packages are intended for use simulating circuits at frequencies of hundreds of gigahertz. The first part of this thesis describes a software library called SuperMix that was written to solve this problem. SuperMix can be used to calculate and optimize the signal and noise performance of high-frequency circuits, especially circuits including superconductors and superconducting tunnel junctions. After describing the SuperMix library in more detail and explaining some aspects of how it internally represents and calculates circuits, simulations of a complete 690 GHz SIS receiver including the IF low-noise amplifier will be presented along with measured results for comparison.

I have already shown that a low-noise IF amplifier is a critical component of an SIS receiver, and that the bandwidth of this amplifier should be large enough to

observe an entire emission line with a single receiver tuning. The second part of this thesis describes the development of a 4-8 GHz low-noise amplifier (LNA) for use in the 690 GHz galaxy receiver. Microwave amplifiers are typically based on field-effect transistors (FETs) and are either assembled from discrete components or fabricated as monolithic microwave integrated circuits (MMICs). The amplifier described here is a quasi-monolithic microwave integrated circuit, or QMMIC. Normal MMICs are expensive to fabricate because of very small features in the transistors. The QMMIC puts everything except the transistors on an integrated circuit. Discrete transistors are then bonded to this passive substrate. This approach has most of the advantages of a MMIC, such as giving the designer a high level of control over the details of the circuit and making the amplifiers compact and easy to assemble. At the same time, in small quantities the cost of fabrication is much lower than for MMICs because the substrates don't include any transistors. The measured gain of the amplifier described here is 32 dB, and noise is approximately 8 Kelvin from 4 to 8 GHz.

The third part of this thesis describes the 690 GHz galaxy receiver. This quasi-optical receiver uses a niobium SIS mixer with a twin-slot antenna in a superconducting NbTiN ground plane to achieve a measured double-sideband noise temperature of 180 K. With a 4-8 GHz QMMIC LNA as the IF amplifier, the receiver has a spectral bandwidth of 1,700 km/s, enough to comfortably observe the entire emission line of the broadest extragalactic submillimeter sources with a single receiver tuning. I present simulations of the receiver, and compare them to the measured performance. I also discuss the impedance the SIS mixer presents at the IF port, and how a circuit was designed to match the mixer IF impedance into the LNA.

The final part of this thesis is a study of molecular gas in M82. First, a map of ^{12}CO J=6→5 emission in the central kiloparsec of the galaxy will be presented, along with observations of ^{12}CO J=4→3, ^{12}CO J=3→2, and ^{13}CO J=3→2. A commonly used measure of the physical conditions of molecular clouds is the ratio of the intensities of different emission lines. I will present a novel deconvolution technique to calculate maps of spectral line intensity ratios that extracts position information from the line shape. I use this technique to compute a J=6→5 / J=2→1 line ratio map

based on high-resolution ^{12}CO J=2→1 interferometer data. This line ratio and the J=6→5 emission both have peaks located on either side of the center of the galaxy. I evaluate the physical conditions at these two peaks using the four measured transitions presented in this work along with an upper limit for ^{13}CO J=6→5 and five measured transitions from the literature. An excitation model is used to calculate line intensities based on parameters such as the temperature, density, and column density of the molecular gas assuming that the gas is comprised of two independent components, one warm and one cool. This model is fit to the measured intensities. In part due to measurement uncertainty in the data, we expect a family of model solutions to be consistent with the measured intensities. Rather than present a single best-fit model, likelihood curves are calculated for each of the model parameters, such as temperature and density, as well as for a variety of related physical quantities, such as pressure and beam-averaged column density. This approach reveals how well various quantities can be constrained by the observations.

Chapter 2
SuperMix Receiver Simulation Software

2.1 Overview

2.1.1 Motivation: Designing and Simulating SIS Receivers

Although there are many excellent software packages available to aid the design of microwave circuits, none provide the specialized elements needed for the design of complete superconducting tunnel junction (SIS) receivers. For instance, thin film microstrip lines, which are widely used in SIS mixers for impedance matching circuits, have characteristics which depend on the surface impedance of the normal or superconducting metal films. Surface impedance calculations usually involve nontrivial numerical computations, such as numerical integration or the solution of integral equations (Mattis and Bardeen 1958; Pöpel 1989; Bin 1997), and are not available in commercial microwave software packages. Furthermore, the calculation of the signal and noise properties of SIS mixers requires the use of Tucker's theory (Tucker and Feldman 1985) combined with a nonlinear harmonic-balance calculation (Withington and Kollberg 1989; Rice et al. 1999) of the local oscillator waveform. Again, the required calculations are numerically intensive and are not available in commercial packages.

It is clear that a complete simulation of an SIS mixer is a substantial computational task. Because of this, SIS mixer design is usually performed using simplifying approximations. For instance, the RF circuit is usually designed and optimized by treating the problem as an impedance matching exercise. Once a circuit is designed in this way, the embedding admittances it presents to the SIS junction can be calculated, and these can be used in a Tucker theory calculation to determine the conversion loss

and noise temperature of the mixer. The results of such a calculation could then be imported into a standard microwave program to explore the effect of the HEMT IF amplifier and its matching circuit. This was the approach followed by Padin et al. (1996) for the design of an integrated HEMT IF amplifier for an SIS mixer.

However, prior to SuperMix, no one has ever designed an SIS receiver by directly calculating the noise temperature across some desired RF band, including the harmonic effects and the IF amplifier contribution, and optimizing this total receiver noise temperature as a function of the circuit parameters. Even though this sounds like the most obvious and straightforward approach to the design, the software to do this has simply been unavailable until now. Furthermore, with the exception of a few special cases involving two junction circuits (Zmuidzinas et al. 1994; Noguchi et al. 1995), parallel arrays (Shi and Noguchi 1998), and distributed junctions (Tong et al. 1997), most of the Tucker-theory programs that have been written for SIS design assume that only a single SIS junction will be used. However, now that junction fabrication processes are reliable and reproducible, there is a clear trend toward more complex mixer designs incorporating multiple junctions. For example, Chattopadhyay et al. (2000) developed a dual-polarized mixer using eight SIS junctions.

2.1.2 Alternative Approaches

There are several possible solutions to this problem. Some commercial circuit simulators allow user-defined elements to be written using an interpreted "scripting" language. However, it was felt that this approach would not provide the necessary level of computational performance needed for simulating and optimizing superconducting mixers. Indeed, existing Tucker theory SIS mixer programs are written in standard compiled programming languages such as FORTRAN. Alternatively, it might have been possible to work with a software vendor to have routines for SIS mixer simulation incorporated directly into a commercial microwave package. However, it is doubtful that many vendors would be interested given the very limited market. Furthermore, being dependent upon closed-source proprietary software would have hampered the

ability to rapidly add new elements and models to the code as new materials and mixer designs are developed. Finally, it was desired to have software that would run on a large variety of platforms, unplagued by licensing restrictions. For these reasons it was decided to develop a stand-alone package.

2.1.3 A Complete Simulation Library

A C++ library called "SuperMix" has been developed to provide a flexible tool with which to design and optimize receiver circuits, and microwave circuits in general.

SuperMix calculates circuits in the familiar wave representation, in which the behavior of a linear circuit is specified by a scattering matrix, a noise wave correlation matrix, and an outgoing source wave amplitude vector. The source wave vector represents the effects of generators inside the circuit, such as a local oscillator. Easy-to-use functions can convert the wave representation to other quantities, such as impedance or admittance matrices, gain, or noise temperature.

The C++ programming language (Stroustrup 1997) was chosen for this project to provide flexibility, ease of use, and a means to design the library with a modular approach. For this project, complex numbers, vectors, and matrices are used extensively, and the C++ programming language can be extended to include them in a natural and powerful way. For instance, the standard arithmetic operations with complex vectors can be defined, as can the operation of multiplying a vector by a matrix.

As an object-oriented language, C++ provides a natural way to write modular programs. The SuperMix library was written from the ground up to be highly modular, flexible, and expandable. Circuits and circuit elements are implemented as C++ class objects. The modular approach used allows new elements to be added to the library by writing only a few lines of code (to calculate the scattering and noise matrices) without having to deal with details about how the overall library works. The modular design of the optimizer provides a straightforward means to add new optimization algorithms if needed. Almost every part of the library benefits from the

Basic Elements	*Transmission Lines*	*Transistors*	*Other Elements*
Resistor	Superconducting Film	Transconductance	Mixer
Capacitor	Normal Metal Film	FET	SIS Junction
Inductor	Layered Film	Fujitsu FHR02X	Transformer
Attenuator	Dielectric	Fujitsu FHX13X	180° Hybrid
Terminator	Transmission Line	Kukje HEMT	90° Hybrid
	Microstrip	JPL-TRW InP 160 μm	Circulator
	CPW	JPL-TRW InP 300 μm	Voltage Source
	Radial Stub		Current Sink
	Time Delay		Generator
	Rectangular Waveguide		Slot Antenna
			Twin Slot Antenna
			Power Divider
			Deembed
			Touchstone Reader

Table 2.1 Circuit Components Currently Provided by the Library

flexibility provided by the C++ programming language.

Each circuit element in SuperMix inherits the properties common to all devices. This way, each element added to the library automatically includes a standard interface, for instance, a function to return scattering parameters of the circuit element. Lossy elements which generate noise can be assigned arbitrary temperatures. A list of circuit elements currently available in the library is given in Table 2.1.

2.2 The Wave Representation

Internally, circuits are calculated using a wave representation based on the scattering matrix. This representation was chosen in part because it is numerically well behaved: unlike the impedance representation, which is singular for open circuits, and the admittance representation, which is singular for short circuits, the elements of the scattering matrix are always finite and well-defined.

The incoming and outgoing wave amplitudes at some port i of a linear circuit are defined in terms of the voltage V_i across the port terminals and the current I_i flowing

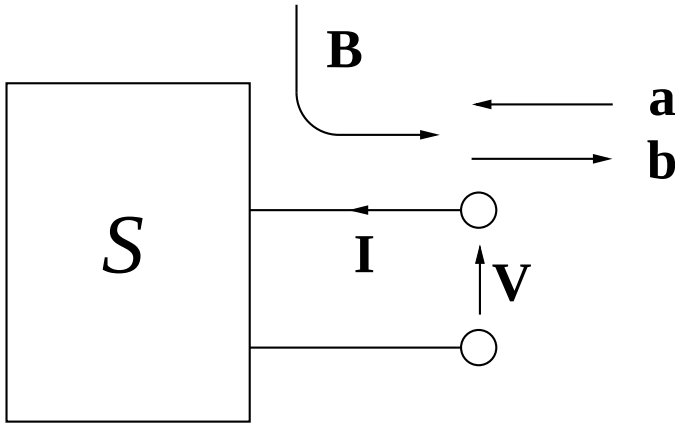

Figure 2.1 The scattering matrix representation of a linear circuit.

into the positive terminal by the expressions

$$a_i = \frac{1}{2\sqrt{Z_0}}\left(V_i + Z_0 I_i\right) \quad \text{and} \quad b_i = \frac{1}{2\sqrt{Z_0}}\left(V_i - Z_0 I_i\right) , \tag{2.1}$$

where Z_0 is some standard normalizing impedance. These definitions are motivated by transmission line theory. Note that the normalization is chosen such that power can be calculated simply by squaring the wave amplitudes. For instance, the incoming power at port i is $P_{incident} = |a_i|^2$ and the reflected power is $P_{reflected} = |b_i|^2$. Thus the net power absorbed by a circuit is

$$P = \mathbf{a}^\dagger \mathbf{a} - \mathbf{b}^\dagger \mathbf{b} . \tag{2.2}$$

Extensive discussions of the scattering matrix and its use in circuit calculations can be found in the references (Wedge 1991; Wedge and Rutledge 1992; Dobrowolski and Ostrowski 1996).

SuperMix uses three quantities to represent a circuit: the scattering matrix $\mathcal{S}$, the noise wave correlation matrix $\mathcal{C}_S$, and the wave source vector $\mathbf{B}$. The definition of these quantities comes from the following expression, in which the outgoing wave amplitudes $\mathbf{b}$ are considered to be dependent upon the incoming wave amplitudes $\mathbf{a}$:

$$\mathbf{b} = \mathcal{S}\mathbf{a} + \mathbf{c} + \mathbf{B} , \tag{2.3}$$

see Figure 2.1. The source vector **B** represents the effect of *deterministic* voltage or current generators inside the circuit which cause outgoing waves with various amplitudes and phases to emanate from the circuit's ports even in the case that the incoming wave amplitudes **a** all vanish. In contrast, **c** represents outgoing *noise* waves, which are the result of various noise current or noise voltage generators inside the circuit. These noise waves are characterized by the noise wave correlation matrix $\mathcal{C}_S$, defined by the relation

$$< c_i(\nu)\, c_j^*(\nu') > \;=\; [\mathcal{C}_S]_{ij}\, \delta(\nu - \nu')\;, \tag{2.4}$$

where $c_i(\nu)$ represents the Fourier component at frequency ν of the noise wave emanating from port i. Finally, the product $\mathcal{S}\mathbf{a}$ represents the outgoing waves that are generated when the incoming deterministic waves **a** are scattered by the N-port circuit, which has a scattering matrix $\mathcal{S}$.

2.3 Noise in Passive Elements

The Johnson noise from a resistor at temperature T in a frequency bandwidth of $\Delta\nu$ is usually taken to be

$$P_n \;=\; k_B\, T\, \Delta\nu\;. \tag{2.5}$$

This expression implicitly assumes the Rayleigh-Jeans limit, i.e., $h\nu \ll k_B T$. At 690 GHz, $h\nu/k_B = 33$ K. Clearly, it would be inappropriate to blindly use equation 2.5 for a receiver operating at 690 GHz in a 4.2 K liquid helium cryostat. In this case, the Planck formula must be used without approximations. In addition, an extra half-photon of noise from zero-point quantum fluctuations is present in all coherent detectors, including SIS receivers, since the precision with which the magnitude and phase of the incoming radiation can be measured is limited by the uncertainty relation. The Callen-Welton formula (Callen and Welton 1951) for noise spectral density is equivalent to the sum of the Planck term and the zero-point quantum fluctuation

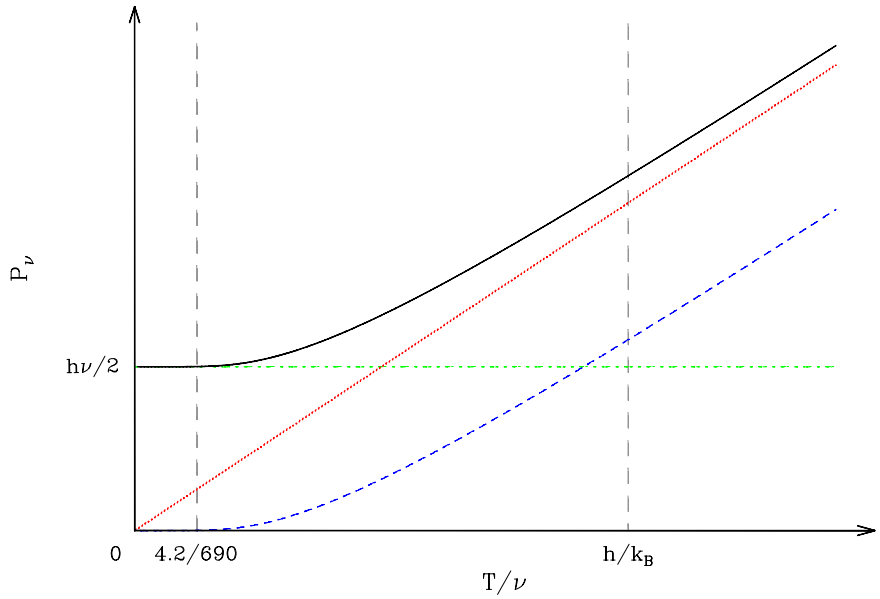

Figure 2.2 Thermal noise spectral density. The Planck noise is displayed as a blue dashed curve, and the half-photon of noise present in all coherent detectors as the green horizontal line. SuperMix uses the sum of these two components, called the Callen-Welton formula, shown in solid black. The left vertical dashed line corresponds to a temperature of 4.2 K at 690 GHz. The Rayleigh-Jeans approximation, shown in dotted red, is only valid when $T/\nu \gg h/k_B$.

term (Figure 2.2). In temperature units,

$$\frac{h\nu}{2k_B}\coth(h\nu/2k_BT) = \frac{h\nu/k_B}{\exp(h\nu/k_BT)-1} + \frac{h\nu}{2k_B}\,. \tag{2.6}$$

This reduces to T in the Rayleigh-Jeans limit, $h\nu \ll k_BT$.

SuperMix calculates the noise correlation matrices of passive elements or passive circuits at a uniform temperature T from their scattering matrices using the formula

$$\mathcal{C}_S = \frac{h\nu}{2k_B}\coth(h\nu/2k_BT)\,(\mathcal{I}-\mathcal{S}\mathcal{S}^\dagger)\,, \tag{2.7}$$

where $\mathcal{S}$ is the scattering matrix, $\mathcal{I}$ is the identity matrix, and $\mathcal{C}_S$ is the noise correlation matrix. These equations are derived and discussed in Bosma (1967), Wedge and Rutledge (1991), and Wedge (1991). SuperMix uses the Callen-Welton spectral density to automatically include both quantum noise as well as the thermal noise produced by lossy elements (e.g., warm optics or lossy microstrip). Because the zero-point

quantum noise term is included, the correct value of the IF output noise is calculated for a mixer whose RF input is terminated with a load (Wengler and Woody 1987; Devyatov et al. 1986). Note that commercial microwave programs usually use the Rayleigh-Jeans approximation for thermal noise, which is, once again, inappropriate for cryogenic receiver systems at millimeter wavelengths which have components at temperatures below $h\nu/k_B$.

The passive noise computations are carried out by a single standard function. Thus, when adding new passive elements to the library, it is usually sufficient to program only the scattering matrix calculation, and then use the standard library function to calculate the noise correlation matrix.

2.4 Connecting Circuits

The SuperMix library provides a class `circuit` to create composite circuits. A user can assemble a circuit from the basic elements (resistors, capacitors, etc.) by calling the `connect` member function of a `circuit` object. The `connect` function allows the user to connect ports between other circuits and/or basic elements. See Section 2.9.1 for an example of how to assemble and simulate a simple composite circuit. The circuits being connected can have arbitrary numbers of ports; hence the concept implemented by the `connect` function is much more general than a simple cascade of two-ports. Furthermore, the `connect` function allows both *interconnections*, in which the ports are on two different subcircuits, as well as *intraconnections*, in which two different ports of the same circuit are being connected. Series and parallel "tee" components are available to allow series or parallel connections.

Since all elements including the `circuit` class share the same software interface (they are all derived from a single generic device class), composite circuits can be used in other composite circuits. Thus, a hierarchical design is possible: large, complicated circuits can be built up from smaller, more manageable pieces. This capability is a direct benefit of the modular design described in Section 2.1.3.

A composite circuit calculates itself by making a single connection between the

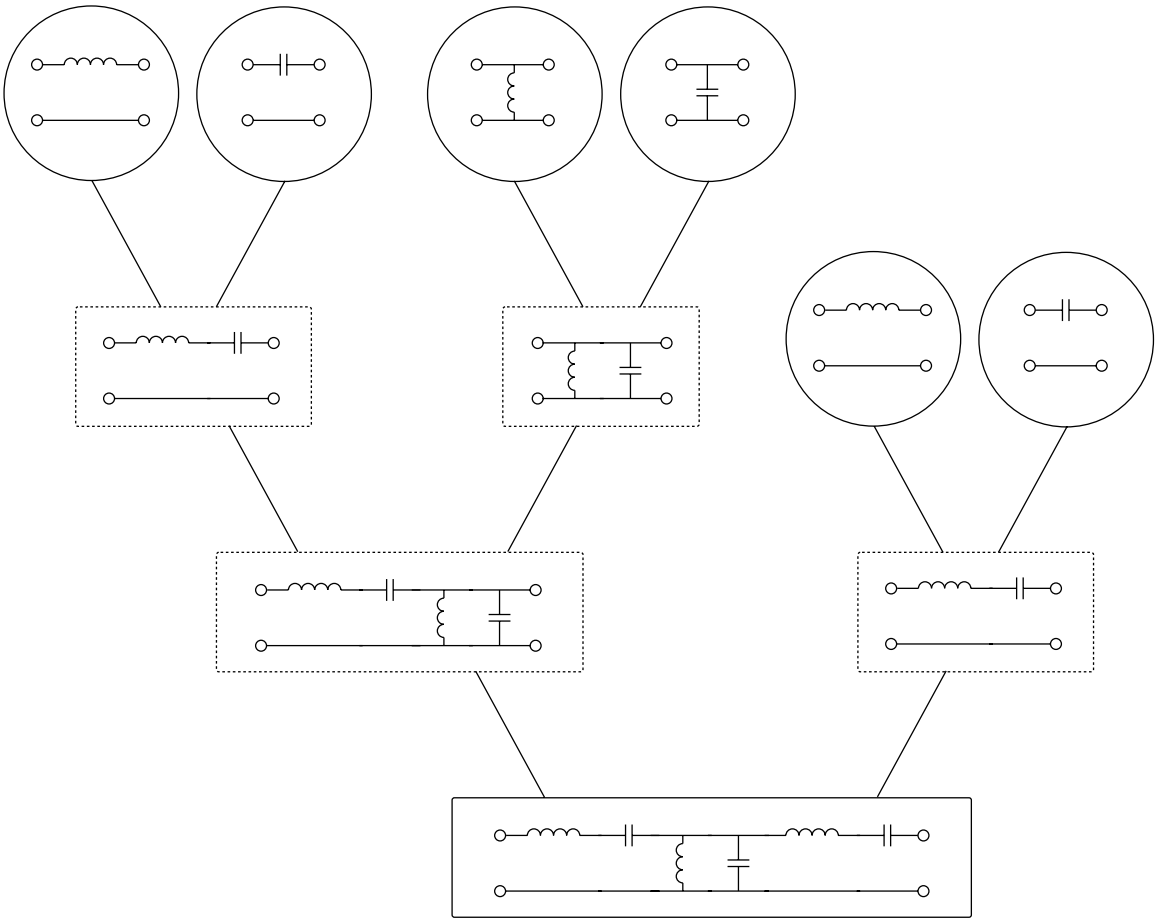

Figure 2.3 This diagram shows how SuperMix would calculate a simple bandpass filter using the method of subnet growth. The circles represent the elements of the circuit defined by the user. Connections are calculated one at a time, creating the intermediate subcircuits in the dashed boxes. The complete circuit forms the base of the tree. Note that this simple example in no way implies that SuperMix is limited to cascading two-ports; in general, SuperMix can calculate arbitrarily complicated multi-port circuits.

ports of its elements or subcircuits at a time. The $\mathcal{S}$ and $\mathcal{C}_S$ matrices for the two subcircuits are combined using equations developed by Wedge (1991) using signal flow graphs. When a composite circuit is asked to calculate itself, it splits itself into two subcircuits and asks each for its $\mathcal{S}$ and $\mathcal{C}_S$ matrices and source vector $\mathbf{B}$. Each of these subcircuits splits itself in two. The process continues until all subcircuits are broken down to the original basic elements. This process creates a binary tree (Figure 2.3). The desired circuit is the base, and the tips of the branches are the components of the circuit. The intermediate subcircuits form the branches. This algorithm is fast because the tree only needs to be built a single time yet can be used for an unlimited number of calculations, such as for different frequency points or in the inner loop of the optimizer. A detailed description of the circuit connection algorithm can be found in Appendix A.

2.5 Transmission Lines

The SuperMix C++ library includes a number of classes which can be used to calculate the properties of normal and superconducting transmission lines, such as the characteristic impedance and propagation constant. The transmission lines can be used as elements in circuits such as SIS mixers. SuperMix currently includes microstrip, rectangular waveguide, and lossless coplanar waveguide. Adding new types is straightforward: the user only needs to calculate the characteristic impedance and the propagation constant. The conversion of these quantities into the scattering and noise correlation matrices is handled by library routines.

The characteristics of thin-film transmission lines (such as microstrip) often depend strongly on the surface impedance of the metal conducting films used. SuperMix can calculate the surface impedance for normal metals and superconductors (Mattis and Bardeen 1958) in the case of a local conductivity $\sigma(\omega)$ defined by Ohm's law, $\boldsymbol{J}(\boldsymbol{r},\omega) = \sigma(\omega)\,\boldsymbol{E}(\boldsymbol{r},\omega)$.

Transmission lines such as microstrips often use dielectric films or substrates, and the complex dielectric constant ϵ of the material must be specified. Dielectrics can be

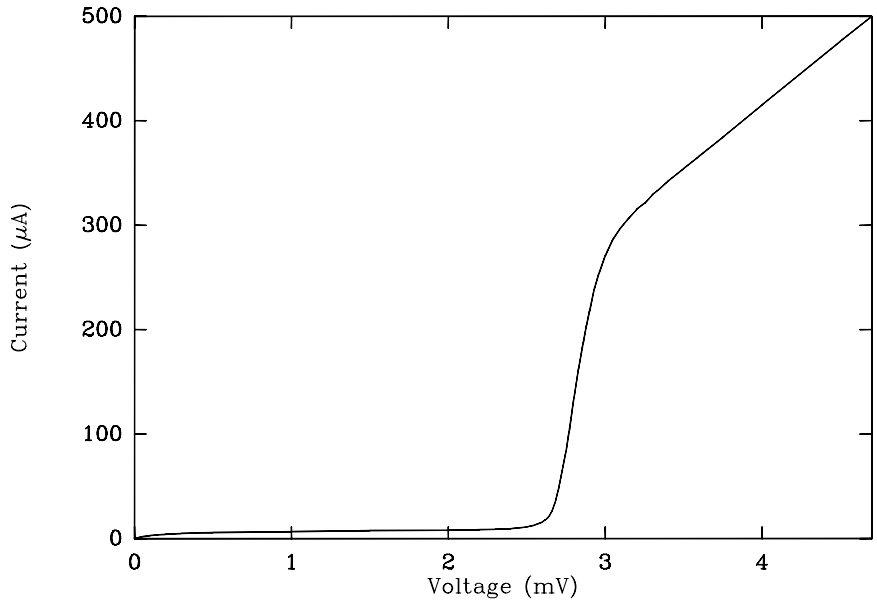

Figure 2.4 IV curve of an unpumped SIS junction.

defined in SuperMix by specifying the real part of ϵ and the loss tangent, Im[ϵ]/Re[ϵ]. If necessary, a table of values specifying a frequency-dependent $\epsilon(\nu)$ can be read from a data file and automatically interpolated. Actually, this can be done for any circuit parameter, and the interpolation can be done with respect to any other parameter (e.g., temperature), not just frequency.

Conductive films and dielectrics form the building-blocks for transmission lines. After the dielectrics and conductors have been specified, transmission lines such as microstrip can be assembled from them. See Section 2.9.2 for an example of how to assemble and simulate a simple superconducting microstrip line.

2.6 Mixers

As its name implies, SuperMix was created primarily to simulate circuits including superconducting heterodyne mixers. Mixers are simulated using a combination of linear circuits and objects derived from a generic nonlinear device class named `junction`. The `junction` class does not implement any specific device; rather, it defines a standard software interface for all nonlinear devices that can calculate both their large and small signal responses in the frequency domain. Currently, the only nonlinear

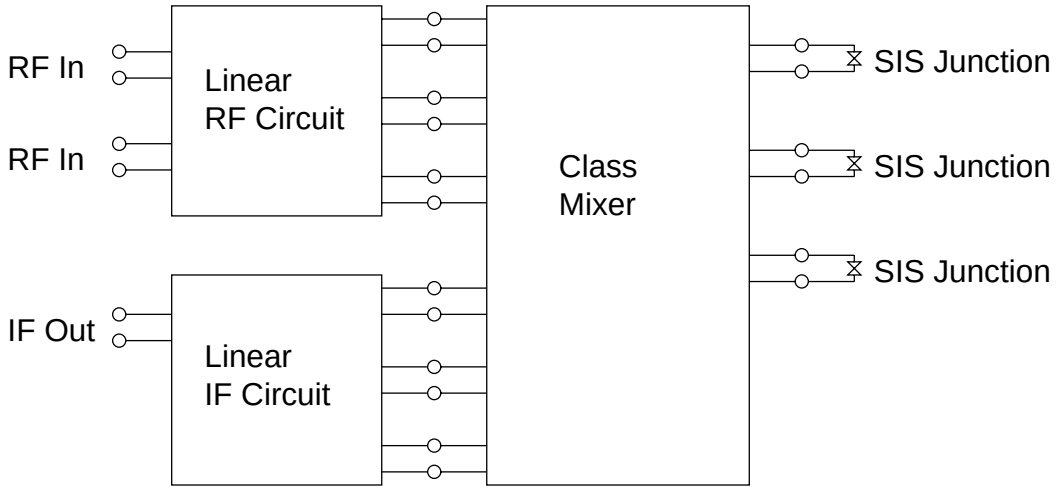

Figure 2.5 SIS mixer simulation. The RF and IF linear circuits are usually two different models of the same physical circuit to account for differences in electrical behavior in the different frequency realms. The `class mixer` instance performs the harmonic balance and small signal analysis.

devices available within SuperMix are superconducting tunnel (SIS) junctions. The SIS junction object reads its current-voltage (IV) curve from a data file, which can be either experimentally measured or mathematically generated (Figure 2.4). Other nonlinear devices could be implemented by adding the code that simulates the device behavior to a new subclass of `class junction`.

The mixer is assembled from a `class mixer` object, any number of SIS junctions, a radio-frequency (RF) linear circuit, and an intermediate-frequency (IF) linear circuit (Figure 2.5). Typically, the RF and IF circuits are two different models of the same physical circuit, since the electrical characteristics at the IF are usually completely different from the electrical characteristics at the local oscillator (LO) frequency and its harmonics. The linear circuits can be arbitrarily complicated and can contain arbitrary numbers of ports. The LO can be injected anywhere in the RF linear circuit. The `mixer` will then calculate its operating state by performing a harmonic balance; the number of harmonics used in the balance can be as large as the user deems necessary. After the operating state is determined, the user can ask the `mixer` object to perform a small signal analysis (Rice et al. 1999). Once these calculations are complete, which typically takes a few milliseconds total per frequency point,

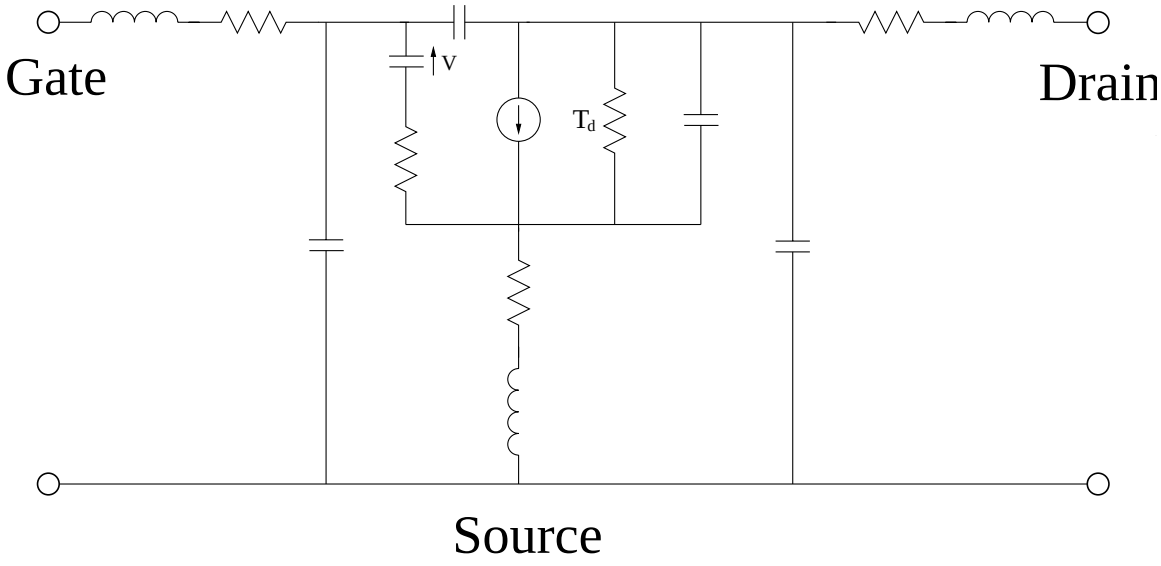

Figure 2.6 Small signal FET model.

including solving the linear circuits and the harmonic balance, the user may examine standard quantities such as noise temperature and conversion gain. The user may also look into details such as the impedance, admittance, or reflection coefficient looking into each port at each sideband of each harmonic of the LO, as well as the transmission via mixing from one harmonic of the LO to another, including the IF. In other words, the entire multifrequency scattering and noise matrices are calculated and are available to the user.

2.7 Transistors

Field-effect transistors (FETs) are modeled with the small-signal equivalent circuit shown in Figure 2.6 (Pospieszalski 1989). The active element is a current source that provides a current proportional to the voltage marked with a V in the figure,

$$I = V g_m \exp(-j\omega\tau) \, , \tag{2.8}$$

where I is the current, g_m is the transconductance of the FET, ω is the angular frequency, and τ is the FET transit time. Pospieszalski showed that the FET noise

performance can be calculated by setting the temperature of the drain-source resistor (labeled T_d in the figure) to a frequency-independent value.

New transistors can be added to SuperMix by first measuring the scattering matrix across a wide frequency band with a vector network analyzer. SuperMix can read in data files written by most modern network analyzers, and provides a `deembed` object to remove the effects of any input and output circuits included in the measurements. The optimizer can then be used to find the FET model parameters by matching the model predictions to the measured data. The effective drain temperature must be determined by measuring the noise parameters at at least one frequency. See, for example, Pospieszalski et al. (1988).

2.8 A Flexible Optimizer

The optimizer was designed to be a very flexible tool that can minimize general error functions by varying nearly any circuit parameter, real or complex. At present, SuperMix allows standard quantities of interest such as gain, noise temperature, and input or output match to be readily included in the definition of the error function. These quantities are usually calculated while sweeping the frequency over one or more bands. For instance, the design of a bandpass filter requires that the transmission across the passband be maximized while the transmission in stopbands be minimized. SuperMix supports this capability; furthermore, any parameter can be swept, not just frequency. Even multi-dimensional sweeps are allowed. For example, a receiver can be optimized simultaneously over both LO and IF frequency. See Section 2.9.1 for a simple example of how to optimize the parameters of a circuit.

The modular design of the optimizer allows easy addition of new types of error function terms. In addition, the interface between the error function and the optimization routine is simple and generic, and so it is easy to add new minimization algorithms. The SuperMix optimizer currently includes both a deterministic and a semi-stochastic minimizer. The deterministic minimizer uses Powell's method; this routine is both robust and fast. In practice, it has been used to optimize 10 param-

eters of a 50 element linear amplifier across an octave bandwidth. On a 333 MHz Sun Ultra 10, this entire optimization and simulation runs in less than 10 seconds. One downside of Powell's method is that it can converge upon local rather than global minima, so the user must choose reasonable initial values for the parameters being optimized. SuperMix also provides a novel minimizer to find global minima in the presence of local minima for those times when adequate starting values are not available. This method works by picking initial parameter values randomly, then continuing with Powell's method. When Powell's method begins to converge, the process is repeated with a new random starting point. This is iterated many times until a target error function value is achieved or a maximum iteration count is reached. In either case, the optimizer reports the best parameters found. This technique is especially powerful when there are only a relatively small number of local minima, as is often the case with error functions for microwave and submillimeter circuits, since it combines the robustness of a stochastic method with some speed advantages of a deterministic minimizer. Other approaches, such as purely stochastic algorithms, could easily be added to SuperMix.

2.9 Using the SuperMix Library

A circuit is simulated by writing a C++ program that uses the SuperMix library. Devices in the library are represented as C++ class objects, which can be used simply by declaring a variable of the appropriate type. For example, declaring a variable of type `resistor` will automatically provide all functionality needed for the simulation of a resistor, including parameters for resistance and physical temperature, and functions to return the scattering matrix, noise correlation matrix, noise temperature, etc., of this element. All elements are derived from a single generic device class, guaranteeing a uniform standard interface for all devices and allowing the user to add elements to the library with a minimum of effort.

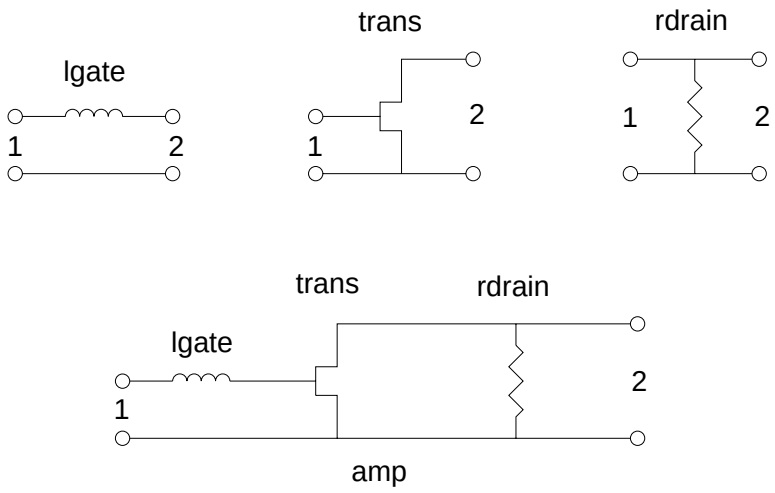

Figure 2.7 Block diagram of a single-stage LNA.

2.9.1 Simulation of a Low-Noise Amplifier

The source code for a complete program to optimize and simulate the single-stage low-noise HEMT amplifier drawn in Figure 2.7 is listed in in Figure 2.8. This program demonstrates the key features of the linear circuit library, including creating circuit elements, connecting them, and running the optimizer. The results are plotted in Figure 2.9.

In this example, there are only three subcircuits being connected together to produce the composite circuit `amp`: the gate inductor `lgate`, the Fujitsu FHX13X transistor `trans`, and the drain resistor `rdrain`. Each of the subcircuits is a two-port; the ports are labeled by integers as shown in Figure 2.7. The statement `amp.connect(lgate, 2, trans, 1)` connects port 2 of the inductor to port 1 (the gate) of the transistor. Similarly, `amp.connect(trans, 2, rdrain, 1)` connects the drain of the transistor to the resistor. The statement `amp.add_port(lgate, 1)` simply specifies that port 1 of the inductor will be used as port 1 (the input) of the overall amplifier circuit. Finally, `amp.add_port(rdrain, 2)` specifies the output port of the amplifier.

```
#include "supermix.h"

int main(void) {

  // Set the global temperature.
  device::T = 4.2 * Kelvin;

  // Declare the components we will use for the circuit.
  fhx13x trans;      // Fujitsu HEMT transistor
  inductor lgate;    // Gate tuning inductor
  resistor rdrain;   // Drain bias line

  // The inductor is series, resistor parallel.
  lgate.series();
  rdrain.parallel();

  // Construct the circuit.
  circuit amp;
  amp.add_port(lgate, 1);            // Put the gate inductor at the input.
  amp.connect(lgate, 2, trans, 1);   // Connect the inductor and transistor.
  amp.connect(trans, 2, rdrain, 1);  // Connect the transistor and resistor.
  amp.add_port(rdrain, 2);           // Make the drain resistor the output.

  // Define the optimization band.
  sweeper band1;
  band1.sweep(device::f, 4.*GHz, 8.*GHz, 0.5*GHz);

  // Declare an error function.
  error_func ef;

  // Define which parameters are optimized.
  lgate.L  = ef.vary( 1,  3,  10, nHenry);
  rdrain.R = ef.vary(30, 50, 100, Ohm);

  // Define the error function.
  gain_dB gain(amp, 1, 2, error_term_mode::MATCH, 12);  // Optimize for flat gain.
  ef.add_term(1.0, band1, gain);
  input_tn tn(amp, 1, 2, error_term_mode::MATCH, 0.0);  // Optimize for low noise.
  ef.add_term(2.0, band1, tn);

  // Use the Powell algorithm for minimizing.
  powell pow1(ef);             // Minimize the error function we created above.
  pow1.FTOL = 0.00001;         // Define the tolerance for the convergence test.
  pow1.minimize();             // Run the optimizer.
  ef.get_parms_user().show();  // Print the optimized parameters.

  // Print out gain and noise temperature in our optimization band.
  cout << "\n        Freq     S21(dB)       Tn(K)" << endl;
  for(double freq = 4.0*GHz; freq <=8.1*GHz; freq += 0.2*GHz)
  {
    device::f = freq;
    sdata sd = amp.get_data();
    cout << setw(12) << freq/GHz            // Print the frequency in GHz.
         << setw(12) << sd.SdB(2,1)         // Print the gain in dB.
         << setw(12) << sd.tn(2,1)/Kelvin   // Print the noise temperature in Kelvin.
         << endl;
  }
}
```

Figure 2.8 Simulation and optimization of the single-stage LNA shown in Figure 2.7.

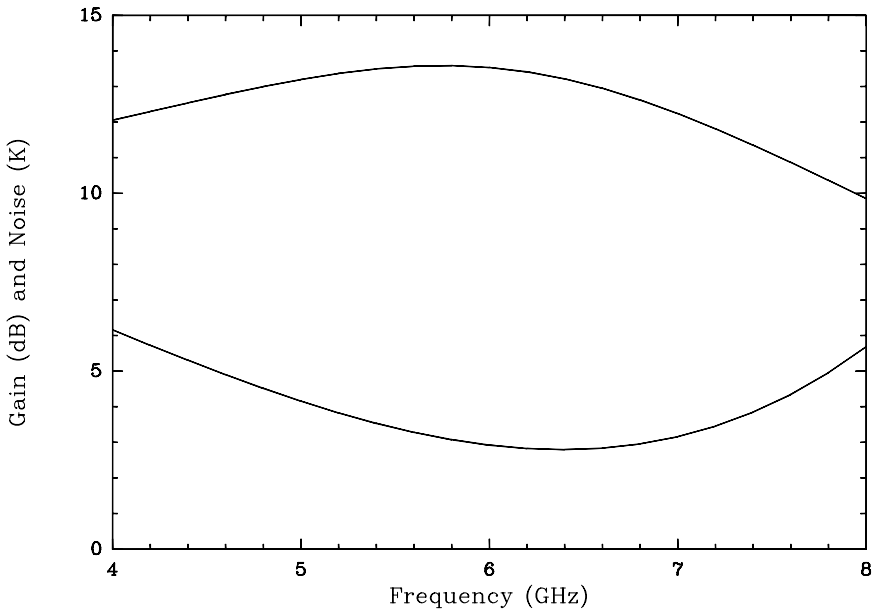

Figure 2.9 Gain (top curve) and noise temperature (bottom curve) of the simple single-stage LNA shown in Figure 2.7.

2.9.2 Simulation of a Section of Microstrip

The code in Figure 2.10 is a complete program to simulate a segment of superconducting microstrip. It demonstrates the ease with which a microstrip line can be constructed and the high level of readability of a C++ circuit file.

2.9.3 Simulation of a 690 GHz Receiver

The previously presented examples are of very simple circuits to demonstrate the basic capabilities and usage of the SuperMix library. The full simulation of a real-world SIS receiver is substantially more lengthy. The complete simulation of a 4-8 GHz low-noise amplifier is presented in Appendix F, and the simulation of a 690 GHz SIS receiver in Appendix G. Results of these simulations are presented in Chapters 4 and 5.

```
#include "supermix.h"

int main()
{
  device::T  = 4.2*Kelvin;  // Set the default operating temperature.
  device::Z0 = 50*Ohm;      // Set the default normalization impedance.

  // Create a superconducting film called niobium.
  super_film niobium;

  niobium.Vgap       = 2.9*mVolt;
  niobium.Tc         = 9.2*Kelvin;
  niobium.rho_normal = 5.0*Micro*Ohm*Centi*Meter;
  niobium.Thick      = 3000*Angstrom;

  // Create dielectrics
  const_diel SiO(5.6, 0.0001);   // Create a silicon oxide dielectric.
  const_diel air(1.0, 0);        // Create a dielectric for air.

  // Construct a new microstrip variable.
  microstrip ms1;

  ms1.superstrate(air);
  ms1.top_strip(niobium);
  ms1.substrate(SiO);
  ms1.ground_plane(niobium);

  ms1.sub_thick = 2500*Angstrom;
  ms1.width     = 1.0*Micron;
  ms1.length    = 100*Micron;

  // Display complex numbers in magnitude phase(degrees) format.
  complex::out_degree();
  cout << fixed << setprecision(3);

  // Print out S21 for this microstrip from 100 to 1000 GHz, step by 10 GHz.
  cout << "      f(GHz)               S21" << endl;
  for(double freq = 100. ; freq <= 1000.; freq += 10)
  {
    device::f = freq*GHz ;
    cout << setw(12) << freq << "   "
         << setw(16) << ms1.S(2,1)
         << endl;
  }
}
```

Figure 2.10 Simulation of superconducting microstrip in SuperMix.

2.10 Compatibility and Availability

The library was written in standard C++ and should compile on most platforms using an ANSI C++ compiler that supports the Standard Template Library (STL). The package has been tested using the freely available GNU g++ compiler on SPARC Solaris 2.7 and Intel Linux platforms. The entire library, which is currently composed of about 40,000 lines of source code, is available free of charge on the internet at http://www.submm.caltech.edu/supermix.

Chapter 3
Noise and Gain Measurements of Cryogenic Amplifiers

3.1 Overview

Before an IF amplifier can be used in an SIS receiver (Chapters 4 and 5), the signal and noise performance must be verified. The signal performance at room temperature can be easily measured with a commercially available vector network analyzer. Measurement of the noise, on the other hand, is more difficult. Fortunately, the complete noise correlation matrix of the amplifier need not be measured; for our purposes, measurement of the noise power referred to the input is adequate. This is accomplished by applying a known power at the amplifier input and measuring the power at the output,

$$P_{out} = G(P_{in} + P_{noise}) \ , \tag{3.1}$$

where G is the gain of the amplifier. Since there are two unknowns (G and P_{noise}), it is necessary to measure P_{out} for at least two different values of P_{in}. For accurate measurements, it is desirable to have the lowest-valued input power be small, i.e., $P_{in} \lesssim P_{noise}$, and to keep the spacing between the maximum and minimum input powers large. These requirements can be met by using the Johnson noise from a variable-temperature resistive terminator as a calibrated power source. It is convenient to work in the Rayleigh-Jeans approximation, since $h\,\nu \ll k_B\,T$ at microwave

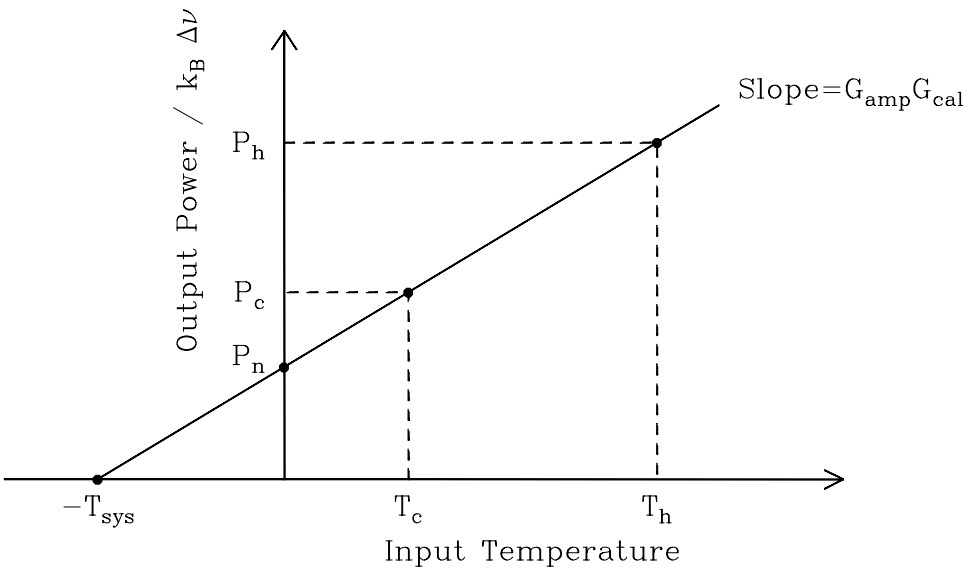

Figure 3.1 Calculation of amplifier gain and noise. T_h and T_c are input powers expressed in temperature units. The system noise temperature, T_{sys}, still includes some contribution from the spectrum analyzer. The gain of the spectrum analyzer, G_{cal}, must be determined by calibration.

frequencies. The input power is then

$$P_{in} = k_B \, \Delta\nu \, T \; . \tag{3.2}$$

Since noise power depends upon the frequency bandwidth, it is convenient to express all noise powers in temperature units by dividing by $k_B \, \Delta\nu$.

A spectrum analyzer is used to measure the output power as a function of frequency. Figure 3.1 shows graphically how the noise temperature referred to the input is calculated from two measured points for one frequency channel. Since the spectrum analyzer contributes noise to the system, its noise temperature must also be measured so that a correction may be applied to T_{sys} to find the noise of the amplifier.

3.2 A Computer-Controlled Spectrum Analyzer

The input signal to the spectrum analyzer ranges from a 4 K noise source to a room-temperature amplifier with 295 K input and 35 dB of gain. In a 100 MHz channel, this corresponds to an input power range from -112 dBm to -58 dBm. The spectrum

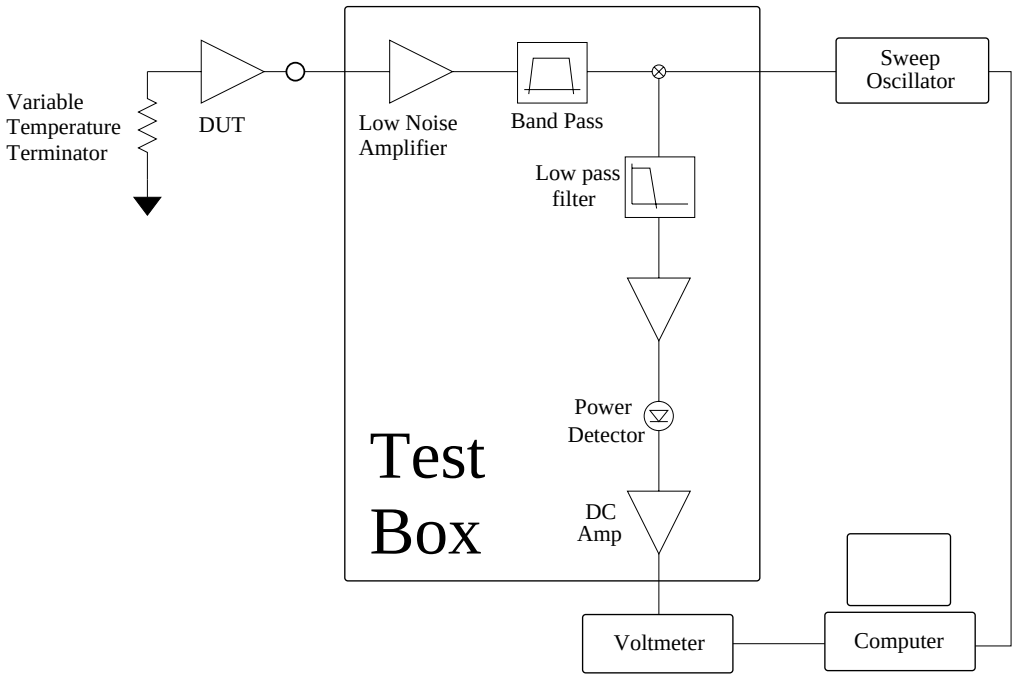

Figure 3.2 Amplifier test set schematic.

analyzer thus needs to have low noise to detect weak signals as well as a dynamic range of about 55 dB. Figure 3.2 shows a schematic diagram of a computer-controlled spectrum analyzer designed specifically for this task. First, a series of amplifiers increases the signal power. A computer-controlled oscillator is used to select the frequency channel by providing an LO to a mixer. A low-pass filter after the mixer cuts out frequencies above 50 MHz. Since the mixer operates in double-sideband mode, this gives the spectrum analyzer square channels 100 MHz wide. The signal in the channel is then further amplified before being fed into a power detector diode. The DC voltage across the diode is proportional to the input power. The system is controlled by a computer running a program developed with LabView (National Instruments). For each channel in the spectrum, this program sets the oscillator frequency, reads out the temperature of the noise source, and then reads the voltage of the diode power detector.

Maintaining accuracy over the wide dynamic range of the input power requires special care. If enough gain is provided to measure the weakest sources, then some amplifiers in the system will compress when measuring a room-temperature amplifier.

To prevent this, a 31 dB step attenuator was added to the middle of the 50 MHz amplifier chain. In designing the spectrum analyzer, it was critically important to calculate the maximum power at every point in the system to make sure that all amplifiers always operate well below their 1 dB compression points. It was also important to make sure that the system noise temperature doesn't depend on the attenuator setting.

3.3 Room Temperature Tests

Since cryogenic testing is slow and somewhat labor intensive, it is necessary to verify the amplifier at room temperature before cooling it in a cryostat. First, the DC IV curves of the transistors are checked. If the amplifier can be properly biased, then the scattering parameters are measured on a vector network analyzer.

If the signal performance is good, then the noise should be checked at room temperature before cooling the amplifier. To do this, the spectrum analyzer must first be calibrated. A $\sim$ 10 cm stainless steel coaxial cable terminated with a 50 Ω resistor is connected to the input of the spectrum analyzer. After recording the spectrum, call it P_h, the terminator is dunked in liquid nitrogen to cool it to 77 K. A second spectrum is recorded, call it P_c. The gain and noise temperature of the spectrum analyzer can be calculated at each frequency point:

$$G_{cal} = \frac{P_h - P_c}{T_h - T_c} \, , \tag{3.3}$$

and

$$T_{cal} = \frac{P_c}{G_{cal}} - T_c \, . \tag{3.4}$$

Note that T_h and T_c represent the noise power from the hot and cold terminators, which may not be exactly equal to their physical temperatures. A correction factor for the cable loss will be given in Section 3.4.1.

The amplifier under test is then inserted between the stainless steel coaxial cable

and the spectrum analyzer and the measurement process is repeated. New P_h and P_c are measured. The amplifier gain is

$$G_{amp} = \frac{1}{G_{cal}} \left(\frac{P_h - P_c}{T_h - T_c} \right) , \tag{3.5}$$

and the noise, corrected for the contribution from the spectrum analyzer, is

$$T_{amp} = \frac{1}{G_{amp}} \left(\frac{P_c}{G_{cal}} - T_{cal} \right) - T_c \, . \tag{3.6}$$

If the noise temperature is good, then the amplifier is ready to be tested cryogenically.

3.4 Cryogenic Tests

3.4.1 A Calibrated Noise Source

As with room temperature testing, the noise source for cryogenic tests is based on Johnson noise from a 50 Ω terminator at the end of a ∼ 10 cm stainless steel coaxial cable. Although stainless steel has undesirable electrical loss, its use is necessary to thermally isolate the noise source from the device under test. The terminator is mounted in a copper block to keep it at a uniform temperature. An additional resistor affixed to the block serves to dissipate DC power to heat the block up, and a diode allows the control computer to read out the temperature. The thermal time constant of the noise source is set by the length/area ratio of a copper strap connecting it to the cold surface of the cryostat.

Two sources of systematic error must be carefully minimized. First, varying the temperature of the noise source must not change the temperature of the device under test. This is avoided by bolting the device under test directly to the cryostat cold work surface, and by soldering a silver heat strap to the amplifier-end of the stainless steel cable such that any heat flow along the cable gets short-circuited to the cold work surface before reaching the amplifier. Secondly, loss in the stainless steel cable both attenuates the power from the terminator and contributes noise of its own. If

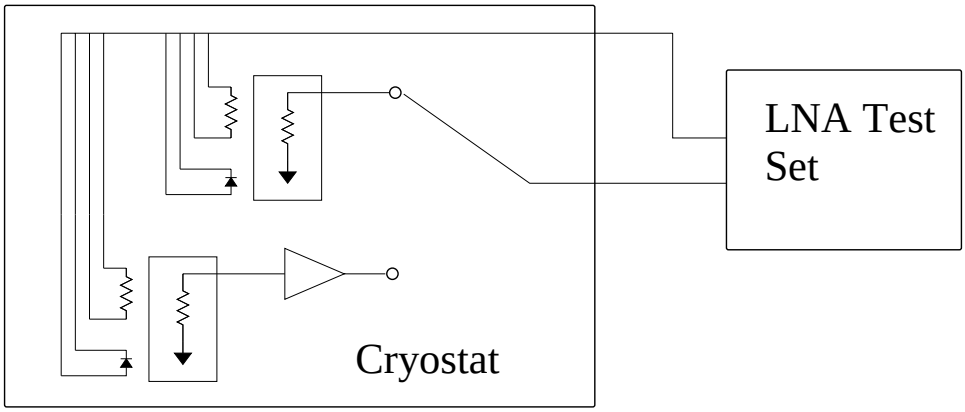

Figure 3.3 Configuration of the amplifier test cryostat. The upper terminator is heated to provide a variable-power noise source to calibrate the entire system down to the input to the switch. Then the lower terminator is heated to characterize the amplifier under test. The resistors to the left of the terminators are heaters, and the diodes are temperature sensors.

the amplifier is at temperature T_A, the terminator is at T_R, and A is the cable loss in dB, then the power from the noise source is

$$T = T_A + \frac{10\,(T_R - T_A)\,(1 - 10^{-\frac{A}{10}})}{A \ln 10}\ . \tag{3.7}$$

For example, if $T_R = 40$ K, $T_A = 4$ K, and the cable loss is 1 dB, then the noise power is 36.2 K. See Appendix B for the derivation of this equation.

3.4.2 The Cryostat

A diagram of the cryostat is shown in Figure 3.3. There are two noise sources: one at the amplifier input, and one for calibration. A switch is used to select the calibration source or the device under test. A single coaxial cable brings the signal out of the cryostat to the spectrum analyzer. A photo of the cold work surface is shown in Figure 3.4.

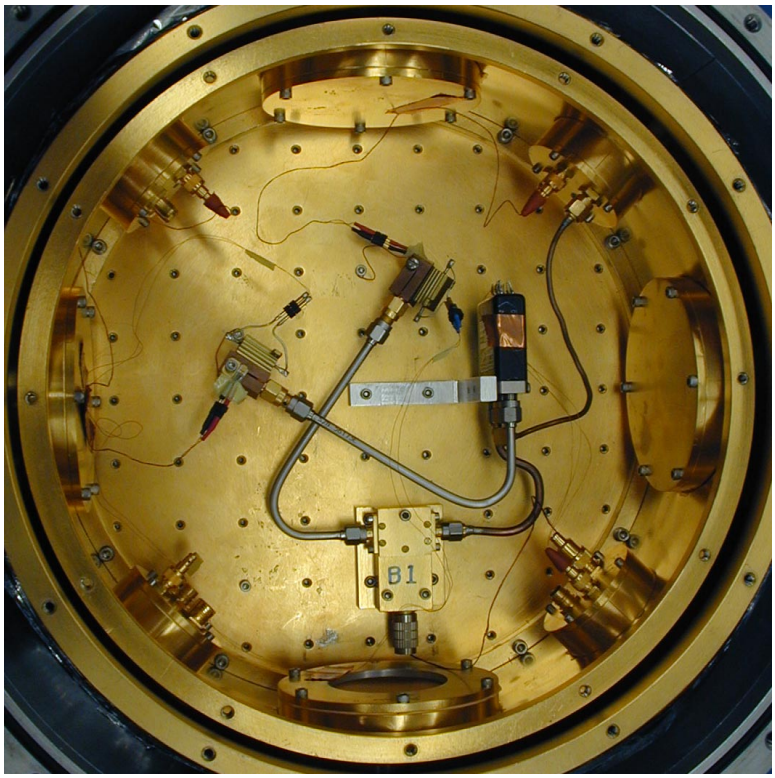

Figure 3.4 Amplifier test cryostat. The amplifier under test is the gold box in the lower center, labeled B1. The switch is mounted to the upper right on an aluminum bracket. The noise sources are small copper blocks mounted at the ends of the two stainless steel coaxial cables. Each source has a temperature sensor and a heater.

3.4.3 Running the Tests

To test a cold amplifier, first the amplifier is biased and the DC IV characteristics are checked. The switch is set to the calibration noise source. Current is run through the calibration noise source heater resistor until the terminator is at about 40 K. The heater is turned off, and the power spectrum is measured many times as the terminator cools. The control computer monitors the temperature of the terminator while it measures the spectrum. This way, after the terminator has cooled, a line of the form $P_{out} = G_{cal}(T_{in} + T_{cal})$ can be fit to the data for each frequency channel to find the gain, G_{cal}, and the noise, T_{cal}. The switch is then set to the device under test, and the noise source at its input is heated to about 40 K. The power spectrum is read out repeatedly as the noise source cools as was done for the calibration. Once again, a line is fit to the data for each frequency channel, this time to find G_{sys} and T_{sys}. It

mustn't be forgotten that before fitting lines to the measured data, the noise source temperatures must be corrected for loss in the stainless steel cable using equation 3.7. The amplifier gain and noise can be calculated from the fit results,

$$G_{amp} = \frac{G_{sys}}{G_{cal}} \tag{3.8}$$

and

$$T_{amp} = T_{sys} - \frac{T_{cal}}{G_{amp}} \, . \tag{3.9}$$

These results are calibrated to the input of the switch; the switch, cable out of the cryostat, spectrum analyzer noise, etc., have been calibrated out.

3.4.4 An Improved Measurement System

The noise tests described in the previous section have the disadvantage of being somewhat slow. The measurement speed is determined by the thermal time constant of the noise sources. Increasing the thermal conductivity to the cold surface will reduce the time constant; however, to maintain accuracy, the heat flow must be small enough that the temperature of the termination and the temperature sensor diode don't differ significantly. One would really like to adjust the amplifier DC bias conditions while watching the gain and noise temperature real-time. This can be accomplished by modifying the test setup to avoid the thermal time constant limitation entirely.

Figure 3.5 shows a modified version of the test cryostat. This version adds two coaxial cables into the cryostat to allow test signals to be sent through large (20-30 dB) heated attenuators that replace the 50 Ω terminators. A photograph of the cold work surface is shown in Figure 3.6. The gain and noise can still be measured with this system using the method described in Section 3.4.3 by terminating the coaxial cables into the cryostat and accounting for the additional power from them in the math.

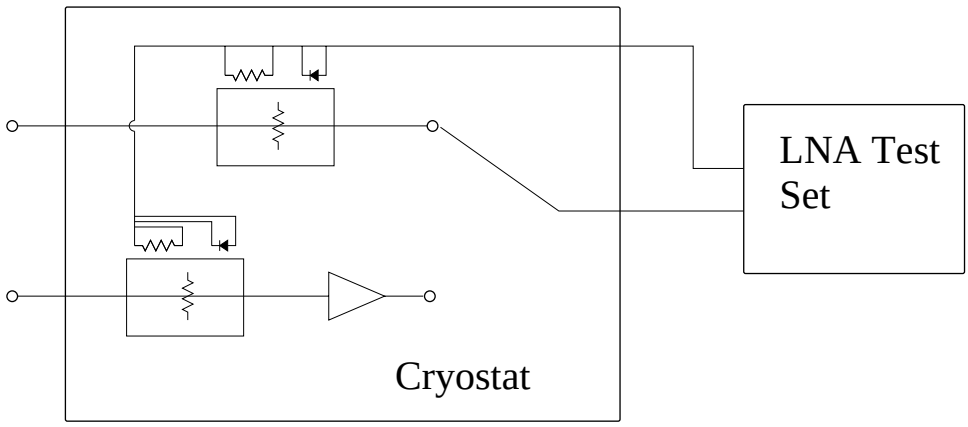

Figure 3.5 Configuration of the amplifier test cryostat for the cold attenuator method. The gain can be viewed with a network analyzer while setting DC bias levels. The cryostat inputs can be terminated, and the amplifier noise measured as described in Section 3.3. With this setup, the noise can also be measured using a room-temperature noise generator as the power source.

One immediate advantage of this setup is that the magnitude of the gain can now be measured directly with a network analyzer. The switch allows the attenuators and the cabling in the cryostat to be calibrated out with the network analyzer's built-in "response" calibration system. The bias of the amplifier can then be adjusted while watching the gain to find conditions with a smooth passband and low power consumption.

Although I haven't actually tried it, this setup can also be used to watch the noise temperature in a chosen frequency channel real-time while adjusting the bias of the amplifier. The frequency of the local oscillator would first be set to select the channel. A noise diode would be connected to the appropriate input cable of the cryostat. The cold attenuators would reduce the input power to achieve maximum accuracy. Since there are still two unknowns, i.e., gain and noise, the noise diode would be switched on and off at a rate of perhaps tens of Hertz. The computer would calculate the gain and the noise from each on-off cycle and display them while the user adjusts the amplifier bias. The computer could also perform fast frequency sweeps with this system since it would no longer be necessary to wait for heated terminators to cool down. Once the optimum bias conditions were found, an independent determination of the noise could be obtained by heating the attenuators as described in Section 3.4.3.

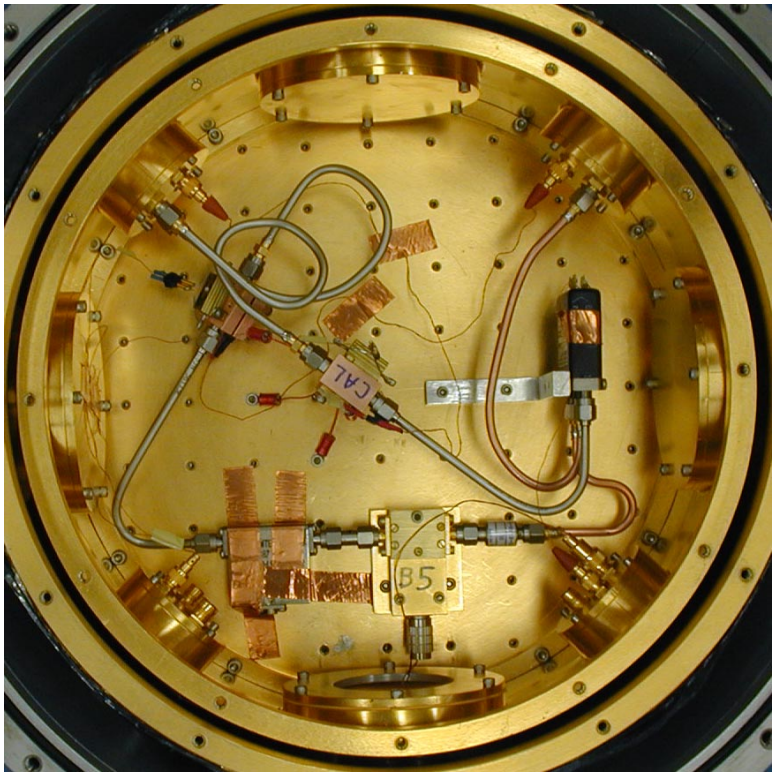

Figure 3.6 Amplifier test cryostat for the cold attenuator method. The amplifier under test is the gold box in the lower center, labeled B5. Two signals enter the cryostat in the upper left corner through stainless steel coaxial cable. Both signals pass through heated attenuators before connecting to the switch (for calibration) or the device under test. The signal exits the cryostat through the copper coaxial cable in the upper right. The device covered with copper tape to the left of the amplifier is a 4-8 GHz cryogenic isolator, which was also being tested when this photo was taken.

Chapter 4
A 4-8 GHz QMMIC Low-Noise Amplifier

4.1 Overview

Low-noise microwave amplifiers based on cryogenically-cooled high electron mobility transistors (HEMTs) are currently the state of the art up to about 100 GHz (Duh et al. 1988; Pospieszalski et al. 1988). This chapter describes a 4-8 GHz quasi-monolithic microwave integrated circuit (QMMIC) HEMT amplifier designed for use at the IF of submillimeter-wave heterodyne receivers. The QMMIC consists of a thin-film passive circuit on a GaAs substrate with three 160 μm gate InP HEMTs bump-bonded to it. The measured amplifier gain is over 32 dB and noise is approximately 8 K from 4 to 8 GHz at a physical temperature of 4.2 K.

4.2 Design Goals

The amplifier was designed to operate at 4.2 K in a liquid helium cryostat. The gain needed to be at least 30 dB to reduce the effect of the noise from subsequent room-temperature stages to negligible levels, and the target gain flatness was $\pm$1.5 dB or better. Noise performance is critical; the target noise temperature referred to the input was 5 K or less across the band. Other design goals included low power consumption to minimize cryogen boil-off, unconditional stability against oscillation at all frequencies both in and out of band, and a compact housing.

While it's easy to design microwave amplifiers with good output matches, getting a good input match can be challenging. In particular, there is generally a trade-off between optimizing the noise performance and minimizing the reflection at the input. Since a commercially-available 4-8 GHz cryogenic isolator can be used to minimize

the reflection at the input of the amplifier, the input return loss need not be especially low.

4.3 Principles of LNA Design

When designing a low-noise amplifier, both the signal and noise performance must be considered. We saw in Section 2.2 that the noise waves emanating from the different ports of a microwave device can be correlated. The key to designing low-noise amplifiers is to reflect some fraction of the noise wave emanating from the input back into the device with the appropriate phase shift such that it cancels out part of the noise wave emanating from the output (Haus and Adler 1958). The complex reflection coefficient that must be presented to the transistor to achieve this effect is referred to as Γ_{opt}. Figure 4.1 shows a plot of Γ_{opt} for the transistors used in the LNA. It can be seen that a simple 4.3 nH inductor at the gate comes close to noise-matching the transistor in the 4-8 GHz band. The figure also shows that there is a trade-off between designing for optimum signal performance or minimum noise.

The most critical aspect of a low-noise amplifier (aside from the transistors) is the tuning circuit at the input of the first FET. When designing this component, the signal performance is often considered to be secondary to the noise performance. After the input to the first stage of the amplifier has been designed for minimum noise, subsequent stages of the amplifier are tuned to equalize the gain. Matching the output to some particular impedance (in this case, 50 Ω) is normally easy, and is accomplished by connecting a resistor of the appropriate size from the drain of the last transistor to an RF ground. This is important to minimize standing waves on transmission lines connected to the output of the device.

The stability of the amplifier against oscillations must be considered both in and out of band up to the highest frequencies at which the transistors still have appreciable gain. The amplifier can oscillate if the input or the output has reflection gain. Since the reflection at a port depends upon the impedance presented to it, it is desirable to design the amplifier to be unconditionally stable, i.e., stable against oscillations for

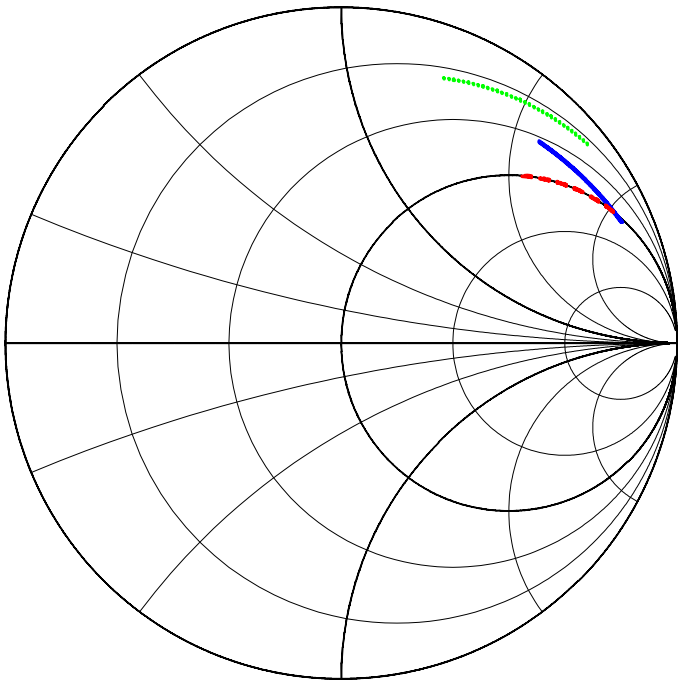

Figure 4.1 Transistor input reflection Γ_{opt} for optimum noise performance. The solid blue curve is the reflection coefficient that, when presented to the input of the FET, would give the lowest possible noise temperature, while the dotted green curve shows the reflection coefficient that would impedance-match the input of the FET. The dashed red curve is the reflection coefficient presented by a 4.3 nH inductor. Note that while Γ_{opt} is moving counterclockwise as the frequency increases from 4 to 8 GHz, the inductor reflection coefficient is moving clockwise. This 50 Ω impedance Smith chart is a polar plot of the reflection coefficients: the center corresponds to no reflection (i.e., a matched load), while the outer circle corresponds to total reflection. The phase of the reflection starts at zero at the right side of the polar plot (an open circuit), and increases counterclockwise.

all passive source and load impedances.

4.4 A Single-Ended Quasi-Monolithic Amplifier

Normally, when a low-noise amplifier with a good input match is needed, a balanced design is used (Padin and Ortiz 1991). With this approach, two amplifiers are combined in parallel with 90° hybrids (four port devices used to introduce 90° phase shifts) such that the reflections from the two parallel stages add 180° out of phase and cancel themselves out. This frees the designer to match the transistors for minimum noise. Balanced designs work well for moderate bandwidths up to a little over an octave; beyond that, it becomes difficult to make good hybrids. Unfortunately, balanced designs have a few drawbacks. Having two amplifiers in parallel would increase the thermal load on the cryostat, and the extra input circuitry adds loss, which increases the noise temperature. Because of these drawbacks, we chose to use a simpler single-ended design and put an isolator at the input to prevent standing waves. The isolator, like a 90° hybrid, adds loss that increases the overall noise temperature, but the single-ended amplifier only generates about half the waste heat of its balanced equivalent, and is easier to design, build, and fabricate.

The initial reason for considering using a MMIC was to gain better control over parasitics compared to a discrete-component amplifier. However, fabrication of MMIC devices is expensive due to tiny features in the transistors. Choosing a quasi-MMIC approach not only greatly reduces the fabrication costs, it also permits the selection of transistors from known good wafers. The relative ease of assembly associated with the QMMIC devices was also attractive, and bump-bonding the transistors creates a robust circuit free from wire bond parasitics. Other advantages of the QMMIC approach include small size and relatively easy adaptability to different packaging constraints. For example, the QMMIC amplifier could more easily be integrated into the mixer block of an SIS receiver than a discrete-component amplifier.

4.5 The Transistors

The transistors are 160 μm gate InP HEMTs provided by the Microwave and Lidar Technology Section at the Jet Propulsion Laboratory. The transistors were measured two ways. Some transistors were measured directly with a microwave probe station and network analyzer. Others were bump-bonded to simple coplanar waveguide (CPW) substrates, and probed including some length of CPW line. The measured scattering matrices of the bump-bonded transistors were mathematically deembedded from the CPW lines to arrive at measured scattering matrices for bump-bonded transistors. It was found that the differences between the bare and bump-bonded transistors were small.

Marian Pospieszalski's FET model (Pospieszalski 1989) was fit to the measured data using the SuperMix optimizer to determine the model parameters, see Section 2.7. The noise prediction from the model, given a best-guess value of 430 K for the noisy drain-resistor temperature, was used without any direct measurement of the transistor noise parameters.

4.6 Design and Simulations

Different tuning circuits for the amplifier were evaluated by first designing them to noise-match 50 Ω to $\Gamma_{\rm opt}$ at the band center, then using SuperMix to optimize the designs across the full band for flat gain above 30 dB, low noise, input reflections below about -10 dB, output reflections below -25 dB, and unconditional stability at all frequencies. During this initial design phase, efforts were made to keep the total power consumption low by minimizing resistive elements in the drain current path. The final design chosen for layout used inductive tuning at the transistor gates, some source inductance for stability, gates biased through large resistors (large enough to not couple appreciable noise into the gate), and resistively biased drains.

After the ideal circuit designs were completed, physical resistors, capacitors, and inductors were laid out. The substrate includes air bridges and a resistive layer, but

Layer	*Thickness*
Bump Gold	8 μm
Air Bridge Gold	1 μm
Air	2 μm
SiN	296 pF/mm^2
Gold	1 μm
NiCr Resistor	50 Ω/square
GaAs	250 μm

Table 4.1 Layers of the QMMIC Substrate

for ease of fabrication does not include via holes. Each component, including the spiral inductors, was simulated with Agilent's Momentum electromagnetic (EM) field simulator (Agilent Technologies). Results of the EM simulations were saved as scattering parameter files, which were then imported back into SuperMix for the final simulation. At this point, the predicted results including field simulations differed enough from the original design that the amplifier was re-optimized, and the component layouts modified accordingly. Two designs were selected for fabrication, one optimized for best performance (Figure 4.2), and one optimized for greater stability. The final simulation is listed in Appendix F. The predicted gain and noise are shown in Figure 4.3.

The DC gate and drain bias lines for each transistor were kept separate to reduce power consumption on the cryogenic stage and allow the performance to be fine-tuned. Each gate bias line starts with a voltage divider before passing through an RC filter network. By dropping the gate bias voltages by a factor of 10, the dividers both protect the transistors and reduce the effects of noise on the bias lines. RC filter networks are also used on the drain bias lines.

4.7 Mask Layout

The layers of the QMMIC substrate are shown in Table 4.1, and the layout is shown in Figure 4.4. The substrate is gold-backed 250 μm GaAs. The input is coplanar waveguide (CPW) at the left edge of the chip. From left to right, the signal passes

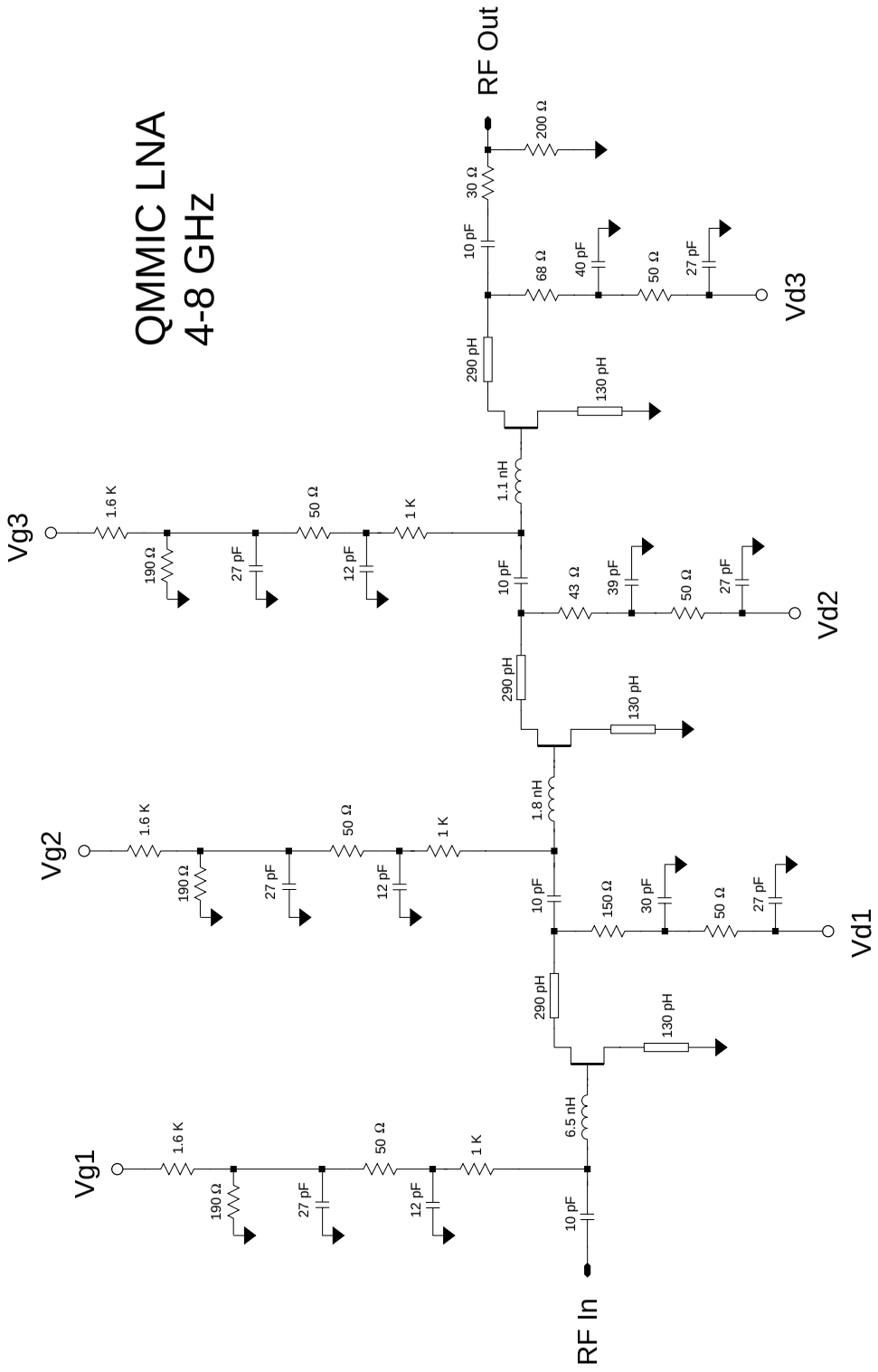

Figure 4.2 Amplifier schematic.

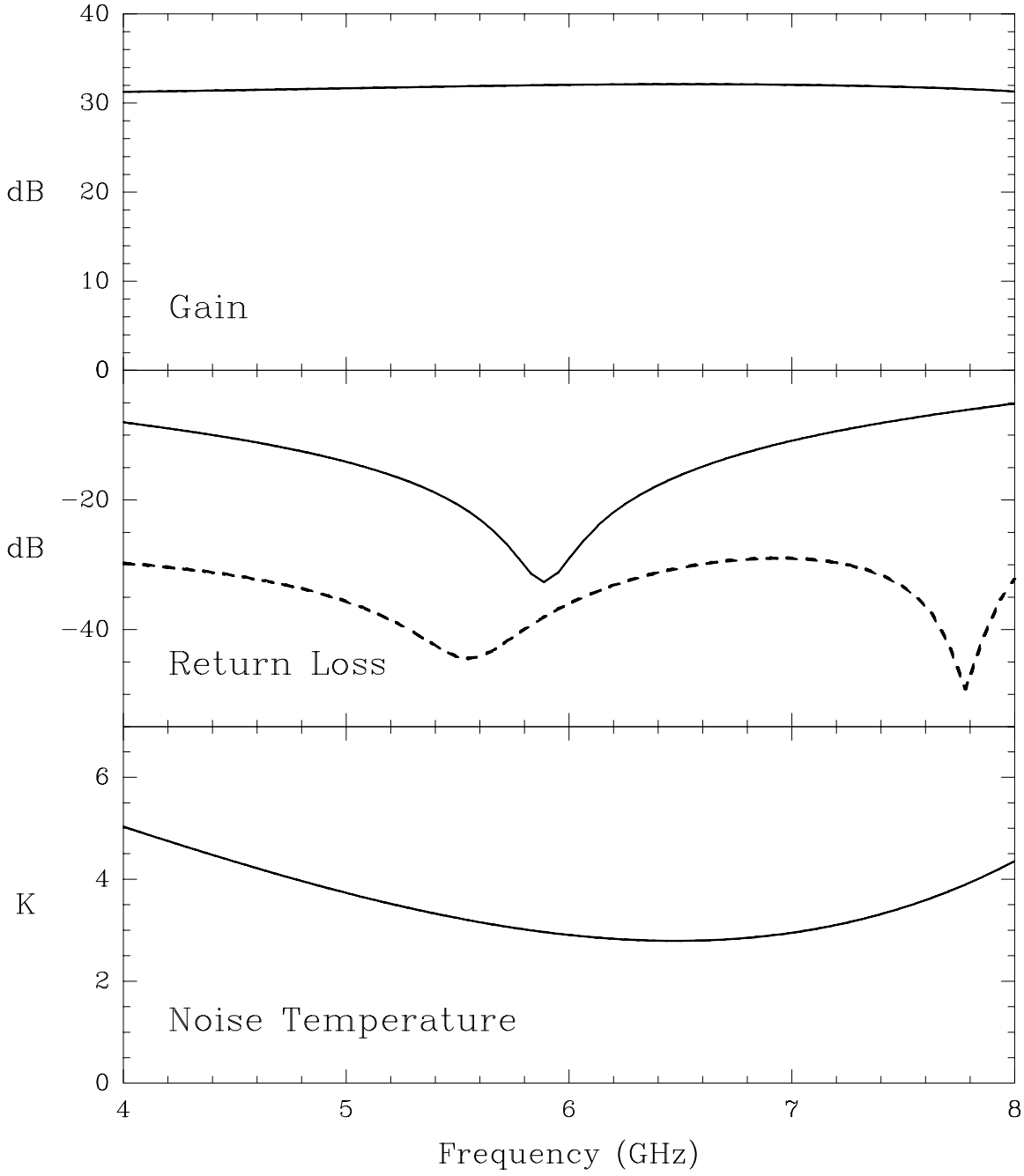

Figure 4.3 Predicted signal and noise performance of the QMMIC amplifier. The output return loss is shown with a dashed line, and the input with a solid line.

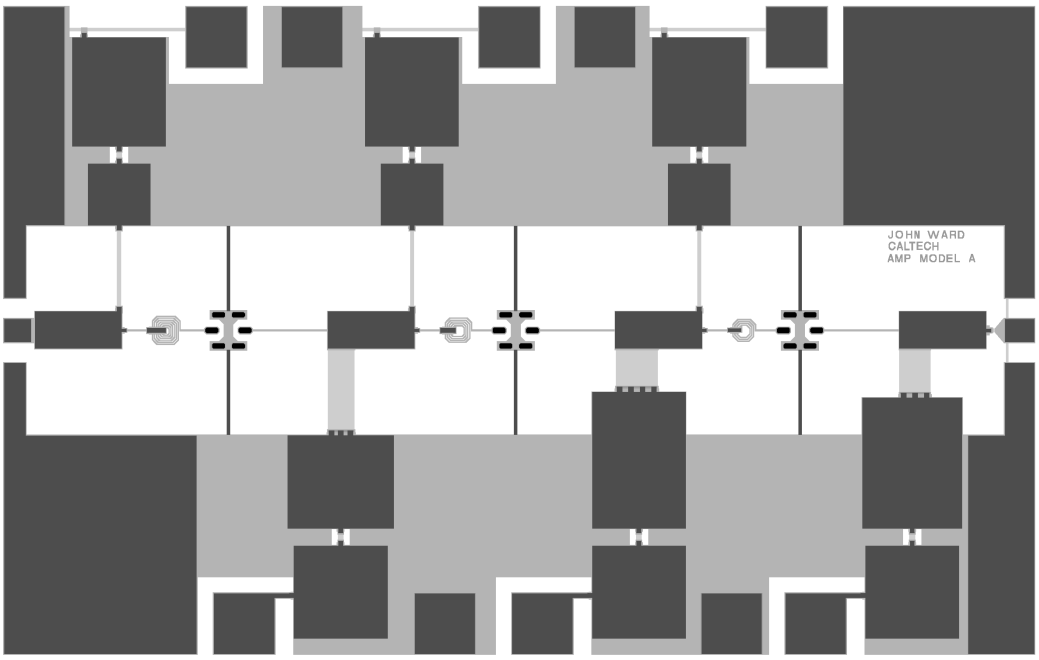

Figure 4.4 Mask layout of the QMMIC substrate. The actual size is approximately 2.5×3.8 mm. The InP HEMTs are bonded to the three pads spaced horizontally across the center of the chip. The input is coplanar waveguide on the left, and the output is on the right. There are three bond pads at the top for the gate bias, and three across the bottom for the drain bias.

through a large DC blocking capacitor, is biased from above through a long, thin resistor, passes through a spiral inductor, and ends in a bump pad for the transistor gate. The transistor sources are grounded through long, thin lines above and below the transistor to add some inductance to provide stabilizing negative feedback. The output of the drain continues to the right through an inductive transmission line, and is biased from below through a wide resistor at the DC blocking capacitor. This pattern repeats three times, ending in the CPW output at the right. Resistive elements just before the output bond pads are used to match the output to 50 Ω.

The top half of the chip has an RC filter network for each gate, ending in a bond pad after a voltage divider. The bottom half of the circuit has RC filter networks for the drain bias. Resistances in the drain bias lines are kept relatively small to minimize power consumption.

All of the wire bond pads have a double thickness of gold for added strength.

Ground bond areas were added all around the chip. In later testing, it was found that good grounding is important to eliminate substrate modes.

4.8 Transition Circuits

The input and output of the QMMIC chip are laid out in coplanar waveguide (CPW), both to avoid via holes and to allow the devices to be tested on a probe station. A separate circuit was designed to convert from the QMMIC CPW to microstrip; the microstrip-end of this circuit can in turn be soldered to an SMA connector pin. The thickness and dielectric constant of these transition circuit boards were chosen to roughly match those of the QMMIC chip. Ground plane spacings for 50 Ω CPW were calculated for center conductor widths ranging from the QMMIC CPW value to the width of 50 Ω microstrip. These values were used to lay out the transition circuit board. Via holes were used to connect the top and bottom ground planes. The Momentum EM field simulator predicted reflections below -34 dB in the 4 to 8 GHz band for the transitions.

4.9 The Housing

The amplifier housing was designed to be compact (Figure 4.5). The microwave and bias circuits were split into two separate cavities on opposite sides of the housing. This way, the microwave side could be kept small to eliminate in-band cavity resonances (Figure 4.6). DC bias for the transistors was brought up to the microwave cavity from the DC cavity using small feed-thru pins. The DC cavity contains filtering capacitors and provides space to add overvoltage protection diodes.

The microwave connectors are SMA. The size of the housing was determined by the DC bias circuit board and the DC bias connector. The housing was made of brass and was finished in wire-bondable gold.

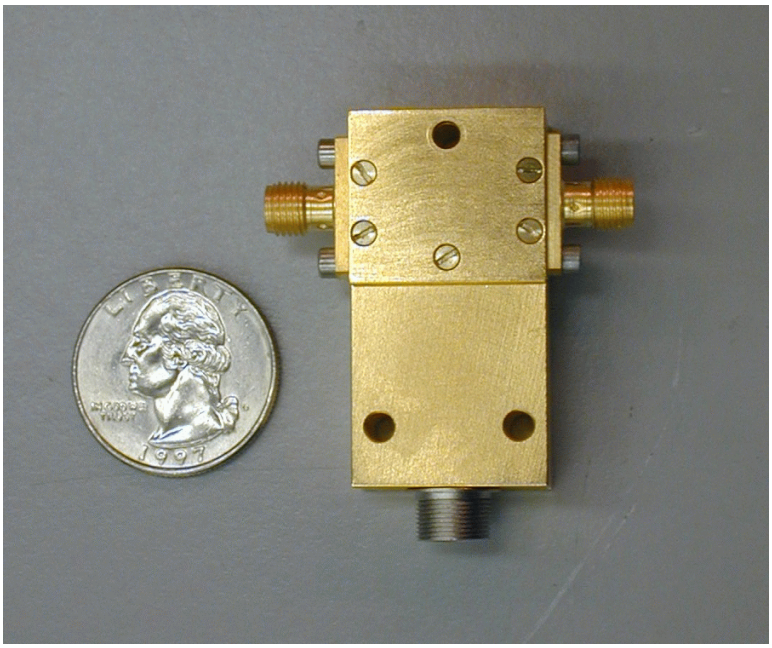

Figure 4.5 The assembled amplifier. The lid between the SMA connectors covers the microwave cavity.

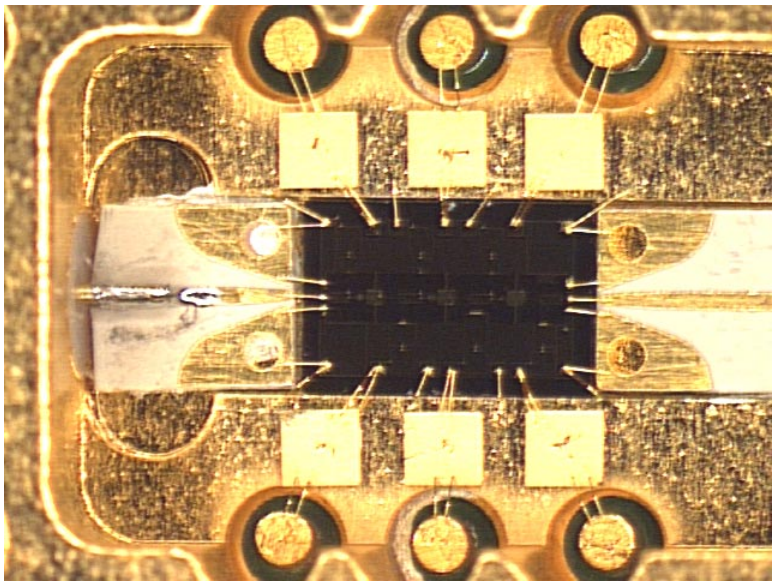

Figure 4.6 The QMMIC chip mounted in the microwave cavity. The signal enters from the left, is transformed to coplanar waveguide by the white circuit board, then enters the GaAs chip. The DC bias lines are brought into the cavity via the six gold posts, and are wire bonded to parallel-plate capacitors for filtering before connecting to the QMMIC chip.

4.10 Measured Results

A QMMIC LNA was tested at 4.2 K. The gain was found to be above about 32 dB, and the noise ranged from 6 to 12 K (Figure 4.7). The power consumption was 8 mW, corresponding to a liquid helium boil-off rate of 270 mL per day.

Some of the differences between the measured results and the model predictions in Figure 4.3 were expected. The measured gain is higher than the prediction because the FET transconductance increases as the device is cooled. The return loss was measured at room temperature, where the resistivity of the NiCr layer was 7.4% larger than the 4.2 K design value. Since the impedance of the output of the chip is set by a network of resistors, it is likely that the output return loss improves when the device is cooled. The ripple in the measured gain and noise are artifacts of the measurement process; the impedances of the heated terminator and the stainless steel coaxial cable in the calibrated noise source (Section 3.4.1) probably shift when cooled to 4 K, causing an impedance mismatch and standing waves on the cable.

As for unexpected differences, the measured noise is larger than the prediction, and the noise minimum is shifted to higher frequency. This can be explained by some combination of the effective drain resistor temperature being higher than expected, the losses at the input of the amplifier being higher than expected, and the inductance being slightly lower than expected. Increasing the drain resistor temperature in the FET model both increases the noise and shifts the minimum to higher frequency. A decrease in input inductance would also shift the noise minimum upward in frequency. Extra losses in the input circuitry might come from some combination of the connector, the microstrip-to-CPW transitions, the wire bonds, and the spiral inductor. The measured noise curve is matched well by a drain resistor temperature of about twice the expected value (860 K instead of 430 K), a 3% decrease in the input inductance (0.2 nH), and a 0.6 dB increase in the input loss.

To better understand the measured noise, more amplifiers should be tested. For example, it's possible that the input transistor is a statistical outlier with higher than usual noise, or that the transistors were slightly damaged by the high heat of

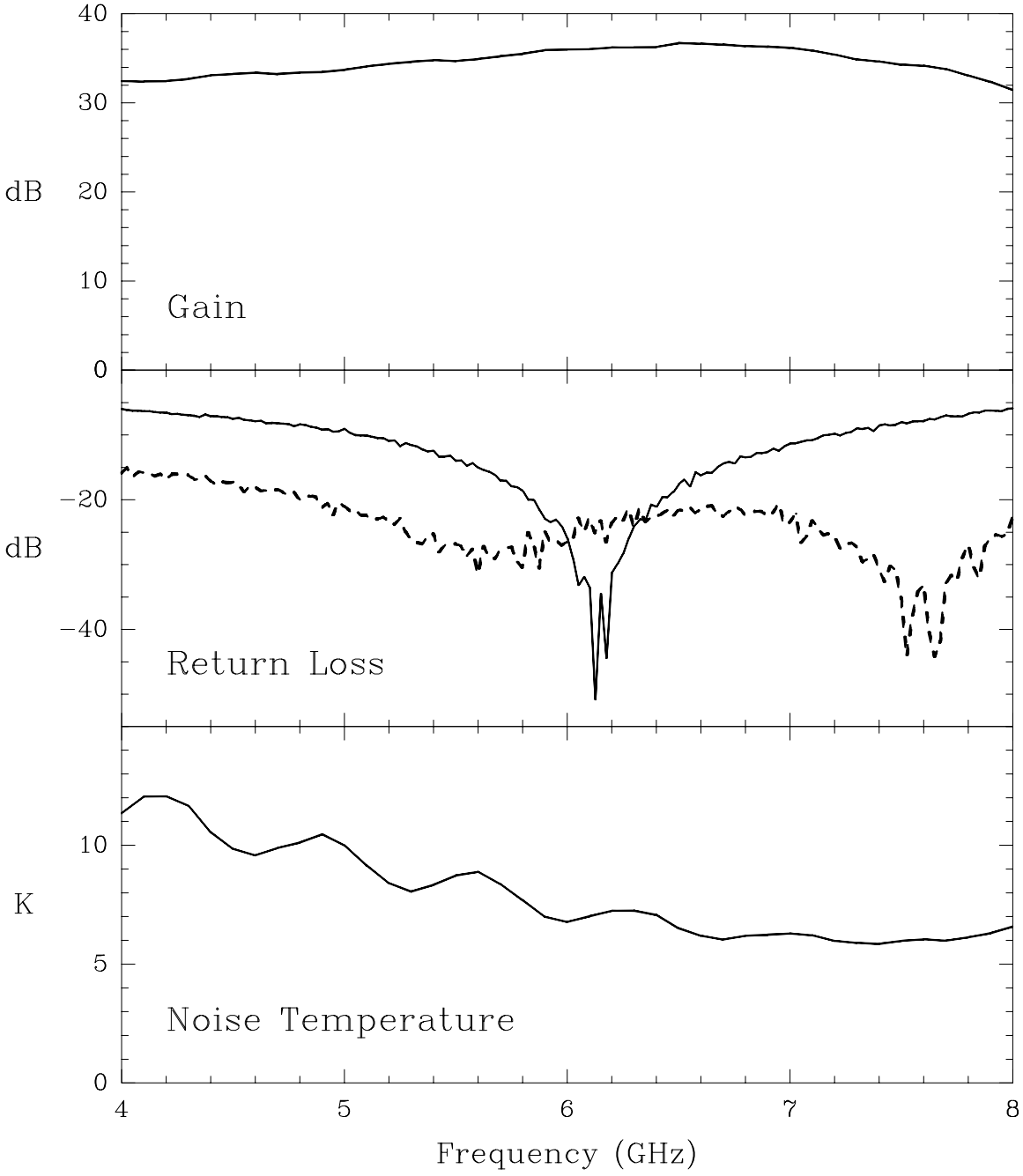

Figure 4.7 Measured signal and noise performance of the QMMIC LNA. The output return loss is shown with a dashed line, and the input with a solid line. The gain and noise temperature were measured at 4.2 K, and the return losses at room temperature.

the bonding process. To test these possibilities, it would be desirable to bond more amplifiers at a lower temperature, test the second QMMIC chip design that was fabricated but never bonded, and try transistors from different wafers or fabrication runs.

The deviation of the measured 4.2 K gain from flat is ±2.5 dB. At 77 K, the gain is flat to within better than ±1 dB. It is not clear why the shape of the gain changes as the device is cooled from 77 to 4.2 K. It's possible that there is some coupling from the chip output back to the input via a substrate mode. If S_{21} were the forward scattering parameter in the absence of the supposed substrate mode, and the reverse coupling were described by the complex scattering parameter τ, then the forward scattering parameter in the presence of the substrate mode, call it S'_{21}, would become

$$S'_{21} = \frac{S_{21}}{1 - \tau\, S_{21}} \,. \tag{4.1}$$

Cooling increases S_{21}, which would make the feedback stronger at low temperature, thus explaining the temperature-dependence of the effect. Since the phases of S_{21} and τ are expected to vary with frequency, the effect of the reverse coupling would be to alternately increase and decrease the gain across the passband.

If feedback via a substrate mode is the reason why the cold gain is not flat, then there are several potential solutions. First, grounding the chip better would help kill off the mode. Reducing the gain of the amplifier by changing the bias of the second or third stage HEMT would reduce the feedback. If these simple solutions were to prove to be insufficient, then the gain could be further reduced by redesigning the chip as a 2-stage amplifier. Two chips could then be cascaded to provide the required overall gain.

Chapter 5
A 690 GHz Wide Spectral Bandwidth Heterodyne Receiver

5.1 Overview

The rotational velocities of galaxies are typically hundreds of kilometers per second, creating large Doppler shifts that broaden spectral lines. The CSO has an excellent facility 565-690 GHz receiver (Kooi et al. 1994), but it is limited to observing 1 GHz of spectrum at a time. To observe a galaxy with this receiver, it is usually necessary to retune the receiver during the observations to observe the line in pieces. Doing so at least doubles the required integration time and significantly decreases measurement accuracy by hampering the subtraction of systematic intensity offsets.

The primary design goal for the new instrument described here was to be able to observe entire extragalactic CO J=6→5 emission lines with a single receiver tuning, including adequate baseline on either side of the emission line for optimum baseline subtraction. Single-dish submillimeter heterodyne observations of weak sources are normally made in beam-switching mode. The antenna is alternately pointed at the source and at a nearby region of blank sky at a rate of about a Hertz. The off-source observations are subtracted from the on-source observations to remove the system noise. Unfortunately, the subtraction is not perfect, so the final spectrum typically has some (hopefully small) intensity offset that must be subtracted out in subsequent data reduction. It is effectively impossible to determine this offset if the observed spectrum does not include some baseline. Furthermore, the error in the determined offset is inversely proportional to the square root of the frequency bandwidth used in the determination. Thus, ideally, the frequency width of the baseline should be

at least as large as the width of the observed emission line so that the error of the subtraction of the offset does not dominate over the noise within the emission line itself. The sources with the broadest submillimeter spectra, such as Arp 220, have emission line widths of about 2 GHz in the CO J=6→5 transition. Thus, a target spectral bandwidth of 4 GHz was chosen for our receiver. It should be noted that the spectral bandwidth of the receiver is only useful if teamed with a comparable spectrometer; a 4 GHz analog correlator spectrometer was developed concurrently with the receiver (Harris and Zmuidzinas 2001).

The receiver uses SIS junctions as the mixing element for their high sensitivity at submillimeter wavelengths. SIS junctions use the photon-assisted tunneling of electrons through an insulating barrier to coherently detect radiation in the 100 to 1,200 GHz range with a sensitivity approaching the quantum limit imposed by the uncertainty principle (Tucker and Feldman 1985; Bin 1997). A tunerless quasi-optical design was chosen for ease of construction and use. Despite the absence of tuners, the RF bandwidth of the mixer comfortably covers the entire 650 GHz atmospheric window (see Figure 1.5). An added benefit of the broadband tunerless mixer is that since the conversion loss in the two sidebands is nearly equal for any particular LO frequency, calibration uncertainties due to receiver sideband imbalance are small.

Under excellent conditions for observation of CO J=6→5, with 30% transmission through a 275 K atmosphere, the system temperature assuming a noiseless single sideband receiver would be 640 K, or 1300 K if observing with a double sideband receiver. The system temperature using a state-of-the-art 150 K receiver operating in double sideband mode would be around 2,300 K. Thus, the noise from the receiver is significant when observing under optimal conditions, and so must be carefully minimized. If the beam-switched telescope integrates on-source 35% of the time and the telescope beam efficiency is 30%, then for a system temperature of 3,000 K, the RMS noise per 30 MHz channel after one hour of observing would be 70 mK.

5.2 Characterization of Submillimeter Receivers

Measuring the noise performance of an SIS receiver is similar to measuring the noise of a low-noise amplifier as described in Chapter 3. At millimeter and submillimeter wavelengths, however, a sheet of black absorbing material is used for the noise source instead of the 50 Ω terminators used for the lower-frequency tests. The total IF power of the receiver is measured first with a room-temperature absorber in the receiver beam, then again with the absorber cooled to 77 K by dunking it in a liquid nitrogen bath. The double sideband noise temperature is then calculated using the standard Y-factor formula

$$T_{DSB} = \frac{T_h - T_c}{Y - 1} - T_c \ , \tag{5.1}$$

with $Y \equiv P_h/P_c$. This formula implicitly assumes that the brightness temperatures of the loads are equal to their physical temperatures, i.e., it assumes the Rayleigh-Jeans approximation. In reality, the brightness temperature of the 77 K load at 690 GHz calculated with the Planck formula is 62 K. However, given that the load is almost certainly not entirely black, and therefore scatters some ambient-temperature radiation into the cryostat, this practice may not be entirely unreasonable.

The frequency response of a submillimeter receiver across its RF passband can also be evaluated using a Fourier transform spectrometer (FTS). For this measurement, the mixer is treated as a direct detector by measuring the SIS current rather than the IF power. See Belitsky et al. (1995) or Bin (1997) for a complete description of the use of Fourier transform spectrometers to characterize SIS receivers.

Usually, the performance of a receiver is evaluated almost exclusively based on its noise temperature as a function of LO frequency calculated using the total power technique described above, since it is normally assumed that other parameters such as the shape of the IF passband have little effect on the receiver's sensitivity for astronomical use. Nonetheless, other measurements are still useful for research and development purposes. I measure both the receiver gain and the noise temperature

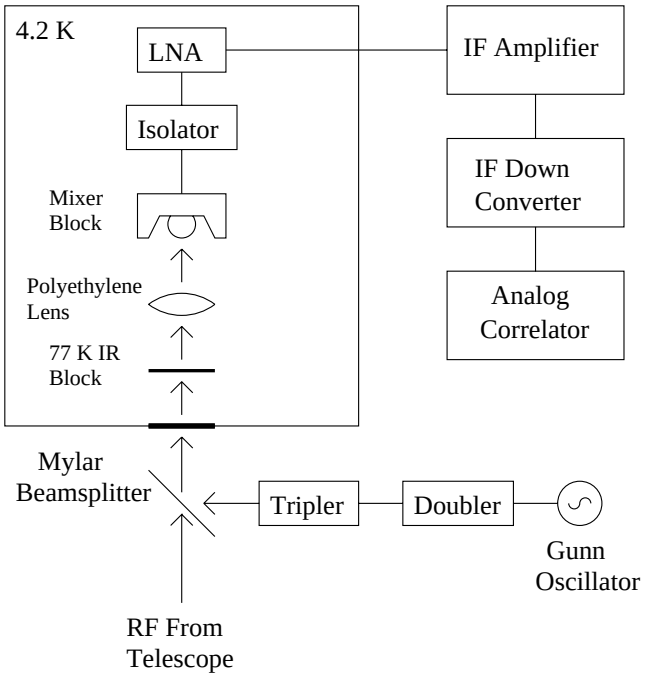

Figure 5.1 Configuration of the receiver.

across the IF passband using the spectrum analyzer described in Section 3.2. The IF spectrum is measured with ambient and then 77 K absorbers in the receiver beam, then the noise temperature and gain of the entire system up to the IF connector of the cryostat are calculated at each frequency channel using equations 3.3 through 3.6.

5.3 Receiver Configuration

A block diagram of the receiver is shown in Figure 5.1. The local oscillator (LO) is generated by a tunable Gunn oscillator (Carlstrom et al. 1985) and multiplied by $\times 2$ and $\times 3$ varactor multipliers (Zimmermann). The LO is combined with the RF signal through a 13 μm mylar beam splitter, and then enters a liquid helium cryostat through a Teflon-coated quartz pressure window. A 77 K Zitex filter blocks infrared radiation. The LO and signal then pass through a polyethylene lens and into a silicon hyperhemisphere anti-reflection coated with alumina-doped epoxy. The hyperhemispherical lens focuses the signal and LO onto a twin-slot antenna, which is used for its nearly-circular beam profile. Microstrip lines match the signal from the

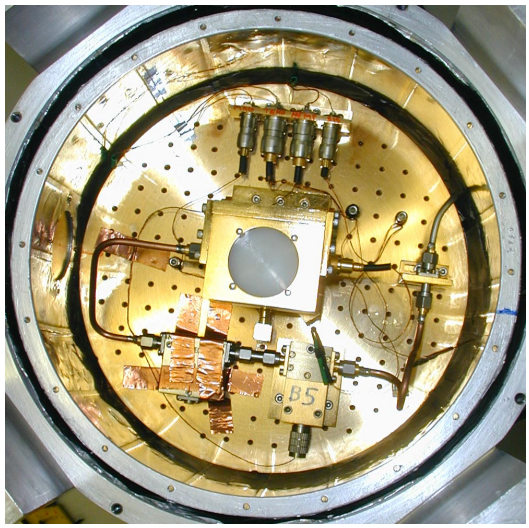

Figure 5.2 Cryostat cold surface. The RF and LO signals pass through the polyethylene lens in the center of the photo before entering the mixer block. The IF signal exits the mixer block via the coax cable to the left, goes through the isolator (under copper tape), through the LNA, and then exits the cryostat in the upper right.

slots into a pair of niobium SIS junctions.

The IF signal is coupled out of the mixer chip through wire bonds to a microstrip circuit that matches the impedance to 50 Ω. The signal then passes through a 4–8 GHz isolator, and into the low-noise amplifier (Chapter 4). The signal then leaves the cryostat, is amplified by a 4–8 GHz room-temperature stage, down-converted to 0.5–4.5 GHz, and analyzed by a 4 GHz analog correlation spectrometer. Figure 5.2 shows the cold surface of the cryostat.

5.4 The SIS Mixer Chip

A photograph of the mixer chip is shown in Figure 5.3. This type of mixer, with twin slot antenna, dual SIS junctions, and hyperhemispherical lens, has already been discussed extensively in the literature, and so won't be described in detail here (Zmuidzinas and LeDuc 1992; Zmuidzinas et al. 1994; Zmuidzinas et al. 1995). The geometry of the chip is presented by Gaidis et al. (1996) as device number 72.

Radial stubs couple the signal from the slot antenna into microstrip tuning circuits, which in turn couple the signal into a pair of SIS junctions. To minimize loss, the

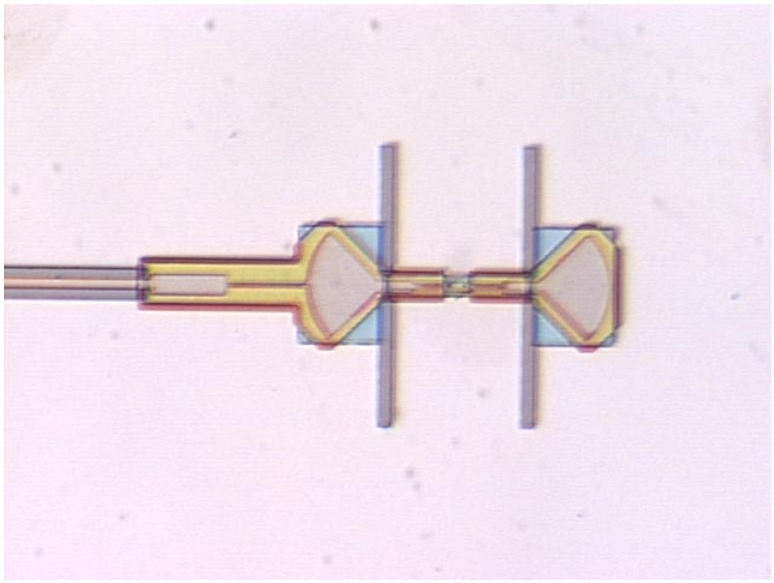

Figure 5.3 The SIS chip. The vertical lines form the slot antenna. The RF and LO signals couple to the antenna through a silicon hyperhemispherical lens underneath the chip. The SIS junctions are the black dots near the center of the "H." The IF signal exits through the transmission line on the left.

ground plane under the microstrip and forming the slots is made of superconducting NbTiN (Tc=15–16 K), and a superconducting niobium film is used for the wiring. NbTiN has only recently been used in SIS mixers (Kawamura et al. 1999). The excellent performance of this receiver demonstrates that NbTiN has low loss around 600–700 GHz. The chip is fabricated on a silicon substrate, and is glued to the anti-reflection coated silicon hyperhemispherical lens. A transmission line to the left of the antenna carries the downconverted IF signal to a wire bond pad.

The SIS mixer chip was originally designed for use with a 1–2 GHz IF system. In order to characterize the mixer so that an IF matching circuit could be designed to use the chip with the 50 Ω, 4–8 GHz low-noise amplifier described in Chapter 4, the mixer was first tested with a 1–2 GHz IF. The current-voltage (IV) curves of the pumped and unpumped mixer were measured for several LO frequencies, and the mixer frequency response was measured with a Fourier transform spectrometer (FTS). The IV and FTS data were used to verify SuperMix simulations of the chip, and to constrain the primary unknown parameter, i.e., the normal-state resistivity (or equivalently, the magnetic penetration depth) of the NbTiN film. The best-fit

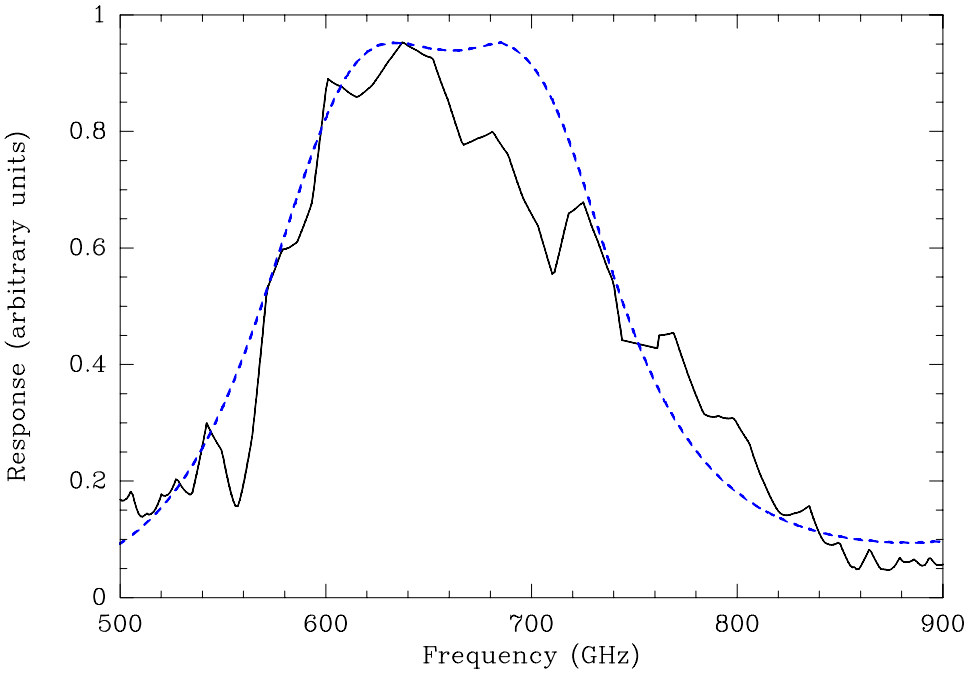

Figure 5.4 FTS response of the mixer. The measured response is shown with the solid line, and the simulated response with the dashed line.

resistivity was 59 $\mu\Omega$ cm, which corresponds to a penetration depth of 0.2 μm. The measured and simulated receiver FTS responses are shown in Figure 5.4.

5.5 The IF Matching Circuit

The IF impedance of the mixer chip was calculated with the now-verified SuperMix model. The IF impedance calculated by SuperMix can be approximated with a parallel RC equivalent circuit (Figure 5.5). The equivalent capacitance is actually the combination of the total electrical capacitance of the circuit on the chip and the quantum susceptance of the SIS junctions, while the resistance is close to the dynamic resistance (slope of the IV curve) at the bias point. It was seen that for a fixed bias voltage and LO power, the IF impedance varies with LO frequency (Figure 5.6). In the context of the parallel RC model, the capacitance was found to remain constant while the resistance varies. Similarly, holding the LO frequency constant while varying the LO power also causes the equivalent resistance to vary while the capacitance remains constant. This dependence of the IF impedance on the LO poses a problem, since

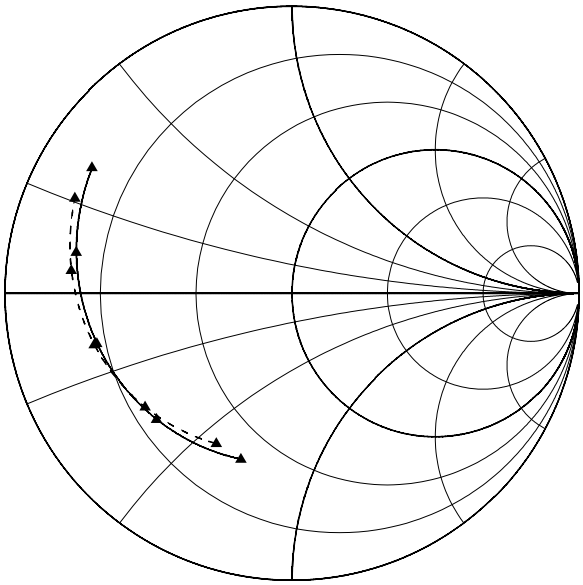

Figure 5.5 IF impedance of the full SIS chip simulation from 4 to 8 GHz compared to a simple parallel RC equivalent circuit. This impedance Smith chart is referred to 50 Ω. The mixer impedance (solid line) is for a bias voltage of 2.15 mV and any LO frequency, as long as the LO power is adjusted appropriately. The parallel RC model (dashed line) is for 109 Ω and 832 fF. Note that wire bond inductance and DC blocking capacitors were included in the impedance calculations.

the IF tuning circuit can only match to some well-defined impedance. It was found that setting the LO power to a specific function of the LO frequency will keep the RC model resistance constant, thus making the IF impedance independent of the LO frequency. A receiver-tuning lookup table was created to give the target SIS current (which is sensitive to LO power) based on the LO frequency to keep the IF impedance at a standard value.

Several considerations had to be kept in mind while designing the IF matching circuit. First of all, the RF return loss is strongly affected by the IF impedance seen by the mixer. For some range of IF impedances, typically for a conjugate-matched IF, there can be reflection gain at the RF port (Ke and Feldman 1992; Kooi et al. 1999). Secondly, the Bode-Fano limit for the return loss when matching the equivalent parallel RC impedance presented by our mixer chip to a real impedance with a lossless passive circuit is about -12 dB for a 4 GHz bandwidth (Bode 1945; Fano 1950a; Fano 1950b). The series inductance added by wire bonds connecting the mixer chip to the

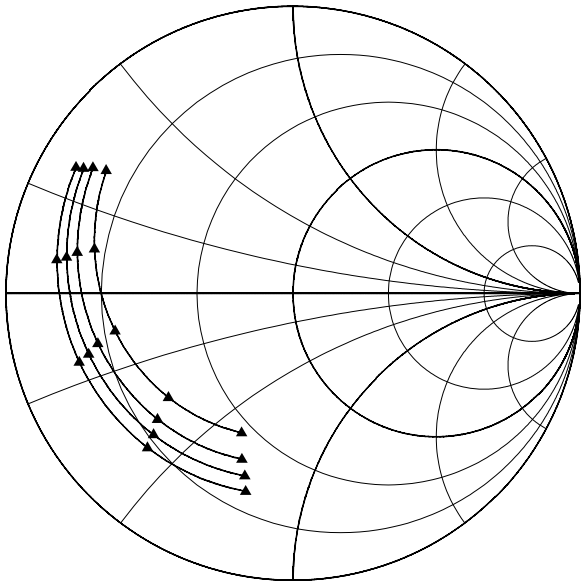

Figure 5.6 IF impedance from 4 to 8 GHz of the SIS chip for various LO frequencies. This impedance Smith chart is referred to 50 Ω. The LO frequencies are, from left to right, 640, 660, 680, and 700 GHz. The bias voltage was 2.15 mV, and the LO power is constant. Note that wire bond inductance and DC blocking capacitors were included in the impedance calculations.

IF circuit board further degrades the achievable limit on the return loss (Kerr 1995). Finally, the primary goal of low system temperature should be achieved while keeping the passband reasonably smooth and flat.

A 2-element microstrip circuit was designed to match the mixer IF impedance to a 50 Ω transmission line. The receiver was then simulated to see how the entire system would perform using this circuit, computing reflections at the RF ports, total receiver noise temperature including the isolator and IF amplifier, conversion loss, etc. The microstrip matching circuit had to be detuned slightly to improve the RF match and eliminate the possibility of RF reflection gain. The circuit was fabricated on a 0.025" thick $\varepsilon_r = 9.8$ TMM 10i circuit board (Rogers Corporation). Figure 5.7 shows a schematic of the matching circuit, and Figure 5.8 shows a photo of the assembled mixer.

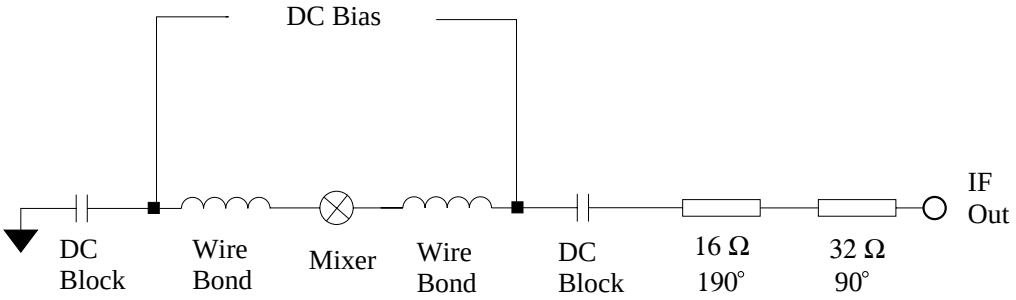

Figure 5.7 Schematic diagram of the IF matching circuit, including wire bonds, DC blocking capacitors, etc. The microstrip phase lengths are referred to 6 GHz.

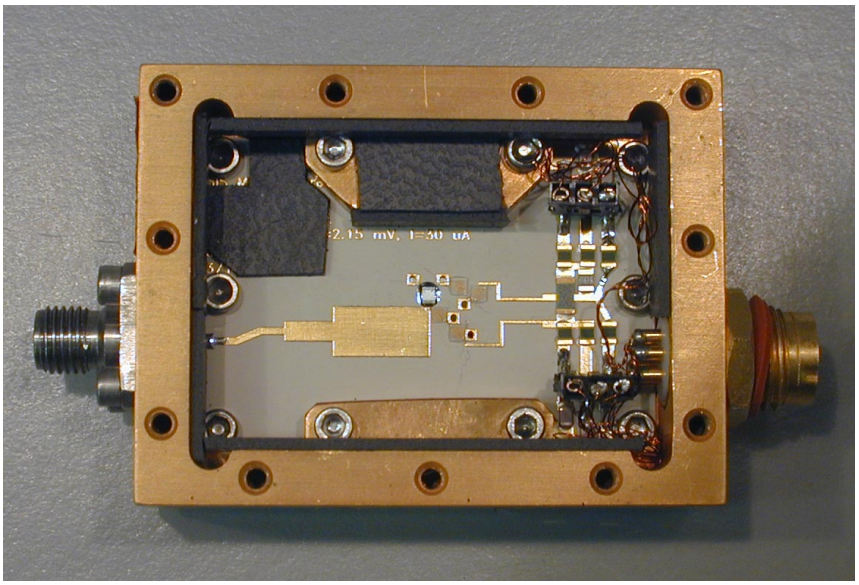

Figure 5.8 The mounted SIS mixer chip and IF matching circuit board. The SIS chip is the small black rectangle in the center. The circuitry to the right of the chip is for DC bias. The microstrip circuit to the lower left of the chip matches the mixer IF to 50 Ω. The dark grey strips are ferrite absorbers.

5.6 Results

The complete receiver was run with the low-noise amplifier described in Chapter 4. The double sideband noise temperature was below 200 Kelvin across most of the IF passband, reaching a minimum of 152 K at 7.2 GHz (Figure 5.9). This noise performance is competitive with the best receivers currently in use (Kooi et al. 1998). Figure 5.10 shows IV curves of the pumped and unpumped mixer along with the total IF power measured with hot and cold absorbers in the beam. For comparison, results of a simulation of the complete receiver (listed in Appendix G) are also included in the figure. To match the measured noise temperatures, the losses from the receiver optics including the beam splitter in the simulation were adjusted to a total of 3 dB, compared to the expected total of 2 dB.

An early version of the receiver was taken to the Caltech Submillimeter Observatory and used with a 500 MHz spectrometer to observe carbon monoxide toward the nearby starburst galaxy M82. The spectra are shown in Figure C.4, and a detailed analysis and discussion of the observations will be presented in Chapter 6. A photograph of the receiver mounted at the Cassegrain focus of the telescope is shown in Figure 5.11.

With a double sideband noise temperature below 200 K across 3 GHz of the IF passband, the corresponding usable bandwidth of the receiver is 1,300 km/s. The increase in the noise at the band edges can be understood by examining the gain curve in Figure 5.9. Power is not being efficiently coupled from the SIS chip into the IF amplifier at the band edges, causing an increase in the noise contribution from the amplifier. There are several things that might cause the coupling to be less efficient than expected:

- The model for the IF impedance of the SIS mixer is incorrect,
- The model for the microstrip impedance transformer is incorrect,
- Incomplete decoupling at the DC bias lines, or
- Effects from the circuit geometry in the vicinity of the SIS chip.

One would naïvely expect the IF impedance of the SIS chip to resemble a resistance

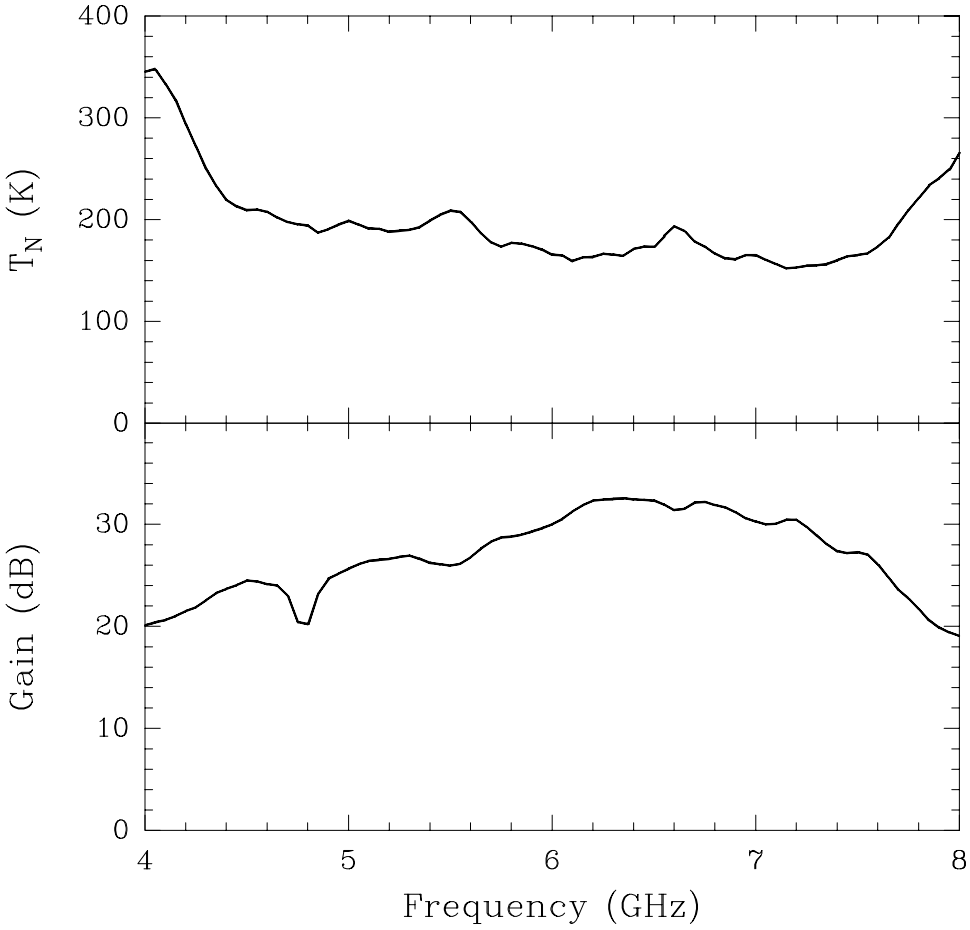

Figure 5.9 Gain and DSB noise temperature of the receiver as a function of IF frequency. The LO frequency was 648 GHz, $V_{SIS} = 2.18$ mV, and $I_{SIS} = 59$ μA. The gain was measured from the input of the beam splitter to the SMA connector at the output of the cryostat.

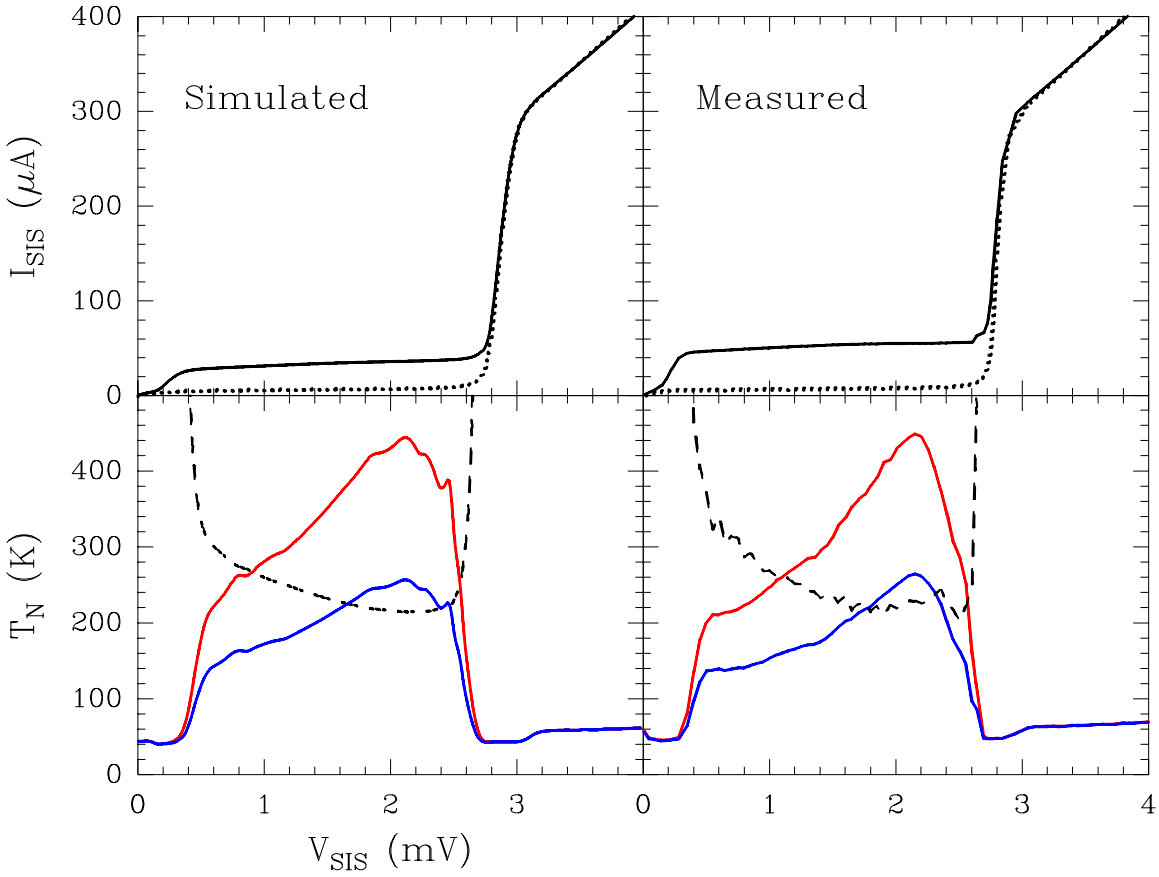

Figure 5.10 IV curves of the pumped (solid lines) and unpumped (dotted lines) mixer with hot and cold IF power. The load temperatures were 77 and 295 K, and the LO frequency was 630 GHz. The IF power is in arbitrary units. Losses in the five optical elements in the receiver simulation were adjusted to a total of 3 dB to match the measured noise temperature (dashed lines).

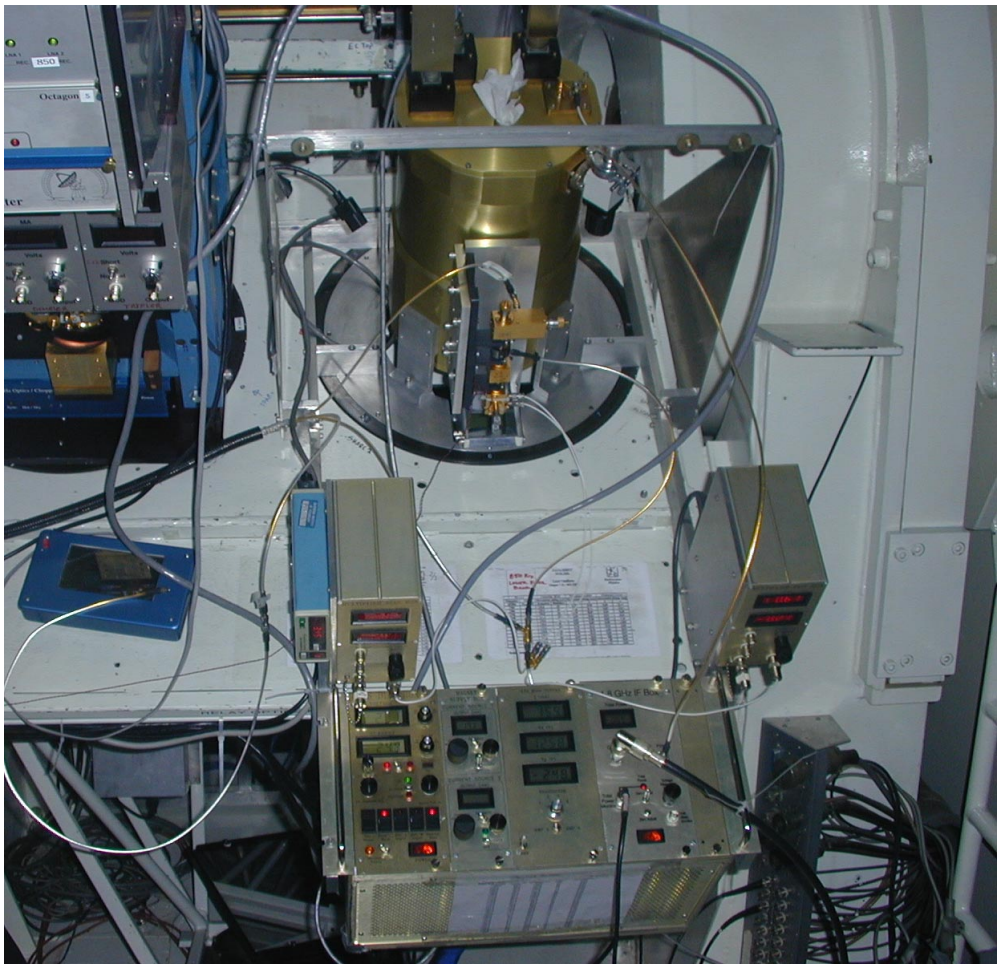

Figure 5.11 Receiver mounted at the Cassegrain focus of the CSO. The receiver is in a downward-looking gold cryostat at the top of the photo. The 690 GHz LO chain is on the front of the cryostat. The rack at the bottom of the photo houses, from left to right, the SIS bias box, the magnet bias box (for Josephson oscillation suppression), the LNA bias box, and the 4 to 8 GHz IF system.

and a capacitance in parallel, with the resistance equal to the dynamic resistance of the mixer IV curve at the bias point, and the capacitance equal to the total electrical capacitance of the circuit on the chip plus some contribution from the quantum susceptance of the SIS junctions. We saw in Section 5.5 that the thorough calculation performed with SuperMix confirmed this expectation. Thus, the mixer IF impedance used for the design is likely to be correct. The microstrip impedance transformer was designed first with a linear circuit solver. Since the microstrip sections are quite wide, semi-empirical equations were used to take end-effects into account. Subsequent simulation with the EM solver Momentum confirmed the original circuit simulation results. So, it is safe to assume that the microstrip model was also correct. Each component of the DC bias lines was measured on a microwave probe station, and the complete bias lines were assembled and tested at room temperature. It is unlikely that the bias lines are degrading the IF passband.

This leaves the details of the circuit geometry in the vicinity of the SIS chip as the mostly likely source of the gain roll-off. To explore this possibility, the region was simulated with the High Frequency Structure Simulator (HFSS) software package (Ansoft Corporation). Figure 5.12 shows a close-up of the HFSS model in the region around the mixer chip. The mixer sits in a 0.090" diameter hole in a 0.025" thick circuit board. The IF signal is brought out of the mixer chip to a low-impedance microstrip line. Two via holes on the opposite side of the chip provide the ground for the IF signal. One potential problem with this geometry might be that the IF ground is connected far from the microstrip line. The physical distance between the ground feed and the signal feed is 2.5 mm; given the circuit board relative dielectric constant of $\varepsilon_r = 9.8$, this corresponds to a phase length of 76° at 8 GHz. The HFSS solutions showed that the via holes and extra ground path length add about 1.5 nH of effective series inductance that was not included in the original models, and so confirmed that these details do have a major impact on the IF impedance and are largely responsible for the gain variations seen in Figure 5.9.

Based on the experience of developing this receiver, there are several improvements that could be made to future designs. We have learned that many details of SIS

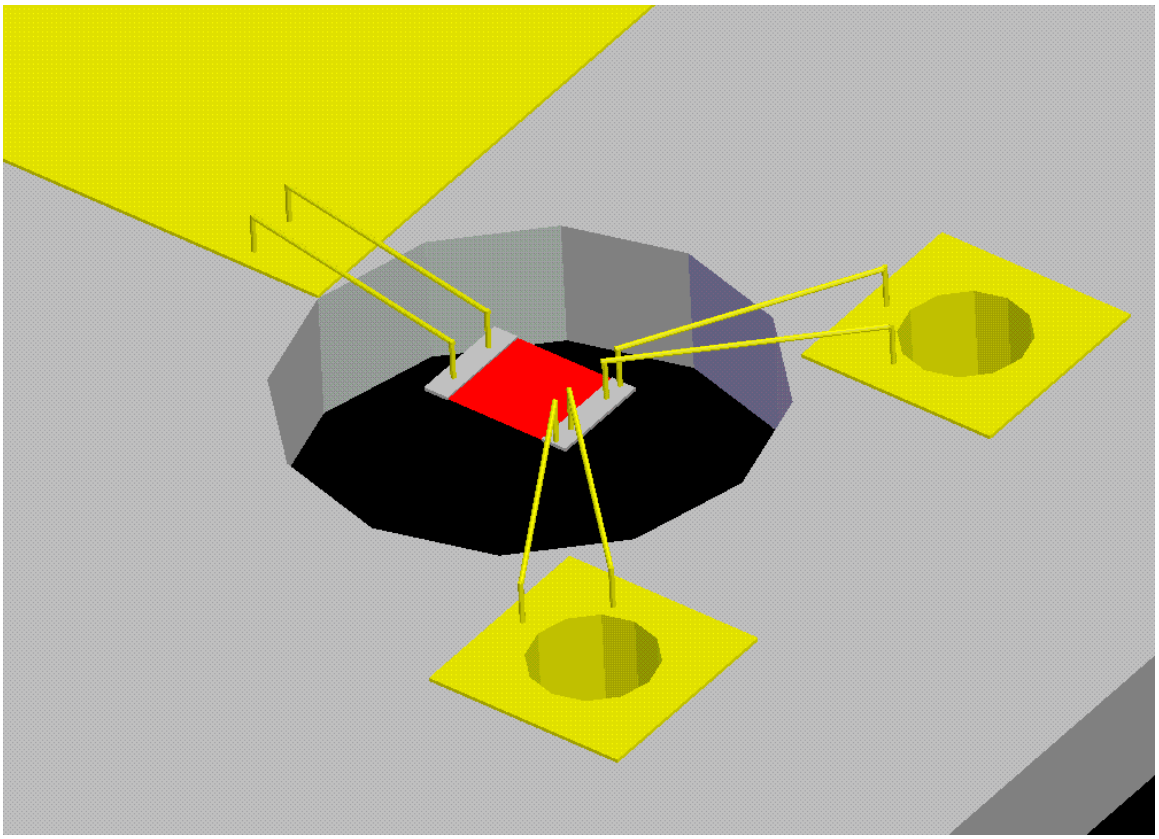

Figure 5.12 HFSS model of the SIS chip feeding the IF circuit. The input port representing the mixer chip sits in a 0.090" diameter hole in the IF circuit board. Wire bonds connect the signal to a microstrip line in the upper left. The ground is connected to two via holes through four wire bonds toward the lower right. The second via hole and the large number of wire bonds are used to reduce parasitic inductances. A photograph of this circuit was shown in Figure 5.8.

receiver design that could be ignored for IF signals below 2 GHz must be carefully dealt with to operate at higher frequencies. First, the capacitance of the mixer chip should be minimized to ease the Bode-Fano limit on the IF match. It would also help to bring both the IF signal and the ground out of the same side of the chip. The IF circuit board should be redesigned to bring the IF ground closer to the microstrip circuit, and to minimize all wire bond lengths. It would be wise to carefully model the complete linear IF circuit starting from the chip including wire bonds with a field simulator such as HFSS to account for geometry-related parasitics. By making these changes, it should be possible to realize low noise and flat gain across IF bandwidths of 4 GHz or wider.

Chapter 6

Observations of the Starburst Galaxy M82

6.1 Introduction

M82, also known as NGC 3034, is a nearby irregular starburst galaxy in Ursa Major, and is seen nearly edge-on. Dust obscures the nuclear region at optical wavelengths. M82 is the brightest IR galaxy in the sky, and has a total IR luminosity of 3.8×10^{10} $L_\odot$ (Colbert et al. 1999). It is believed that the starburst was triggered by a close encounter with M81 about 10^8 years ago (Yun et al. 1993). The bright FIR fine structure lines seen in the inner kiloparsec of M82 imply a far-UV radiation field about 10^3 times larger than the local solar value (Colbert et al. 1999). This strong UV field is generated by a population of massive young stars that also heat the dust which produces the large IR luminosity. The nucleus has a large molecular gas mass, a few times 10^8 $M_\odot$, giving rise to strong CO emission (Wild et al. 1992; Weiß et al. 2001). At an estimated average star formation rate of 1 $M_\odot$ yr^{-1}, this gas will be consumed in about 2×10^8 years (Lord et al. 1996). Maps of both molecular line emission and thermal dust continuum show a double-peaked structure in the central kiloparsec (Neininger et al. 1998; Hughes et al. 1994).

The CO J=6-5 line was first detected toward M82 by Harris et al. (1991), who showed that molecular gas in starburst galaxies is substantially warmer than in typical disk clouds. The CO J=6-5 transition probes higher excitation temperatures (116 K above the ground state) than the more accessible CO J=1-0 (5.5 K), CO J=2-1 (17 K), and CO J=3-2 (33 K) transitions. The higher J spectral lines thus provide important information needed to understand the large mass of T$\sim$100 K molecular gas that is heated by massive young stars in a starburst galaxy. Recent improvements in receiver technology now allow high quality maps to be made of the

^{12}CO J=6-5 and J=7-6 rotational lines in nearby galaxies. Mao et al. (2000) recently mapped the ^{12}CO J=7-6 line. I present here a map of ^{12}CO J=6-5.

As improving receiver technology provides astronomers with ever higher quality data, advances in digital computers open up possibilities for analyzing observations in new and better ways. For instance, CO excitation analyses in the large velocity gradient (LVG) approximation can now be calculated in a few milliseconds on a typical modern desktop computer. This allows us to evaluate multi-component models with many parameters, examining huge volumes of parameter space to find all combinations of the model parameters consistent with the measured data rather than only calculating some narrow range of possible solutions. Using measured line intensities, I have calculated likelihood density functions for each of the parameters of a two-component LVG model for the NE and SW CO emission peaks. I have also calculated likelihood functions for a variety of physical quantities derived from these parameters, such as the pressure and the beam-averaged column density. These likelihood curves were used to find median likelihood estimators and 95% confidence intervals for the quantities of interest.

I have also developed a novel deconvolution technique to compute line ratio maps when a high quality, high resolution map is available for the denominator and both maps are of the same species. This technique uses all spatial and velocity information in both maps, and can calculate the line ratio at a higher spatial resolution than the numerator map. With this technique, information is not thrown away as with the common method of integrating away the velocity information and smoothing the higher-resolution map before dividing.

6.2 Observations

All observations were performed at the Caltech Submillimeter Observatory (CSO) in 1998 January and 1999 January using SIS receivers operating in double-sideband mode. The ^{12}CO J=6-5 map was made in excellent weather ($\tau_{225\,\mathrm{GHz}} \lesssim 0.04$), with typical single-sideband system temperatures (including the atmosphere) around

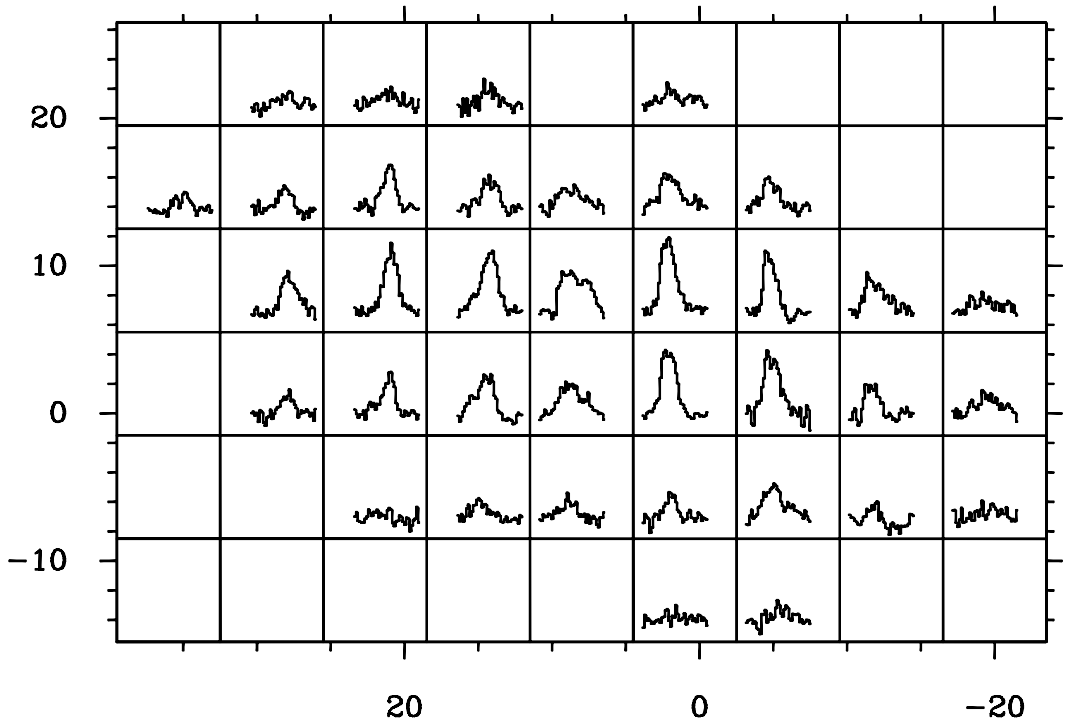

Figure 6.1 Spectra of ^{12}CO J=6-5 in M82. The map has been rotated such that the horizontal offsets are approximately along the major axis. Offsets are in seconds of arc from an arbitrary center. The vertical scale ranges from -1 to 4.5 K, and the horizontal scale ranges from -80 to 520 km s^{-1}.

3000 K. The receiver consisted of a quasi-optical SIS mixer with an integrated HEMT low-noise amplifier (LNA); an upgraded version of this receiver was described in Chapter 5. A pair of 1024 channel, 500 MHz acousto-optical spectrometers were used as backends. The chopping secondary was switched at a 1 Hz rate with a 60″ throw in azimuth. The telescope was calibrated at 691 GHz using observations and beam maps of Saturn. The beam FWHP was approximately 14″, and the main beam efficiency was 30%. The use of a broadband tunerless receiver effectively eliminates calibration errors associated with receiver sideband imbalance. The total calibration uncertainty is estimated to be 30%.

The map of M82 consists of 36 positions on 7.5″ centers, and covers 70″ along the major axis of the galaxy and 50″ along the minor axis (Figure 6.1). At a distance of 3.6 Mpc (Freedman et al. 1994), this corresponds to an area of 1200 pc × 880 pc mapped with a 250 pc FWHP beam. The coordinates of the J=6-5 map were corrected

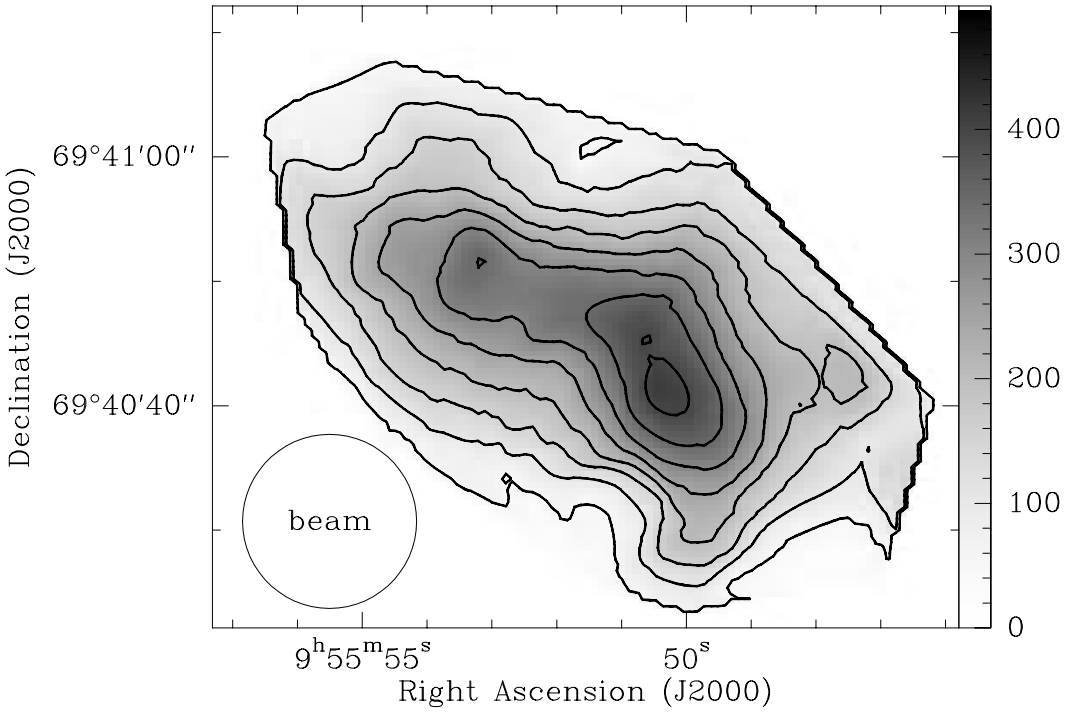

Figure 6.2 Integrated intensity of ^{12}CO J=6-5 in M82. Contours are 50, 100, 150, 200, 250, 300, 350, and 400 K km s^{-1}.

for systematic pointing offsets by comparing to ^{12}CO J=2-1 and C^{18}O J=1-0 Plateau de Bure Interferometer data cubes from Weiß et al. (2001), according to the following procedure. A line connecting the antenna temperature peaks of the bright hot spots on either side of the dynamical center was found. This line was then drawn on top of a contour map of line center velocity,

$$v_c = \frac{\int T_A \, v \, dv}{\int T_A \, dv} \, . \tag{6.1}$$

The contours of constant velocity crossed the line at nearly right angles. A reference point was chosen where the line connecting the hot spots crossed the 200 km s^{-1} velocity contour. The coordinates of the ^{12}CO J=6-5 map were then adjusted to match the reference point to the coordinates of a point found the same way in the interferometer maps. The correction was 4.5″ in right ascension and 7.2″ in declination. This large correction was expected because the telescope fixed pointing offsets were not determined prior to the observations. The uncertainty of the determined position

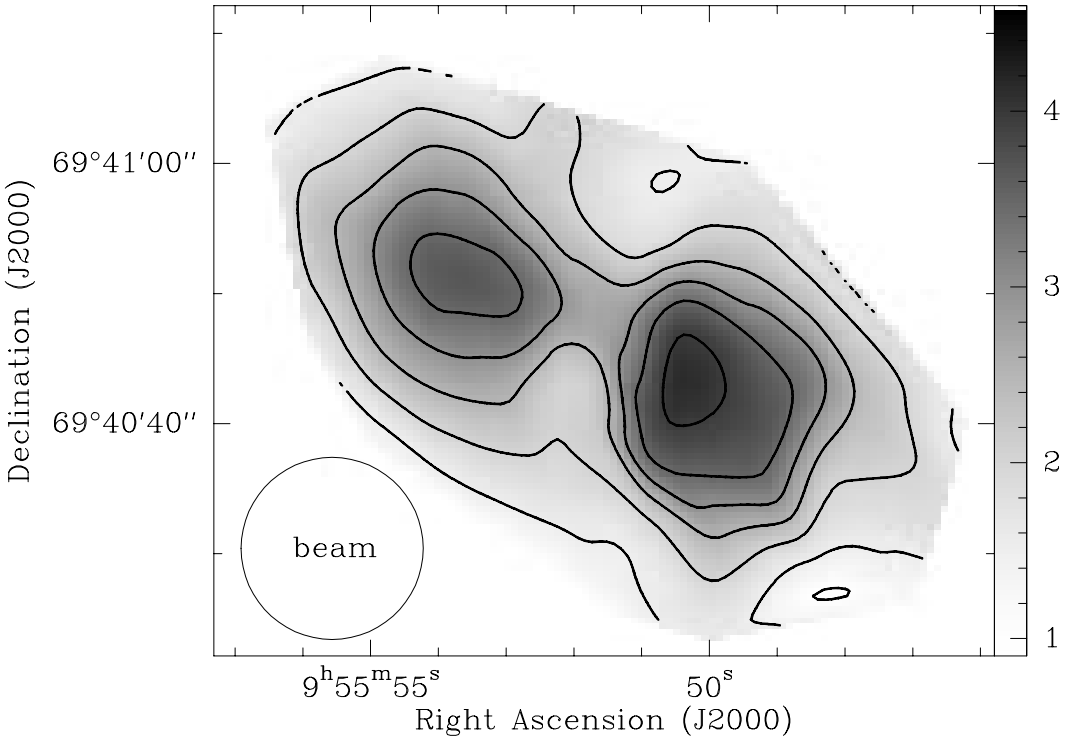

Figure 6.3 Peak antenna temperature of ^{12}CO J=6-5 in M82. Contours are 1.0, 1.5, 2.0, 2.5, 3.0, 3.5, and 4.0 K.

is about 2″ in each axis. Maps of integrated intensity and peak antenna temperature are shown in Figure 6.2 and Figure 6.3, respectively. A channel map is shown in Figure 6.4, and position-velocity plots are shown in Figure 6.5.

In addition to the ^{12}CO J=6-5 map, we have also observed 17 positions of the ^{12}CO J=4-3 line, 9 positions of ^{12}CO J=3-2, and 5 positions of ^{13}CO J=3-2, all with the CSO facility SIS receivers. Most of these positions were observed as cuts along the major axis of the galaxy. The beam sizes were 16.5″, 24.4″, and 25.5″ FWHP at 461, 346, and 331 GHz, respectively, with corresponding main beam efficiencies of 0.45, 0.50, and 0.50. The CO J=3-2 observations were made with a 4 GHz wideband analog correlator spectrometer (WASP) similar to that described by Harris and Zmuidzinas (2001). The ^{13}CO J=3-2 spectra were scaled up by 14% to account for the difference in atmospheric transmission in the two sidebands. The reduced, calibrated spectra are plotted in Appendix C. We also integrated on the ^{13}CO J=6-5 line for a single pointing in 1998 January and 1999 January for a total of 96 minutes under conditions

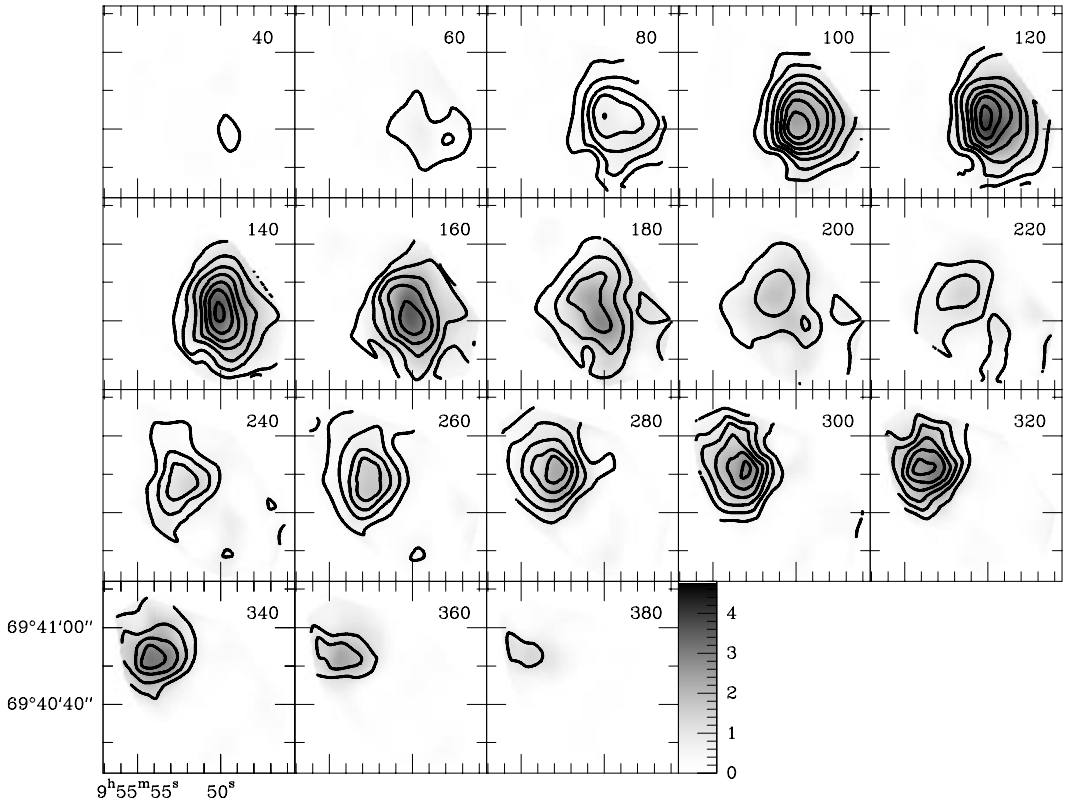

Figure 6.4 Channel maps of ^{12}CO J=6-5 in M82. Center velocities are given in the upper right corner of each box in km s^{-1}. Each image covers a velocity range of 20 km s^{-1}. Contours are 0.5, 1.0, 1.5, 2.0, 2.5, 3.0, 3.5, and 4.0 K.

similar to those for the ^{12}CO J=6-5 observations, but did not detect the line.

6.3 Results

Figure 6.2 shows two peaks in integrated intensity, the SW hot spot being stronger than the NE. Comparing the integrated intensity to Figure 6.3, we see that the two hot spots are much more distinct in peak antenna temperature than in integrated intensity. This is due in part to a spatial smearing effect caused by the antenna beam width being comparable to the spacing between the hot spots, i.e., a 14″ FWHP beam compared to 19″ peak separation in Figure 6.3. The locations of the hot spots in the peak antenna temperature plot are less affected by smearing since the hot spots differ in center velocity by 200 km s^{-1}.

Figure 6.6 shows the ^{12}CO J=6-5 integrated intensity plotted over the ^{12}CO J=2-1

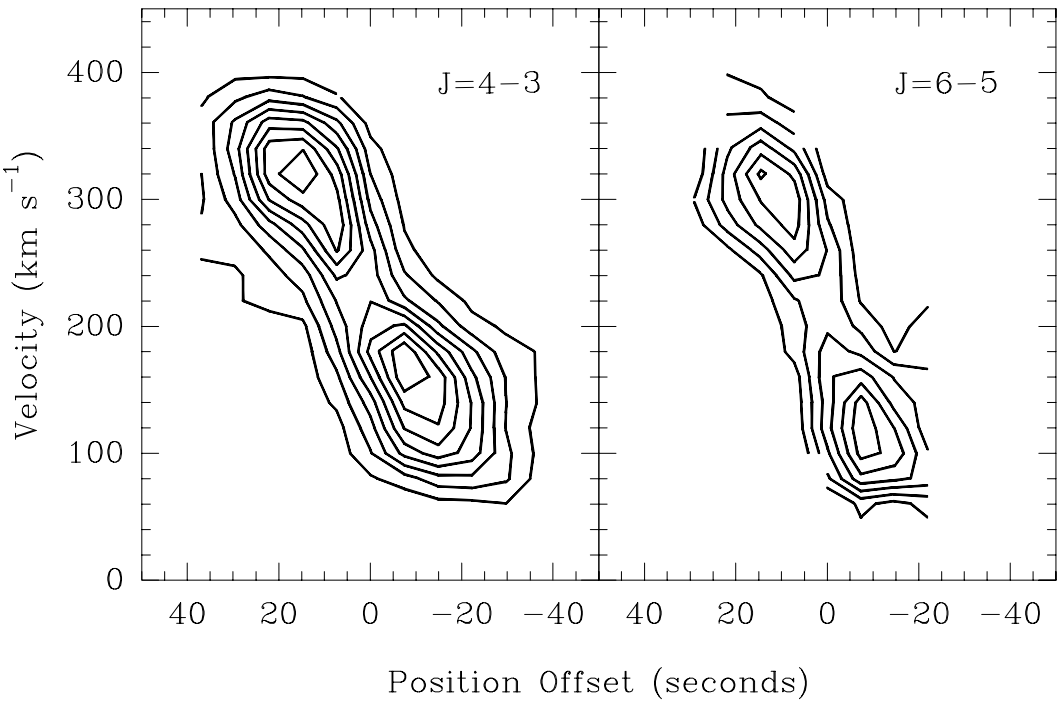

Figure 6.5 Position-velocity diagram along the major axis of M82 for ^{12}CO J=4-3 and ^{12}CO J=6-5. The SW hot spot peaks at different velocities in the two transitions, and the overall velocity gradient is steeper in CO J=6-5. Note that the broad, lower-intensity spectrum between the two hot spots explains the difference in integrated intensity and peak temperature maps. The positions are offset from arbitrary centers along the major axis of the galaxy. Contours are from 0.5 to 4 K in steps of 0.5 K.

map from Weiß et al. (2001). The hot spots in the CO J=6-5 map are closer together than in the lower J map. This is consistent with the finding of Mao et al. (2000) that the angular separation of the lobes is smaller for a "high CO excitation component" than is seen in the low-J CO lines. It can be seen in the figure that the J=6-5 SW hot spot is located between the lower J SW and center hot spots. This suggests that the SW hot spot of the J=6-5 map includes unresolved emission from both of these regions. The SW hot spot appears to be somewhat extended in the direction of the minor axis in the J=6-5 map. It is unlikely that this shape is real because it is not seen in any other published observations, including HCN J=1-0 (Brouillet and Schilke 1993) and CO J=7-6 (Mao et al. 2000) maps. It is also unlikely to be a calibration effect since the weather and receiver were very stable during the observations. It is possible that the telescope pointing drifted a few seconds of arc

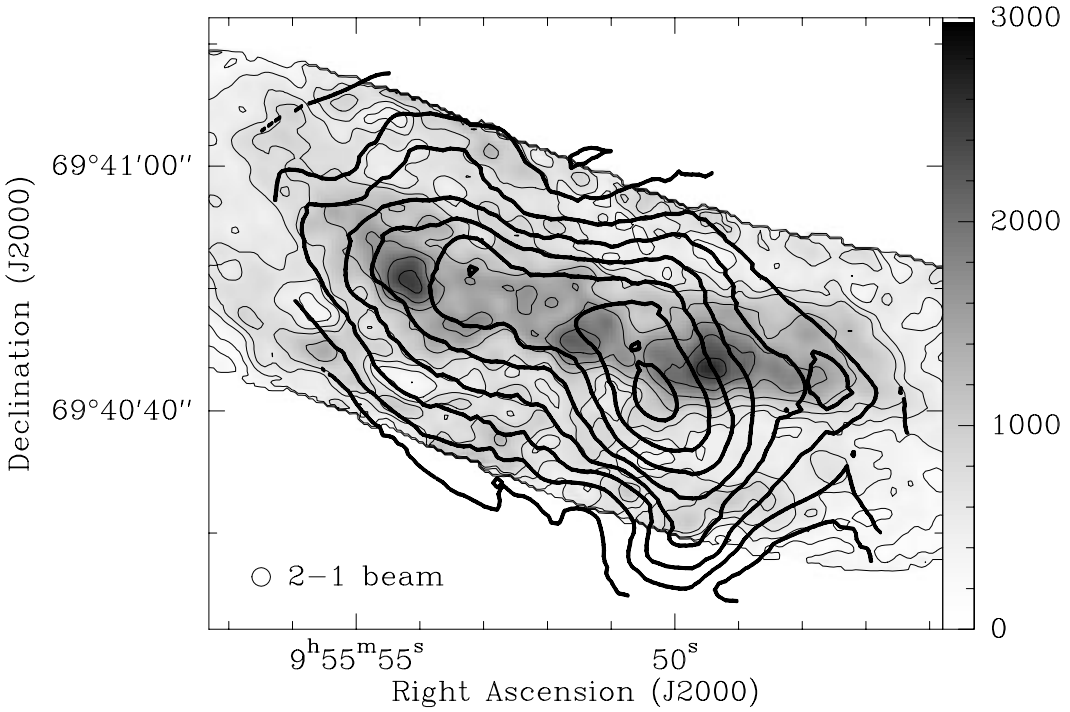

Figure 6.6 M82 ^{12}CO J=6-5 integrated intensity contours superimposed on ^{12}CO J=2-1 integrated intensity from Weiß et al. (2001). Contours are 50, 100, 150, 200, 250, 300, 350, and 400 K km s^{-1}.

during the observations, causing this artifact.

The total luminosity of the ^{12}CO J=6-5 line was found to be 9.0×10^5 L$_\odot$. This was calculated from the spatially and spectrally integrated intensity of 2.8×10^5 K km s^{-1} arcsec^2 after zeroth-order baseline subtraction, assuming spherically-symmetric emission and a distance of 3.6 Mpc.

The ^{13}CO J=6-5 line was not detected after 96 minutes of integration time near the central pointing. The $3\,\sigma$ upper limit of the integrated intensity for a 14″ beam calculated from the RMS channel noise is 7.9 K km s^{-1}. A reliable upper limit may be somewhat larger, however, since uncertainties in zeroth-order baseline subtraction and a small amount of baseline ripple could dominate over the channel noise. Nonetheless, with an implied J=6-5 antenna temperature ratio of I(^{12}CO)/I(^{13}CO)$\gtrsim$ 40, it is clear that ^{13}CO J=6-5 is very weak.

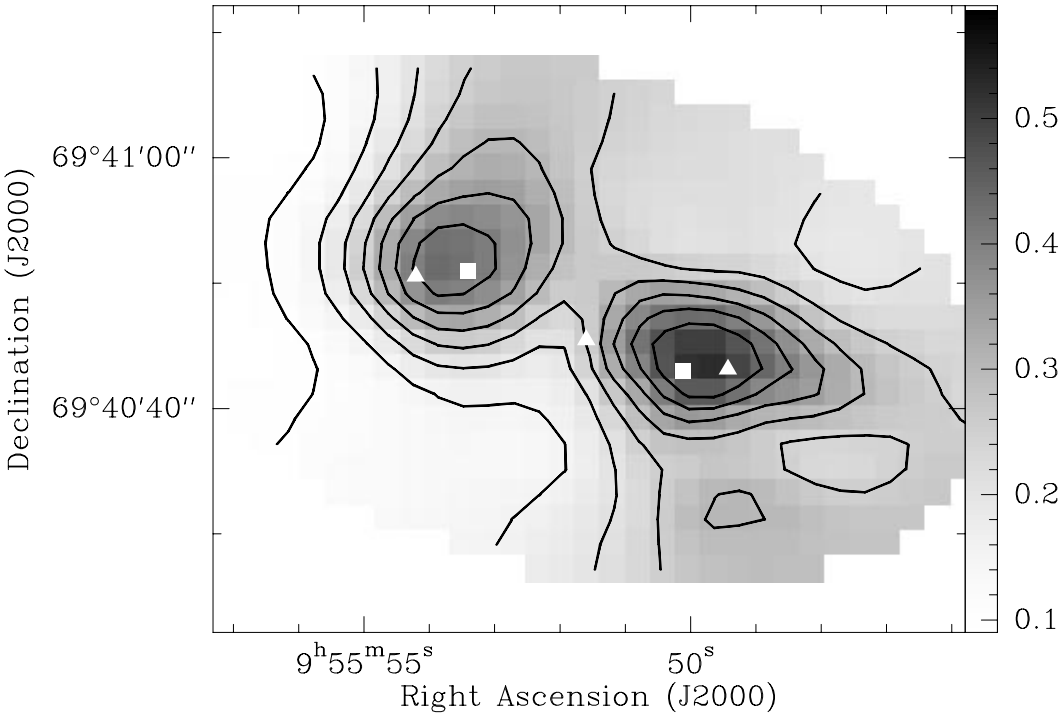

Figure 6.7 Deconvolved ^{12}CO J=6-5 / ^{12}CO J=2-1 brightness temperature ratio map. Contours are from 0.1 to 0.45 by 0.05. The squares indicate the locations of the J=6-5 intensity peaks, and the triangles the locations of the J=2-1 integrated intensity peaks.

6.3.1 A ^{12}CO J=6-5 / ^{12}CO J=2-1 Line Ratio Map

Figure 6.7 shows a map of the ^{12}CO J=6-5 / ^{12}CO J=2-1 line ratio. The J=2-1 data used to calculate the ratio were observed with the Plateau de Bure Interferometer and include short-spacing corrections based on observations with the IRAM 30 m telescope (Weiß et al. 2001). The ratio map was calculated using a novel deconvolution technique that takes advantage of velocity information in the J=6-5 map along with the high spatial resolution of the J=2-1 map to improve the resolution and accuracy of the ratio map. A Lagrange multiplier was used to set the relative weighting between minimizing the resulting χ^2 and maximizing the smoothness of the resulting ratio map. Details of the calculation are given in Appendix D. It is immediately apparent that the brightness temperature ratio is highest at the two integrated intensity peaks, reaching 0.4 and 0.5 in the NE and SW peaks, respectively, and is typically 0.2 elsewhere in the nuclear region.

6.3.2 Comparison to the Galactic Center

It is informative to compare the nuclear region of M82 to the Galactic center. Both are seen nearly edge-on. The hot spots of M82 are each about 180 pc across, corresponding to 1.2° at the Galactic center. With the exception of the circumnuclear disk (CND), the dust temperature over large scales in the Galactic center is a fairly uniform 21 K (Pierce-Price et al. 2000), compared to 48 K in the nuclear regions of M82 (Colbert et al. 1999; Hughes et al. 1994). Although the molecular mass of the two regions is about the same, the IR luminosity of M82 is about 50 times larger than in the Galactic center (Colbert et al. 1999; Nishimura et al. 1980). The star formation rate in the central 500 pc of the Galaxy is about 0.3 to 0.6 $M_\odot$ yr^{-1} (Güsten 1989) compared to about 6.6 $M_\odot$ yr^{-1} in the central region of M82 calculated from the IR luminosity based on a conversion factor for starburst galaxies from Kennicutt (1998). A summary comparison is presented in Table 6.1.

Galactic carbon monoxide emission up to J=8-7 was measured with the COBE Far Infrared Absolute Spectrophotometer (FIRAS). The J=6-5/J=2-1 antenna temperature ratio in the central $5° \times 1°$ calculated from measurements reported by Fixsen et al. (1999) is 0.067 ± 0.010. Comparing this value to Figure 6.7, we see that the J=6-5/J=2-1 line ratio is at least 5 times larger in the SW hot spot of M82 than in the Galactic center. It is clear that the proportion of molecular gas that is warm is significantly larger in the nuclear region of M82 than in the Galactic center.

6.3.3 LVG Analysis

Table 6.2 lists the inputs used in an excitation analysis of the two hot spots in M82. The analysis was performed using the LVG photon escape probability function $\beta = (1 - e^{-3\tau})/3\tau$ derived for plane-parallel clouds by Scoville and Solomon (1974). Results calculated with the escape probability function for spherical clouds in gravitational collapse $\beta = (1 - e^{-\tau})/\tau$ (Goldreich and Kwan 1974) differ in detail but do not change the general conclusions derived from this analysis. Collision rate constants for excitation of CO by para H_2 up to J=14 were taken from Flower (2001) and scaled

Table 6.1 Comparison to the Galactic Center

Quantity	Units	Galactic Center	M82 Nucleus
Diameter	pc	600	1,000
L_{IR}	$L_\odot$	8×10^8 [a]	3.8×10^{10} [b]
M_{mol}	$M_\odot$	$10^{7.9}$ [c]	2×10^8 [d]
L_{IR} / M_{mol}	$L_\odot\ M_\odot^{-1}$	10	200
SFR	$M_\odot\ yr^{-1}$	0.3 – 0.6 [c]	6.6 [e]
T_{dust}	K	21 [f]	48 [b]
CO $\frac{T_A\ J=6-5}{T_A\ J=2-1}$	...	0.067 [g]	0.2 – 0.5

[a] From Nishimura et al. (1980).

[b] From Colbert et al. (1999).

[c] From Güsten (1989).

[d] See, for example, Carlstrom (1988), Wild et al. (1992), Mao et al. (2000), Weiß et al. (2001), this work.

[e] Calculated from L_{IR} based on a conversion factor for starburst galaxies from Kennicutt (1998).

[f] From Pierce-Price et al. (2000).

[g] Calculated from COBE FIRAS measurements reported by Fixsen et al. (1999).

up by 21% to account for excitation by He. Cool gas (approximately 10 K) such as that found in cosmic ray-heated cloud cores gives rise to substantial emission in the millimeter CO lines but does not have sufficient thermal energy to populate higher states such as J=6. On the other hand, warm gas such as the few hundred K gas found in photodissociation regions (PDRs) near massive young stars will emit much more power in J=6-5 than in J=2-1 or J=1-0 (Harris et al. 1987; Kaufman et al. 1999). Thus, I use a two-component model to explain the observed CO flux up to J=7-6. In reality, we expect a continuum of temperatures and densities, but with the limited number of measurements available, a two-component model is a reasonable approximation.

The LVG model for each component takes three parameters: kinetic temperature, H_2 density, and CO column density per unit velocity. The LVG models for the two components are calculated independently, and the line intensities are summed using separate area filling factors for the two components. Calling the area filling factor Φ, H_2 density n, and CO column density N,

$$T_{model} \; = \; \Phi_w \; \times \; f(T_w, n_w, N_w/\Delta v) \; + \; \Phi_c \; \times \; f(T_c, n_c, N_c/\Delta v) \; , \qquad (6.2)$$

where the subscripts w and c represent the warm and cool components, respectively. If the clouds do not fill the beam, then $\Phi < 1$ and N is the cloud column density. In this case, the beam-averaged column density is $\Phi \times N$. The beam-averaged column density is used to calculate the total molecular mass in the beam. If the clouds fill the beam, then $\Phi = 1$ and N is the beam-averaged column density rather than the cloud column density. [Note that solutions with $\Phi > 1$, which would correspond to more than one cloud along the line of sight, imply higher optical depths and so mathematically are treated as unit area filling factors with higher column densities since the intensities no longer add linearly.]

Table 6.2 Measured M82 Line Strengths

	NE Lobe (9, 4) [a]		SW Lobe (-9, -4)		
Transition	I (K km s^{-1})	T (K)	I (K km s^{-1})	T (K)	σ [b]
^{12}CO J=1-0 [c]	529	2.94	620	3.88	7%
^{12}CO J=2-1 [d]	748	4.16	751	4.69	7%
^{12}CO J=3-2	523	2.91	476	2.97	8%
^{12}CO J=4-3	427	2.37	332	2.08	10%
^{12}CO J=6-5	179	0.99	224	1.40	12%
^{12}CO J=7-6 [c]	122	0.68	154	0.96	12%
^{13}CO J=1-0 [c]	37.0	0.205	54.2	0.339	8%
^{13}CO J=2-1 [c,e]	54.3	0.302	63.6	0.398	12%
^{13}CO J=3-2 [f,g]	24.9	0.138	26.0	0.163	50%
^{13}CO J=6-5 [h]	< 4.7	< 0.026	< 4.7	< 0.029	30 mK

Note. — Values correspond to a FWHP beam of 24.4″. Intensities were integrated from 25 to 395 km s^{-1}. Temperatures are averages computed as I/Δv, where $\Delta v = 180$ km s^{-1} for the NE position and $\Delta v = 160$ km s^{-1} at the SW position. These widths were chosen so that the temperatures would be representative of the average temperatures in the primary components of the lines. In all cases except ^{13}CO J=6-5, the statistical error in integrated intensity due to channel noise is much smaller than calibration uncertainties.

[a] Offsets in arc seconds are based on a reference point halfway between the J=6-5 antenna temperature peaks, corresponding to RA 09^{h}55^{m}51.8^{s} Dec 69°40′47″ J2000. The NE and SW positions are at the J=6-5 peaks, but are inside of the low J peaks.

[b] Values are estimates based on a combination of factors, including effects related to calibration and smoothing. The real uncertainty is generally much larger than estimates based solely on the RMS channel noise. These values of σ were used as inputs of the LVG modeling in Section 6.3.3.

[c] Estimated by scaling integrated intensities published by Mao et al. (2000) based on their observations with the IRAM 30 meter telescope and the HHT by 0.92 to account for our broader beam.

[d] Calculated from Plateau de Bure Interferometer data provided by Weiß et al. (2001).

[e] Mao et al. warn that due to the limited extent of their ^{13}CO J=2-1 map, their values should be considered with caution.

[f] Values for a 24.4″ FWHP beam were approximated by scaling observations made with a 25.5″ beam up by 3.6%.

[g] The integrated intensities for ^{13}CO J=3-2 presented here are much lower than those published elsewhere. Due to the wide range of measured values, the antenna temperatures used for LVG models in Section 6.3.3 were 50% larger than the values in this table. The large value of σ reflects this uncertainty. More observations of this line are needed.

[h] Line was not detected after 96 minutes of integration time near the central pointing. Values correspond to 3 σ limits found by scaling σ for a 14″ beam calculated from the RMS channel noise by a factor of 0.59 to approximate a 24.4″ beam. The large 1σ value in the right-hand column reflects concerns that uncertainties involving zeroth-order baseline subtraction and a small amount of baseline ripple could dominate over the channel noise.

Calculating Likelihood Distributions

The two-component LVG model has nine free parameters: the H_2 kinetic temperatures T_{kin}, number densities $n(H_2)$, column densities N(CO), and area filling factor Φ_A for the warm and cool components, plus the $^{12}CO/^{13}CO$ column density ratio. I determine these parameters from the ten measured spectra. A single precise solution for the model would be unrealistic since the number of free parameters is comparable to the number of measured lines, the data have significant uncertainties, and the model is a simplification of the real physical conditions in the source. It should also be noted that while some quantities physically have unique, well-defined values such as the beam-averaged column density, others do not, e.g., the kinetic temperature of the gas.

In our analysis, we assume that the measured line strengths, represented by the vector $\mathbf{M}$, have Gaussian-distributed random errors of known sigma. The model parameters are collected into a vector $\mathbf{a}$, and the set of calculated antenna temperatures is denoted by $\mathbf{T}(\mathbf{a})$. If we knew the true values of the model parameters, ignoring that the model itself only approximates the true physical conditions, then the probability density for measuring a given set of line intensities $\mathbf{M}$ is given by

$$P(\mathbf{M}\,|\,\mathbf{a},\boldsymbol{\sigma}) = \prod_{i=1}^{10} \frac{1}{\sqrt{2\pi}\sigma_i} \exp\left[-\frac{1}{2}\left(\frac{M_i - T_i(\mathbf{a})}{\sigma_i}\right)^2\right] . \tag{6.3}$$

Bayes' Theorem allows us to use this probability density to compute the likelihood of a particular set of parameters $\mathbf{a}$ given a set of measurements $\mathbf{M}$. In addition, it allows other information about the parameters $\mathbf{a}$ to be included in the calculation through the prior likelihood function $P(\mathbf{a})$:

$$P(\mathbf{a}\,|\,\mathbf{M},\boldsymbol{\sigma}) = \frac{P(\mathbf{a}) \times P(\mathbf{M}\,|\,\mathbf{a},\boldsymbol{\sigma})}{\int d\mathbf{a}\, P(\mathbf{a}) \times P(\mathbf{M}\,|\,\mathbf{a},\boldsymbol{\sigma})} . \tag{6.4}$$

We can integrate to compute the likelihood distribution of any one parameter:

$$P_{ai}(x) = \int d\mathbf{a}\, P(\mathbf{a} \,|\, \mathbf{M}, \boldsymbol{\sigma})\, \delta(a_i - x)\ . \tag{6.5}$$

We can also compute likelihood density curves for functions of the parameters, such as pressure and beam-averaged column density. The likelihood distribution of some function $x = f(\mathbf{a})$ is given by

$$P_f(x) = \int d\mathbf{a}\, P(\mathbf{a} \,|\, \mathbf{M}, \boldsymbol{\sigma})\, \delta(f(\mathbf{a}) - x)\ . \tag{6.6}$$

The main difficulty with this approach (and possible source of controversy) is the choice of the prior probability density function $P(\mathbf{a})$. In particular, one must choose $P(\mathbf{a})$ even if one has no prior knowledge of the parameters $\mathbf{a}$. Bayes' Postulate tells us to set $P(\mathbf{a}) = 1$ for this case, since all values of $\mathbf{a}$ are *a priori* equally likely. It should be noted, however, that even this choice introduces a bias since choosing a different set of parameters $\mathbf{a}$ changes $P(\mathbf{a})$. For example, using Bayes' Postulate with the column density as a parameter would result in a different prior probability density $P(\mathbf{a})$ than using the logarithm of the column density as the parameter.

The likelihood distributions are computed numerically by creating an array of bins initialized to zero for each of the physical quantities of interest. The integrands of equations 6.5 and 6.6 are calculated inside a nested loop over all parameters $\mathbf{a}$, and at each iteration are added to the appropriate bins of the arrays. The resulting arrays are then scaled by functions of the loop step sizes and bin widths for normalization.

Constraints on Model Parameters

I first ran a calculation with a single component model, where the prior probability density function $P(\mathbf{a})$ was determined by the assumption that all values of the logarithms of the parameters are equally likely. Although the resulting likelihood curves for the parameters were reasonable, the fit to the measured data was poor. A two-component model was then calculated over a coarse grid to estimate the cool

component kinetic temperature. The cool component kinetic temperature was fixed at 14 K based on this result to speed up subsequent calculations. Since accurate collisional excitation rates were only available for temperatures up to 400 K, $P(\mathbf{a})$ was assumed to equal zero if $T_{kin} > 400$ K. Since I had already found that a single component model was a poor fit, I also set $P(\mathbf{a})$ to zero for models where the cool component accounted for less than 20% of the J=2-1 intensity. In all cases, area filling factors were not allowed to be greater than unity, since larger area filling factors imply higher optical depths and so mathematically must be treated as unit area filling factors with higher column densities. The H_2 densities were limited to the range of 10^2 to 10^6 cm^{-3}.

Two unphysical situations were rejected through the use of $P(\mathbf{a})$. First, the total molecular mass was not allowed to be larger than the dynamical mass. Secondly, models with impossibly large column lengths were rejected. These restrictions eliminated models with very large column density and low volume density. Both restrictions require knowledge of the $^{12}CO/H_2$ abundance ratio. Frerking et al. (1982) measured a ratio of 8.5×10^{-5} based on observations of clouds in Taurus and ρ Ophiuchi. The ratio may be higher in warm, star-forming clouds; Lacy et al. (1994) measured a ratio of 2.7×10^{-4} in NGC 2024. Since the uncertainty of these measurements is large, and the average value in M82 may be substantially different than in local clouds, I conservatively assume that

$$^{12}CO/H_2 \; < \; X_{max} = 5 \times 10^{-4} \; . \tag{6.7}$$

The outer edges of the 24.4″ FWHP beams are about 390 pc from the dynamical center of M82. Since each beam is mostly on one side of the dynamical center, and the beam covers most of the molecular material on that half of the galaxy, I exclude solutions where the mass in the beam is larger than one half of the dynamical mass. Thus, I require

$$\Phi_w N_w \; + \; \Phi_c N_c \; < \; \frac{1}{2} \frac{M_{dyn}}{m_{H2}} \; \frac{X_{max}}{A_{beam}} \; , \tag{6.8}$$

where the subscripts w and c indicate the warm and cool components, respectively, and m_{H2} is the mass of a single H_2 molecule. I take the area of the beam to be 145,000 pc^2, and, based on a rotational velocity of 135 km s^{-1} at a radius of 390 pc, I take the dynamical mass to be $1.7 \times 10^9\, M_\odot$.

Solutions for which the length of the column is larger than the entire molecular region can clearly be excluded. If the area filling factor Φ_A is less than unity, then the maximum possible column length is smaller still. Based on simple geometrical arguments, and given that the bright part of the molecular region is about 900 pc across, I require that

$$\frac{N(CO)}{n(H_2)}\, X_{max} \;<\; \sqrt{\Phi_A} \times 900\; pc. \tag{6.9}$$

Resulting Likelihood Distributions and Confidence Intervals

Using a prior likelihood function $P(\mathbf{a}) = 0$ for the rejected regions of parameter space discussed above, and assuming that all values of the logarithms of the parameters are equally likely everywhere else, I calculated likelihood curves for all eight free parameters as well as nine derived quantities. The best-fit χ^2s of 1.9 and 1.8 for the NE and SW positions, respectively, each based on ten measurements and eight free parameters, indicate that both the model and my choices of σ are reasonable. Likelihood curves of the free parameters are shown in Figure 6.8; the curves for derived quantities are shown in Figure 6.9. Median likelihood estimators and 95% confidence intervals are listed in Table 6.3. Note that since the values in the table were calculated from integrals over all possible solutions, the listed median values do not necessarily represent a single self-consistent solution. Example solutions are shown in Figure 6.10.

Comparison with a Spherical-Cloud Model

Likelihood curves were also calculated using an escape probability function derived for spherical clouds in gravitational collapse (Goldreich and Kwan 1974). The results from the two different cloud models differ in detail but do not change the basic

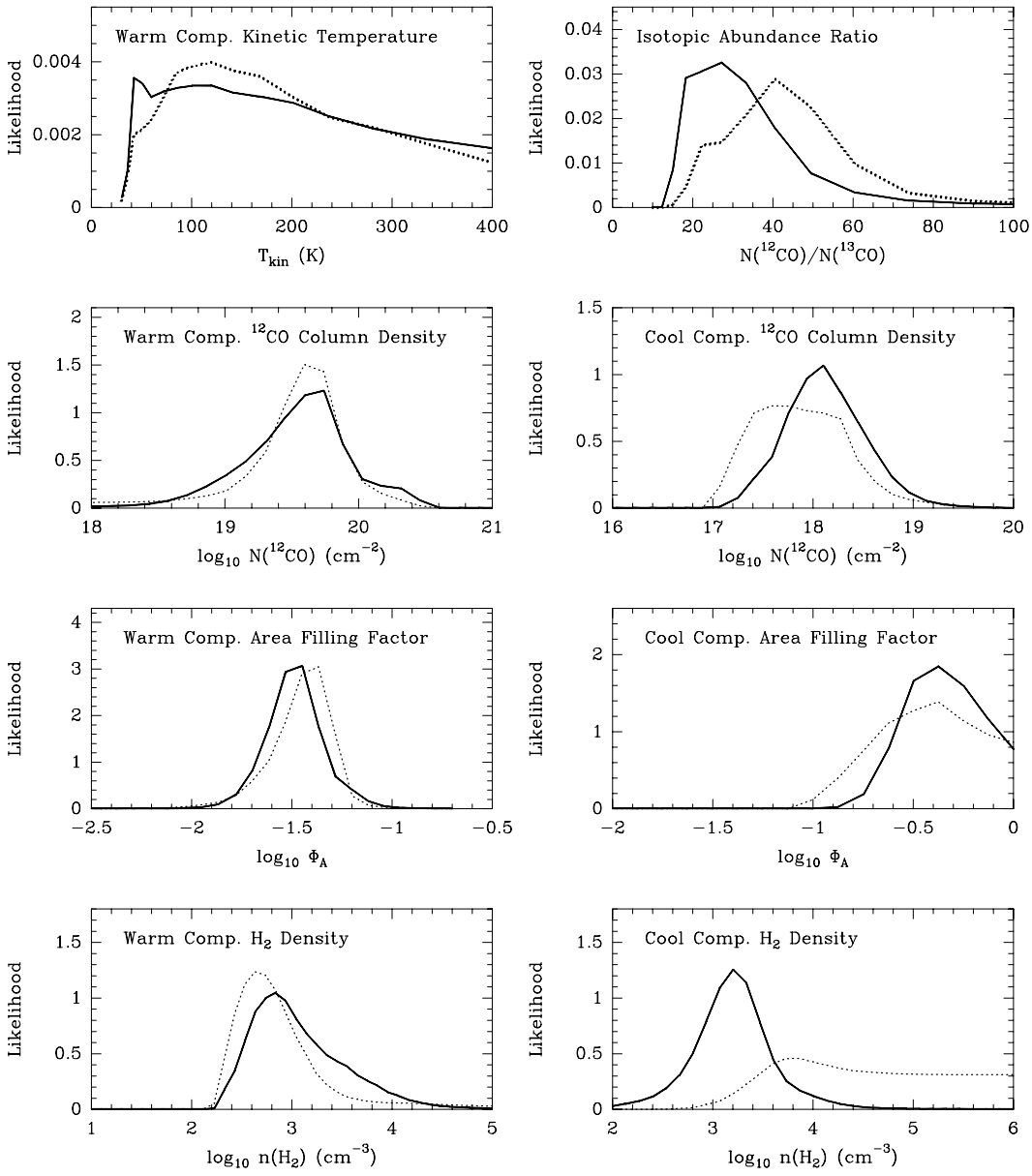

Figure 6.8 Likelihood curves of the LVG model parameters. The solid curves are for the SW lobe, and the dotted curves the NE lobe. The cool component temperature was fixed at 14 K. Note that all parameters are constrained except the cool component density of the NE lobe and the warm component temperature.

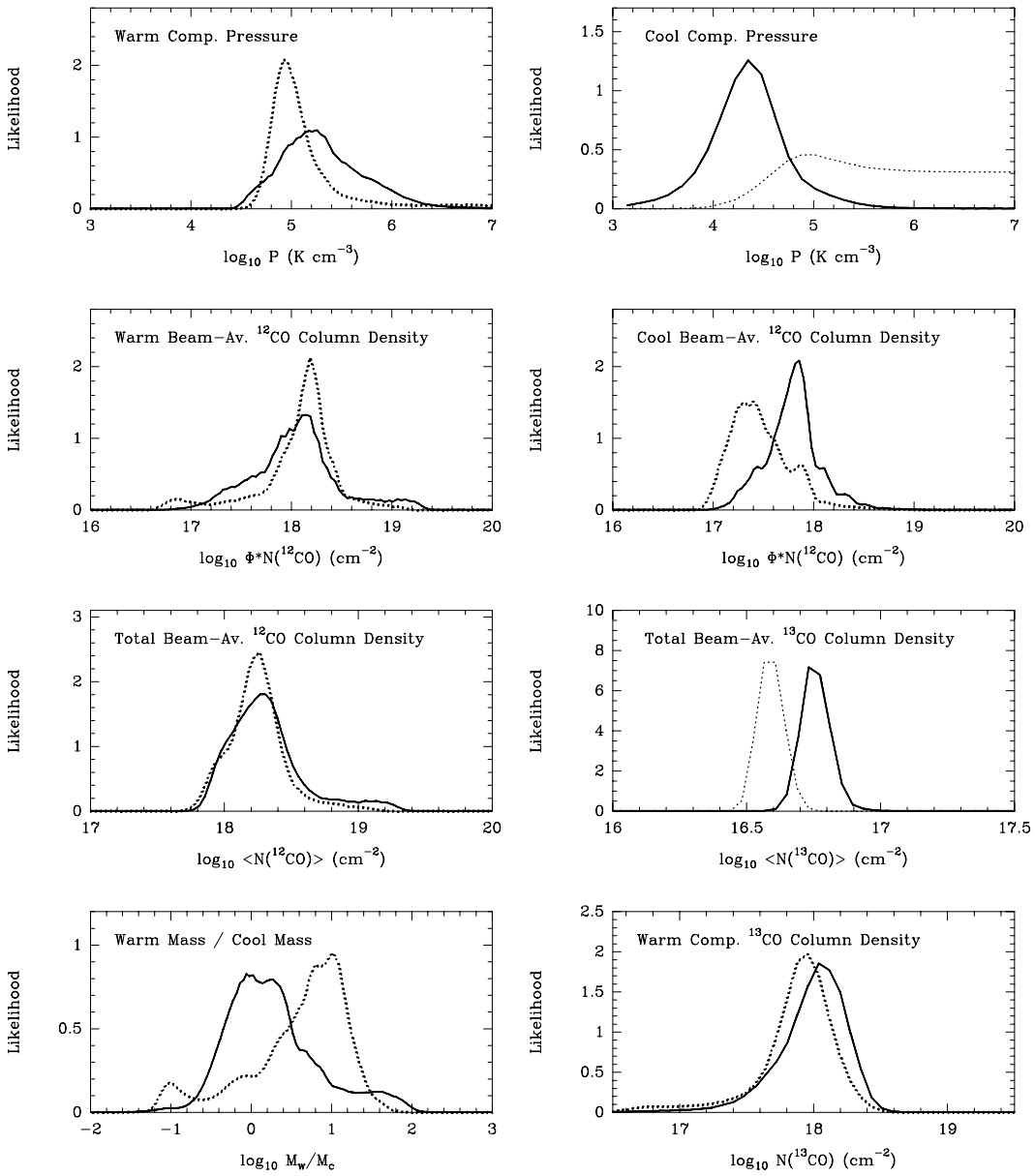

Figure 6.9 Likelihood curves for quantities derived from the LVG model parameters. The solid curves are for the SW lobe, and the dotted curves the NE lobe. The total average column density is the sum of the warm and cool component beam-averaged column densities.

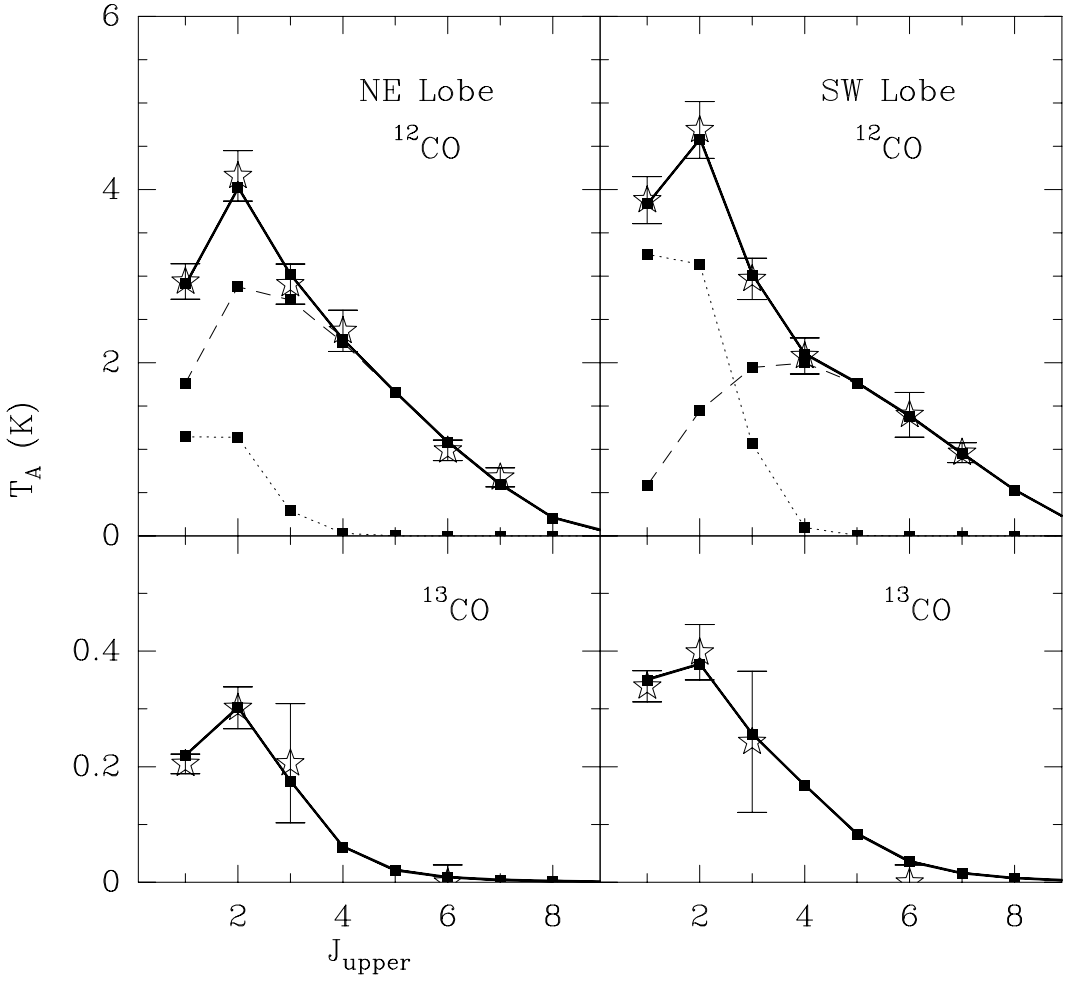

Figure 6.10 Measured temperatures with example LVG solutions for the two main hot spots in M82. Measured values (indicated with stars) and $1\,\sigma$ error bars are taken from Table 6.2, except for ^{13}CO J=3-2, which was scaled up by 50% as explained in the table notes. The cool and warm components are shown with dotted and dashed lines, respectively, and total temperatures with a solid line. The solution for the NE lobe is an example solution with low warm component H_2 density, in this case, $10^{2.6}$ cm^{-3}. For this solution, the pressures of the two components are both around 10^5 K cm^{-3}, and the warm component cloud sizes are large, $\sim$200 pc. The SW lobe example, on the other hand, has a warm component H_2 density of $10^{3.3}$ cm^{-3} and cloud size around 20 pc.

results of this paper; I will therefore summarize the differences rather than present figures and tables of the spherical model results. The most significant difference is that the spherical cloud model predicts higher volume densities than the plane-parallel model by a factor of $\sim$5. Column densities are a factor of $\sim$2 larger. The kinetic temperatures are better constrained with the spherical model, with slightly lower median likelihood values. The isotopomer ratio, on the other hand, is less well constrained and a factor of $\sim$2 higher.

A particularly interesting difference is the ratio of warm gas mass to cool gas mass. We would expect this ratio to be higher in the SW lobe than the NE, since the SW lobe is brighter in most tracers of warm gas and dust, such as 12.4 μm continuum (Telesco and Gezari 1992) and CO J=6-5. The likelihood distributions calculated with the plane-parallel model in Figure 6.9 are somewhat anomalous, since they suggest that the proportion of warm gas is higher in the NE lobe than the SW. The spherical model predicts a lower cool gas mass for the SW lobe than the plane-parallel model, and leaves the cool gas mass of the NE lobe essentially unchanged. This in turn causes the predicted ratio of warm gas mass to cool gas mass to be higher in the SW lobe than the NE lobe, which is more consistent with our expectations.

Not all of the determined quantities changed with the choice of escape probability function. In particular, the total beam-averaged ^{13}CO column density determinations are almost exactly the same with both spherical and plane-parallel cloud models.

Discussion

We see from Table 6.3 that the ^{13}CO beam-averaged column density is the most precisely determined result. This parameter is well determined not only because the ^{13}CO optical depths are lower than those of ^{12}CO, but also because the ^{12}CO measurements help constrain other physical conditions, i.e., the temperatures, densities, and filling factors. It is interesting to note that total beam-averaged column densities, which physically have unique, well-defined values, are generally more tightly constrained by the data than cloud column densities, which would be expected to cover ranges of values due to the presence of many different clouds in a single beam.

After the ^{13}CO beam-averaged column density, the area filling factors and the isotopomer abundance ratio were the next most precisely determined parameters. The data only allow a lower limit to be set on the cool component H_2 density and pressure in the NE lobe. This is primarily because the level populations become thermalized in cool, dense clouds and thus are nearly independent of H_2 density. The density of the warm component is easier to constrain, since the populations of the higher-J levels do not become thermalized until $n \sim 10^5$ cm^{-3}. Determinations of kinetic temperatures are biased by the nature of the two-component model. For example, the very small likelihood that the warm component is ∼30 K does not mean that there is no molecular gas at 30 K in the source; rather, it means that the two-component model cannot match the measured line strengths if it assumes that all the gas in the warm component is at ∼30 K. Although the model was restricted to kinetic temperatures below 400 K for purely practical reasons, it is likely that energy balance considerations would require a similar upper limit.

Figures 6.8 and 6.9 indicate that conditions in the two hot spots are very similar. These results suggest that the SW lobe has higher beam-averaged ^{13}CO column density and lower cool component H_2 density. The temperatures and filling factors are about the same. In both hot spots, the H_2 density is lower for the warm component than the cool. Median likelihood estimates for pressure range from $10^{4.4}$ to $10^{5.2}$ K cm^{-3}.

It is interesting to note that the median likelihood estimates of the isotopomer abundance ratio ^{12}CO/^{13}CO of 40 and 30 in the NE and SW lobes, respectively, (Table 6.3) lie between the value of 25 for Galactic center clouds determined by Güsten (1989) and values ranging from 50 to 100 for M82 determined by Mao et al. (2000) and Weiß et al. (2001).

Table 6.4 shows typical ^{12}CO optical depths calculated from median values listed in Table 6.3. The warm clouds are optically thick in all transitions except J=1-0. The cool component optical depths are of order unity for low-J transitions.

The example fits in Figure 6.10 show that it is necessary to understand the warm molecular component even to understand low-J CO spectra. This is because the warm

Table 6.3 M82 LVG Model Results

		NE Lobe		SW Lobe	
Quantity	Units	Range [a]	Median [b]	Range	Median
$\frac{N(^{12}CO)}{N(^{13}CO)}$		20-140	40	15-200	30
$<N(CO)>$ [c]	cm^{-2}	$10^{17.9}$-$10^{18.8}$	$10^{18.2}$	$10^{17.9}$-$10^{19.1}$	$10^{18.2}$
$<N(^{13}CO)>$ [c]	cm^{-2}	$10^{16.48}$-$10^{16.67}$	$10^{16.57}$	$10^{16.63}$-$10^{16.85}$	$10^{16.73}$
M_w/M_c [d]		0.09-26	5	0.24-50	1.5
Warm Component					
T_{kin} [e]	K	> 50	170	> 50	170
$n(H_2)$	cm^{-3}	$10^{2.4}$-$10^{5.0}$	$10^{2.8}$	$10^{2.4}$-$10^{4.3}$	$10^{3.0}$
N(CO)	cm^{-2}	$10^{18.3}$-$10^{20.1}$	$10^{19.5}$	$10^{18.6}$-$10^{20.2}$	$10^{19.5}$
$N(^{13}CO)$	cm^{-2}	$10^{16.9}$-$10^{18.2}$	$10^{17.9}$	$10^{17.3}$-$10^{18.3}$	$10^{18.0}$
Φ_A [f]		0.013-0.06	0.03	0.015-0.06	0.03
$\Phi_A \times$ N(CO) [g]	cm^{-2}	$10^{16.9}$-$10^{18.7}$	$10^{18.1}$	$10^{17.2}$-$10^{19.1}$	$10^{18.0}$
$T_{kin} \times n(H_2)$ [h]	K cm^{-3}	$10^{4.7}$-$10^{7.0}$	$10^{5.0}$	$10^{4.6}$-$10^{6.2}$	$10^{5.2}$
Cool Component					
T_{kin}	K	...	14	...	14
$n(H_2)$	cm^{-3}	$> 10^{3.3}$	$10^{3.8}$	$10^{2.5}$-$10^{4.2}$	$10^{3.3}$
N(CO)	cm^{-2}	$10^{17.1}$-$10^{18.8}$	$10^{17.8}$	$10^{17.3}$-$10^{18.9}$	$10^{18.0}$
$N(^{13}CO)$	cm^{-2}	$10^{15.2}$-$10^{17.0}$	$10^{16.2}$	$10^{15.2}$-$10^{17.1}$	$10^{16.7}$
Φ_A [f]		0.12-1	0.34	0.2-1	0.4
$\Phi_A \times$ N(CO) [g]	cm^{-2}	$10^{17.0}$-$10^{18.1}$	$10^{17.4}$	$10^{17.2}$-$10^{18.3}$	$10^{17.8}$
$T_{kin} \times n(H_2)$ [h]	K cm^{-3}	$> 10^{4.4}$	$10^{4.9}$	$10^{3.6}$-$10^{5.3}$	$10^{4.4}$

Note. — Model is constrained with eight free parameters fit to the ten measured line temperatures listed in Table 6.2. The parameters are T_{kin}, $n(H_2)$, N(CO), and Φ_A for the warm and cool components, plus the $N(^{12}CO)/N(^{13}CO)$ ratio. The cool component temperature was fixed at 14 K. Assumed velocity widths are 180 km s^{-1} for the NE position and 160 km s^{-1} for the SW position.

[a] Ranges are for 95% confidence intervals.

[b] Median likelihood values do not represent a single self-consistent solution. See Section 6.3.3 for an explanation of how they were calculated.

[c] Beam-averaged column density including both warm and cool components.

[d] Warm gas to cool gas mass ratio.

[e] An upper temperature limit of 400 K is set by the range of available collision rates. Otherwise, the model results do not exclude higher temperatures for the warm gas.

[f] Area filling factor.

[g] Beam-averaged column density.

[h] Pressure.

Table 6.4 ^{12}CO Optical Depths in M82

	NE Lobe		SW Lobe	
J	$\tau_{\rm warm}$	$\tau_{\rm cool}$	$\tau_{\rm warm}$	$\tau_{\rm cool}$
1–0	0.9	0.4	0.7	0.9
2–1	3.4	0.9	2.8	1.9
3–2	6.7	0.7	5.6	1.3
4–3	9.8	0.2	8.4	0.2
5–4	11.5	0.02	10.4	0.01
6–5	10.7	1×10^{-3}	10.9	4×10^{-4}
7–6	7.1	5×10^{-5}	9.0	2×10^{-5}

Note. — Optical depths were computed in the LVG approximation from the median likelihood values listed in Table 6.3.

component accounts for a significant fraction of the total emission even in the J=2-1 transition. Thus, measurements of the high-J CO lines are helpful to understand not only the warm molecular gas, but also the cool molecular component that is essentially invisible above the J=4-3 line. This also explains why single-component models fail to account for the strong CO J=2-1 emission relative to J=1-0 and J=3-2. See, for example, Young and Scoville (1984) or Wild et al. (1992).

The total molecular mass can be estimated from the beam-averaged ^{12}CO column density. The models found an average column density of $< N(CO) > \approx 10^{18.2}$ cm^{-2} for a J=6-5 integrated intensity of $I \approx 200$ K km s^{-1}. I convert the CO column density to H_2 column density by assuming a CO/H_2 abundance of $X_{CO} = 10^{-4}$. The J=6-5 map has an average integrated intensity of 180 K km s^{-1} over an area of 1544 square arc seconds. Putting this together,

$$M_{mol} \approx 1.6 \times m_{H2} \times \frac{< N(CO) >}{X_{CO}} \times \frac{\iint T_A \, dv \, dA}{I} \, , \tag{6.10}$$

where m_{H2} is the mass of a single H_2 molecule and the factor of 1.6 accounts for the mass of helium, dust, etc., in the molecular clouds. Assuming a distance of 3.6 Mpc,

$M_{mol} = 1.7 \times 10^8\, M_\odot$. This value should be treated with caution, since there is no reason to expect the molecular mass to be proportional to ^{12}CO J=6-5 luminosity. It is nonetheless interesting to note that this estimate is within a factor of two of most other published values based on low-J ^{12}CO data and rare isotopomers (Carlstrom 1988; Wild et al. 1992; Mao et al. 2000; Weiß et al. 2001).

Based on simple geometric arguments, characteristic cloud sizes can be approximated as

$$S_{cloud} \approx \frac{N(CO)}{X_{CO}\, n(H_2)} \,. \tag{6.11}$$

If the area filling factor is close to unity, then this value should be considered an upper limit. Use of this expression gives very large sizes (tens or hundreds of parsecs) for warm clouds, and sizes of order one parsec or smaller for cool clouds. The number of clouds in the beam of diameter D_B can estimated with

$$N_{clouds} \approx X_{CO}^2\, D_B^2\, \frac{\Phi_A\, n^2(H_2)}{N^2(CO)} \,. \tag{6.12}$$

This number should be considered a lower limit if the area filling factor is close to unity. We see from this expression that the number of warm clouds is small, perhaps a few, while the number of cool clouds is quite large. The model results therefore suggest that the nucleus of M82 is a region containing a large number of small, cool clouds, and a small number of large, low-density warm clouds. The interferometer map in Figure 6.6, with a $1.5'' \times 1.4''$ beam size corresponding to about 25 parsecs, shows clumpiness at size scales consistent with these predictions. It should be noted, however, that the uncertainty of N_{clouds} (equation 6.12) is very large, since its calculation involves products and quotients of many quantities of significant uncertainty.

If the warm component in each lobe were a single spherical cloud, then for an area filling factor of $\Phi_A = 0.03$ in a $24.4''$ diameter beam, the cloud diameter is $4''$, or $\phi_{cloud} \approx 75$ pc. Assuming that ^{13}CO column density and visual extinction are

related by $N(^{13}CO) = 2 \times 10^{15} A_v$ cm^{-2} (Dickman 1978; Frerking et al. 1982) then for $N(^{13}CO) = 10^{18}$ cm^{-2}, the warm-cloud visual extinction is $A_v \approx 500$. Thus, to keep this gas warm, the cloud must be a star forming zone with stars scattered throughout the region.

The cool cloud ^{13}CO column density is around $10^{16.5}$ cm^{-2}. Using the same conversion factor between ^{13}CO column density and visual extinction as above, the cool cloud visual extinction is around $A_v \approx 16$, which is sufficient to shield the cloud from warming stellar radiation.

The 24.4″ beam-averaged visual extinction including both warm and cool components calculated from $< N(^{13}CO) >= 10^{16.7}$ cm^{-2} is $< A_v > \approx 25$. This is comparable to the range of A_v = 17–50 for a 27″ beam based on an isothermal grey-body fit to 40 μm – 3.3 mm continuum (Hughes et al. 1994). It should be noted that the continuum measurement should be sensitive to atomic gas not seen in the CO data. The beam-averaged H_2 column density can also be calculated from the ^{13}CO column density; assuming $N(H_2) = 5 \times 10^5 N(^{13}CO)$ (Dickman 1978), we find $< N(H_2) >= 10^{22.1}$ cm^{-2}.

Due in part to the nature of the model and the somewhat arbitrary distinction between "warm" and "cool" gas, the ratio of warm gas mass to cool gas mass is not well constrained. It is nonetheless interesting to note that the mass ratio likelihood distribution shown in Figure 6.9 and the warm component kinetic temperature shown in Figure 6.8 together suggest that over half of the molecular gas mass is warmer than the grey body dust temperature of 48 K measured with ISO and the JCMT (Colbert et al. 1999; Hughes et al. 1994). Detecting ^{13}CO in J=4-3 and J=6-5 would help constrain this mass ratio since column densities for the warm component could be more accurately determined at the lower optical depths of this species than with ^{12}CO.

Comparing the J=6-5 / J=2-1 line ratio map in Figure 6.7 to the measured intensities in Table 6.2, we see that the peak ratio at the hot spots is almost a factor of 2 higher than the 24.4″ values of 0.24 and 0.30 used in the LVG models for the NE and SW hot spots, respectively. This is likely to be largely an effect of beam filling

factor, and indicates that if a multi-line LVG analysis were to be performed using data obtained with a smaller beam size, an even larger fraction of the molecular gas would be found to be warm.

6.4 Conclusions

A two-component LVG model of the molecular gas in M82 is consistent with the measured ^{12}CO and ^{13}CO spectra up to J=7-6, and matches the large observed J=2-1/J=1-0 and J=2-1/J=3-2 ratios. Results of this model suggest that the nuclear region contains a large number of small, cool molecular clouds, and a small number of large, warm, low-density clouds.

I have demonstrated an approach to the evaluation of excitation models that provides important insight into how well the model parameters and various quantities derived from them are constrained by the measured data. This is accomplished by computing a likelihood density curve for each of the parameters and derived quantities. I have also demonstrated how prior knowledge and/or physical constraints can be incorporated into this evaluation. We find that a range of conditions is consistent with the measured M82 data. This is to be expected for a complicated region like a galactic nucleus; simple excitation models cannot be expected to determine precise results. On the other hand, simple models can be used to exclude large regions of parameter space.

The results of this analysis show that the most precisely determined quantity is the ^{13}CO beam-averaged column density, with a value of about 4.5×10^{16} cm^{-2} in both lobes. The beam-averaged column density of ^{12}CO was determined to within a factor of a few to be $10^{18.2}$ cm^{-2} in both lobes. The area filling factors were found to be near unity for the cool molecular gas, and around 0.03 for the warm molecular gas.

Median likelihood estimates of the isotopomer abundance ratio ^{12}CO/^{13}CO in the NE and SW lobes of M82 are 40 and 30, respectively. These estimates lie between the value of 25 for Galactic center clouds determined by Güsten (1989) and values

ranging from 50 to 100 for M82 determined by Mao et al. (2000) and Weiß et al. (2001).

Although the temperature of the warm molecular gas in the nucleus of M82 was not well constrained (no upper limit to the temperature was found), it is likely that over half of the total molecular mass is warmer than measured dust temperatures of 48 K.

The density of warm molecular gas in the nuclear region of M82 is low, with median likelihood estimates around 10^3 cm^{-3}. Cool molecular gas appears to be typically more dense than warm molecular gas. Median likelihood estimates for the warm gas and cool gas pressures in the two lobes range from $10^{4.4}$ to $10^{5.2}$ K cm^{-3}.

The ^{12}CO J=6-5 to ^{12}CO J=2-1 line ratio is at least five times larger in the SW lobe of M82 than in the galactic center, indicating that the proportion of molecular gas that is warm is significantly larger in the nuclear region of M82 than in the Galactic center.

Chapter 7 Concluding Remarks

This thesis described one small part of the complex web of research necessary to understand the molecular gas feeding star formation in starburst galaxies. Starting from electrical models, software was written to evaluate and optimize submillimeter heterodyne receiver designs. Using this software, a 690 GHz receiver was designed to observe J=6→5 rotational emission spectra of carbon monoxide in extragalactic sources. The receiver was used at the Caltech Submillimeter Observatory to map carbon monoxide emission toward the nearby starburst galaxy M82. These observations, along with measurements of nine other carbon monoxide emission lines were used to study the physical conditions of the molecular gas in the nucleus of the galaxy.

Research is an ongoing process. Each hard-earned answer suggests new questions, and each incremental improvement of a technology becomes a starting point for the next generation of advances. I will thus conclude this thesis by looking forward and saying a few words about where this research might lead.

Submillimeter receiver technology is developing at a rapid pace. Several new receivers are currently being designed and fabricated by the Caltech Submillimeter Wave Astrophysics group that will provide a major boost in capability over the current generation of instruments. Fast, accurate computer simulation and optimization tools including SuperMix are enabling this rapid development. SuperMix works, but there is still room for continued improvement. In particular, due to the lack of a comprehensive user's guide, only a few people outside of Caltech have been able to take advantage of the possibilities that this software offers. Expanding to a larger pool of users would ensure that the full potential of this new software tool is realized. The long-term usability would be further enhanced if the users begin to add new components to the library as receiver technology evolves to utilize new and different materials and techniques. We have provided a valuable tool to the receiver development community, but the task still remains to make it more generally accessible.

Improving the performance of the receiver would be straightforward. First, the low-noise IF amplifier could be retuned for lower noise and flatter gain. The mixer chip could be redesigned to lower its capacitance; a lower capacitance would allow a better impedance match to the IF amplifier, with the result being lower, flatter noise across the IF passband. Taking the details of the circuit geometry around the SIS mixer chip into account, it should be possible to keep the gain flat and the noise low across the entire 4 GHz of IF bandwidth. The noise could be further reduced by carefully minimizing optics losses.

After the performance of the single-mixer receiver has been fully optimized, two mixers could be combined as a correlation receiver to eliminate the need for beam switching (Blum 1959; Faris 1967; Predmore et al. 1985). This system would increase the on-source integration time by a factor of 2.5 to 3, and the subtraction of correlated sky noise would be significantly improved. Simultaneously observing both polarizations of the incoming radiation could further improve the sensitivity of the receiver by a factor of $\sqrt{2}$.

The next step for the study of molecular gas in M82 would be to observe ^{13}CO emission in the J=4→3 and J=6→5 transitions to improve constraints on the column density, isotopomer abundance ratio, and molecular gas mass. The observations and excitation analysis should be repeated for many different starburst galaxies. The results of such a survey could then be studied to find trends that apply to starburst galaxies in general.

The Atacama Large Millimeter Array (ALMA) is scheduled to begin operation as early as 2006 (ALMA web page). The site is located at an altitude of 16,400 feet in the dry Andes mountains of northern Chile, and has better weather for submillimeter astronomy than Mauna Kea. The zenith transmission in the 650 GHz window is higher than 40% over a quarter of the time. With 64 12 meter dishes, the total collecting area will be 85 times larger than the CSO's 10.4 meter antenna, and baselines up to 14 km will enable spatial resolutions as high as $0.01''$, corresponding to 0.2 pc at the distance of M82.

After it goes on-line, ALMA should be used to observe CO in M82 as well as

many other starburst galaxies. ALMA's high spatial resolution will enable individual molecular clouds in nearby galaxies to be resolved, and its high sensitivity should enable the detection and mapping of high-J lines of optically thin CO isotopomers. Excitation analyses similar to those presented in Chapter 6 could be repeated at high resolution. Such observations will greatly improve our understanding of the interstellar medium of starburst galaxies.

Appendix A The SuperMix Circuit Connection Algorithm

An overview of composite circuits in SuperMix was given in Section 2.4, which described how SuperMix calculates composite circuits one connection at a time using the method of subnet growth. A binary tree of connections is formed, with the composite circuit forming the base of the tree, the user-defined circuit elements the tips of the branches, and each connection a branch of the tree; see Figure 2.3.

An example was presented in Section 2.9.1 of how a composite circuit can be simulated. The circuit is represented as an object of type `class circuit`. The components of the circuit are connected by calling the `connect` member function of `class circuit`. The order of the unconnected ports in the composite circuit are specified with the `add_port` member function. Once the circuit has been specified by the appropriate calls to these functions, the circuit behaves just like any other linear device in SuperMix, and can itself be used in other, more complex circuits.

In this appendix, we will first examine two classes used extensively in building composite circuits, i.e., `class port` and `class connection`. We will then examine the workings of `class circuit` in more detail, listing some of its more important member data structures and presenting algorithms for several of its member functions.

A.1 Identifying Ports

Every device in SuperMix is automatically assigned a unique number called a "device ID." Each device, in turn, assigns an integer to each of its ports. Thus, any port within a simulation can be uniquely identified with a (device ID, port number) pair. SuperMix defines a `class port` data type to hold this pair. A connection can then be specified with a pair of `class port` objects identifying the two ports to be connected.

A.2 A C++ Connection Class

When two ports are connected, the actual math to calculate the resultant scattering matrix $\mathcal{S}$, noise correlation matrix $\mathcal{C}_S$, and source wave vector $\boldsymbol{B}$ is performed by the `connection` class. A `connection` is an intermediate subcircuit used in the calculation of a `circuit`; it is derived from the same generic device class as any other device, and so behaves in the same way. A `connection` can be created both from components defined by the user (like resistors and microstrip lines) as well as from other `connection` devices. Since `connection` objects hold pointers to the devices they are connecting, they form the nodes of the tree data structure described earlier.

The `connection` class knows how to perform three different types of connections. The first and most common is the *interconnection*, when the two ports to be connected are on physically distinct components. *Intraconnections*, on the other hand, are performed when both ports to be connected are already on the same device. Finally, sometimes two devices are to be joined without connecting any ports at all. In this case, the scattering matrices of the two devices are combined into a single block-diagonal matrix. For lack of a better term, I will refer to these as *null connections*.

The equations used to calculate the $\mathcal{S}$ and $\mathcal{C}_S$ matrices and the $\boldsymbol{B}$ vector were taken from Wedge (1991). If the circuit being calculated is passive and all components are at the same temperature, then to save time, `connection` does not calculate the noise correlation matrix $\mathcal{C}_S$, leaving it to be calculated later from equation 2.7.

The `connection` class is never used directly by the user. The `circuit` class automatically creates, uses, and destroys `connection` instances as necessary to build and calculate the composite circuits.

A.3 The Circuit Connection Algorithm

The following sections outline the most important members of the `circuit` class, including data structures and member functions.

A.3.1 Important Data Structures

The following data structures are used by `class circuit` to keep track of the elements of the circuit, the ports to be connected, the order of the ports in the resulting circuit, the connection tree, etc.

`treeBase` – The base of the tree of connections (see Figure 2.3).

`elementSet` – The set of circuit elements to be connected.

`connectionStack` – A stack of the connections to be made, i.e., pairs of ports to be connected.

`portOrderVector` – A vector specifying the order of ports in the final circuit.

`deleteStack` – A stack of `class connection` subcircuits, so that we can free them from memory when this circuit is destroyed.

A.3.2 Specifying Port Order

The member function `add_port(dev, port)` is called by the user to specify the port order in the final circuit. The first call specifies which port is to be port 1, the second call specifies which port is to be port 2, etc. The algorithm is as follows:

- Check that the device and port are valid.
- Check that the port hasn't already been connected somewhere.
- Add the device to the `elementSet`.
- Add the port to the `portOrderVector`.

A.3.3 Specifying a Connection

The member function `connect(devA, portA, devB, portB)` is called by the user to specify a connection. The algorithm is as follows:

- Check that the devices are valid.

- Check that the ports haven't already been used somewhere.
- Create a 2-element port array to represent this connection.
- Add the 2-element port array to the `connectionStack`.
- Add the devices to the `elementSet`.

A.3.4 Building the Circuit Tree

The tree of circuit connections has to be built the first time the circuit is calculated. This is done by the function `build_tree`. Once the tree has been built, it can be reused for each new calculation, such as at each point of a frequency sweep. The following is the algorithm for `build_tree`.

- Create a local copy of the `elementSet` (so that we can modify it).
- Create a local copy of the `connectionStack` (so that we can modify it).
- Create a temporary set of devices called `tmpDeviceSet`.
- If `deleteStack` is not empty,
    - Delete all devices on the stack.
- While `connectionStack` is not empty:
    - Pop a pair of ports to be connected off the `connectionStack`.
    - Find the first port to be connected:
        - Check in the `elementSet`.
            - If not found, check in the `tmpDeviceSet`.
                - If not found, then report the error.
    - Get the second port to be connected:
        - Check in the `elementSet`.
            - If not found, check in the `tmpDeviceSet`.
                - If not found, then report the error.
    - Perform the connection:
        - Create a new `connection` instance.

        - ▷ Add it to `deleteStack`.
        - ▷ Add it to the `tmpDeviceSet`.
- While there is still more than 1 device left in the `elementSet`:
    - Pop two devices off the `elementSet`.
    - Create a new "null connection" `connection` instance from them.
    - Add the new device to the `deleteStack`.
    - Add the new device to the `tmpDeviceSet`.
- If `elementSet` is still not empty,
    - Pop the last device off of the `elementSet`; call it `lastDevice`.
- else
    - Pop a device off of the `tmpDeviceSet`, call it `lastDevice`.
- While `tmpDeviceSet` is not empty:
    - Pop a device off the `tmpDeviceSet`.
    - Create a new `connection` instance "null connecting" it to `lastDevice`.
    - Add the new `connection` instance to `deleteStack`.
    - Call the new `connection` instance `lastDevice`.
- The final `lastDevice` is the `treeBase`.

A.3.5 Calculating the Composite Circuit

The following algorithm describes the function that is called to ask the circuit to calculate its scattering matrix, noise correlation matrix, and source vector.

- If the tree isn't built, then build it.
- Verify that all ports were either connected or specified with `add_port`.
- If necessary, set the global temperature to the temperature of this circuit, remembering the previous global temperature.
- Ask the `treeBase` for its scattering matrix, noise correlation matrix, and source wave vector.

- Sort the elements of the resulting matrices and vector so that the ports have the order specified by the `portOrderVector`.
- Transform the data to the correct normalization impedance if necessary.
- Set the global temperature back to its original value.

Appendix B
Noise from Lossy Transmission Lines of Non-Uniform Temperature

The Johnson noise power per unit bandwidth emitted by a lossy transmission line of uniform temperature is proportional to the loss times the temperature. With cryogenic systems, however, lossy coaxial cables often must be run between stages at different temperatures. In this appendix, expressions will be derived for the noise power of lossy transmission lines of non-uniform temperatures. An expression for the special case of a transmission line with a constant temperature gradient will be presented.

A specific application where the improved accuracy of these equations is useful is the noise measurement of cryogenic amplifiers as described in Chapter 3. With this system, a 50 Ω terminator is heated to serve as a calibrated noise source. A coaxial cable between the heated terminator and the device under test must have reasonably low thermal conductivity, which in practical systems means the cable will also be electrically lossy at high frequencies. I will calculate the noise power at the device-end of the terminated cable for this special case.

B.1 The General Case

Consider a section of transmission line with amplitude loss α nepers per unit length. For a segment of the line of length Δx, the power transmission is

$$\mathbb{T} = \exp(-2\,\alpha\,\Delta x)\ . \tag{B.1}$$

For small Δx, or more precisely, for $\alpha\,\Delta x \ll 1/2$, the expression for the transmission of the segment can be approximated by the first two terms of the Taylor expansion of equation B.1:

$$\mathbb{T} \approx 1 - 2\,\alpha\,\Delta x\ . \tag{B.2}$$

The noise power coming out of any small segment of the transmission line can be expressed as a function of the temperature of the segment and the noise power going into the segment. With $T(x)$ defined as the temperature of the line at x and $P(x)$ defined as the noise power at x traveling in the $+x$ direction,

$$P(x + \Delta x) \approx P(x)\,\mathbb{T} + k_B\,\Delta\nu\,T(x)\,(1 - \mathbb{T})\ . \tag{B.3}$$

Substituting the Taylor expansion for $\mathbb{T}$ into equation B.3 and rearranging gives

$$\frac{P(x + \Delta x) - P(x)}{\Delta x} \;\approx\; 2\,\alpha(x)\,[k_B\,\Delta\nu\,T(x) - P(x)]\ , \tag{B.4}$$

where for generality we have allowed the loss α to be a function of position. In the limit of small Δx, this expression becomes exact and is equivalent to the general differential equation

$$\frac{dP}{dx} = 2\,\alpha(x)\,[k_B\,\Delta\nu\,T(x) - P(x)]\ , \tag{B.5}$$

where $T(x)$ is the temperature at location x, $P(x)$ is the noise power traveling in the positive x direction at x, and $\alpha(x)$ is the loss in nepers per unit length of the transmission line, also at x.

B.2 Constant Temperature Gradient

In general, both the thermal and electrical conductivities of the cable will be functions of temperature, and so both $T(x)$ and $\alpha(x)$ will vary across the cable in some

non-linear way. Thus, to use equation B.5 in full generality, it would be necessary to measure the loss α as a function of temperature, and either measure the thermal conductivity of the cable as a function of temperature to calculate $T(x)$ or measure $T(x)$ directly. The results of these measurements would then be used to solve equation B.5 numerically. Usually, however, this high level of accuracy is not necessary; in these cases, it may be adequate to assume that the variation of the loss and thermal conductivity with temperature are not important to find an analytic approximation for the noise power. For a transmission line of length L held at temperature T_0 at $x = 0$ and T_L at $x = L$, assuming a constant temperature gradient along the line,

$$T(x) = T_0 + \frac{x}{L}\,(T_L - T_0)\ . \tag{B.6}$$

Defining $\Delta T \equiv T_0 - T_L$ and inserting equation B.6 into equation B.5 gives

$$\frac{dP}{dx} = 2\,\alpha\left[k_B\,\Delta\nu\,T_0 - \frac{x}{L}\,k_B\,\Delta\nu\,\Delta T - P(x)\right]\ , \tag{B.7}$$

where we have assumed that the loss α is independent of position.

The general solution to equations of this form is

$$P(x) = a\,e^{-x/b} + c\,x + d\ . \tag{B.8}$$

Three of the constants can be found by substituting the general solution B.8 back into equation B.7. To find the fourth and final constant it is necessary to impose a boundary condition for the input noise power. In the case of $P(0) = 0$,

$$P(x) \quad = \quad k_B\,\Delta\nu\left[T_0 + \frac{\Delta T}{2\,\alpha\,L} - \frac{x}{L}\Delta T - \left(\frac{\Delta T}{2\,\alpha\,L} + T_0\right)\exp(-2\,\alpha\,x)\right] \quad . \tag{B.9}$$

If the loss is expressed in terms of attenuation A in decibels, then the noise power

out of the transmission line $P_{out} \equiv P(L)$ is

$$P_{out} = k_B \, \Delta\nu \left[T_0 \left(1 - 10^{-\frac{A}{10}}\right) - \Delta T \left(1 - \frac{10(1 - 10^{-\frac{A}{10}})}{A \ln 10} \right) \right] . \tag{B.10}$$

If $\alpha L \ll 1/2$, then the noise power originating in the transmission line is not appreciably attenuated. As expected, to first order in αL the output power goes to

$$P_{out} \approx \frac{1}{2} \, k_B \, \Delta\nu \, (T_0 + T_L) \left(1 - 10^{-\frac{A}{10}}\right) . \tag{B.11}$$

This is equivalent to assuming that the entire cable is at the average temperature $\overline{T} = (T_0 + T_L)/2$.

B.3 A Terminated Cable as a Thermal Noise Source

We will now find the noise power from a lossy coaxial cable with a matched load at temperature T_L at one end and held at T_A at the other end. We will assume a constant temperature gradient on the cable, and that the loss per unit length α is independent of position. From equation B.10, the noise power from the cable, with $\Delta T \equiv T_L - T_A$, is

$$P_{cable} = k_B \, \Delta\nu \left[T_L \left(1 - 10^{-\frac{A}{10}}\right) - \Delta T \left(1 - \frac{10(1 - 10^{-\frac{A}{10}})}{A \ln 10} \right) \right] . \tag{B.12}$$

The noise power contribution from the matched load is

$$P_{term} = k_B \, \Delta\nu \, T_L \, 10^{-\frac{A}{10}} . \tag{B.13}$$

Summing these two terms and simplifying, the total noise power is

$$P_{out} = k_B \, \Delta\nu \left[T_A + \frac{10 \, \Delta T \left(1 - 10^{-\frac{A}{10}}\right)}{A \ln 10} \right] . \tag{B.14}$$

Figure B.1 shows the correction to the load temperature as a function of cable

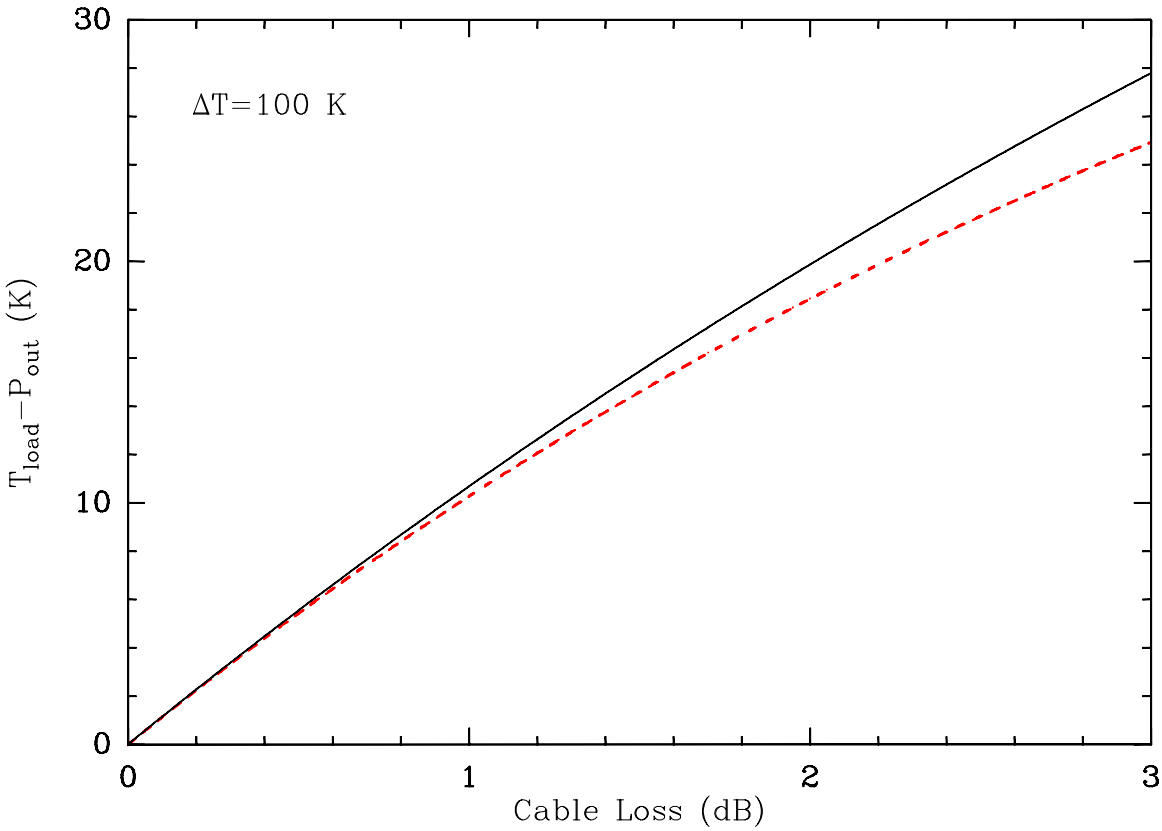

Figure B.1 Correction to the noise power from a heated-terminator noise source for $\Delta T = 100$ K. The calibration standard is described in Section 3.4.1. The solid black curve (calculated from equation B.14) is the correction to be subtracted from the resistor temperature. The dashed curve is the correction to first order in the loss, calculated by assuming that the entire cable is at the average of the temperatures of its two ends.

loss for $\Delta T = 100$ K. The plotted correction in Kelvin is to be subtracted from the load temperature. This figure is especially useful for estimating the magnitude of the error of a particular assumption.

Appendix C Measured Spectra

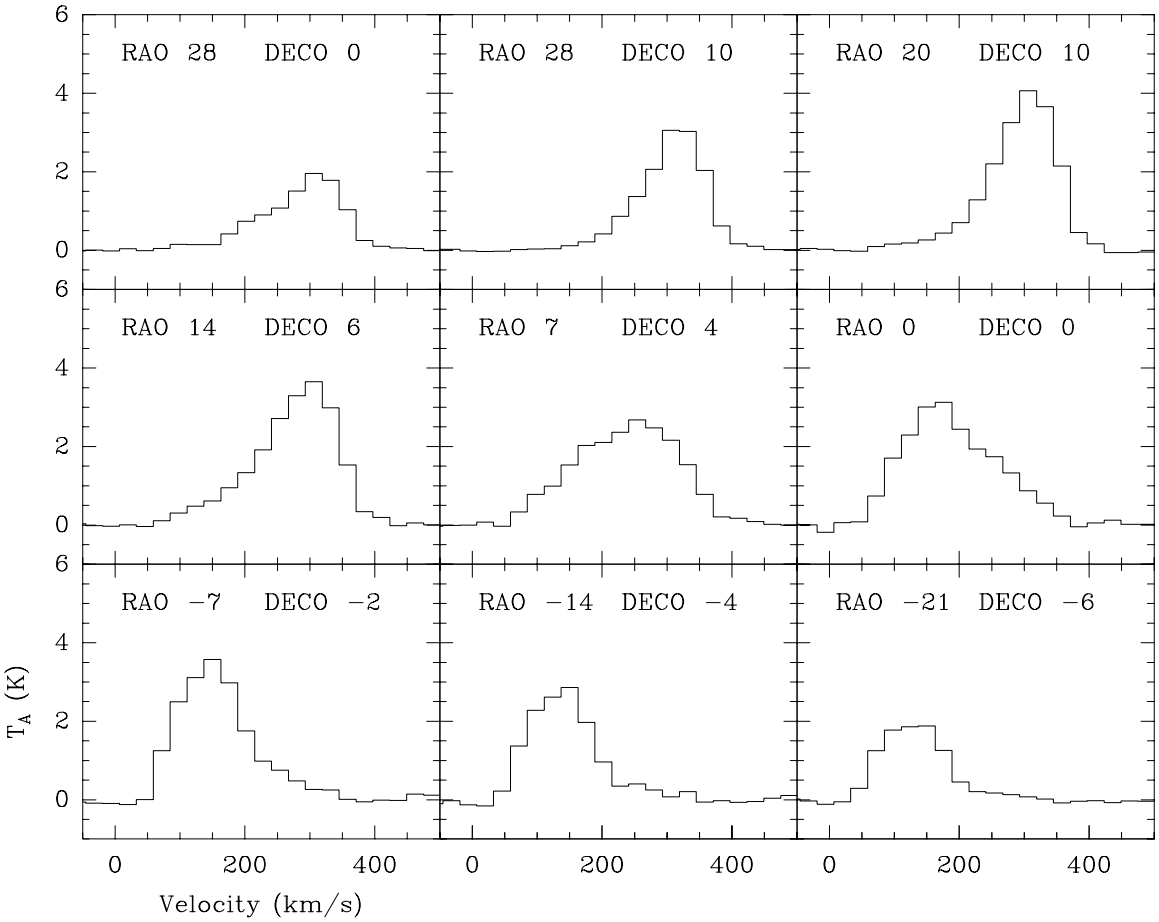

Figure C.1 ^{12}CO J=3→2 spectra. The beam FWHP was 24.4". The spectra were corrected for an efficiency of 50% based on observations of Mars. A zeroth order baseline was subtracted from each spectrum. The pointing offsets are in seconds of arc from RA $09^h55^m51.2^s$ Dec $69°40'44''$ J2000.

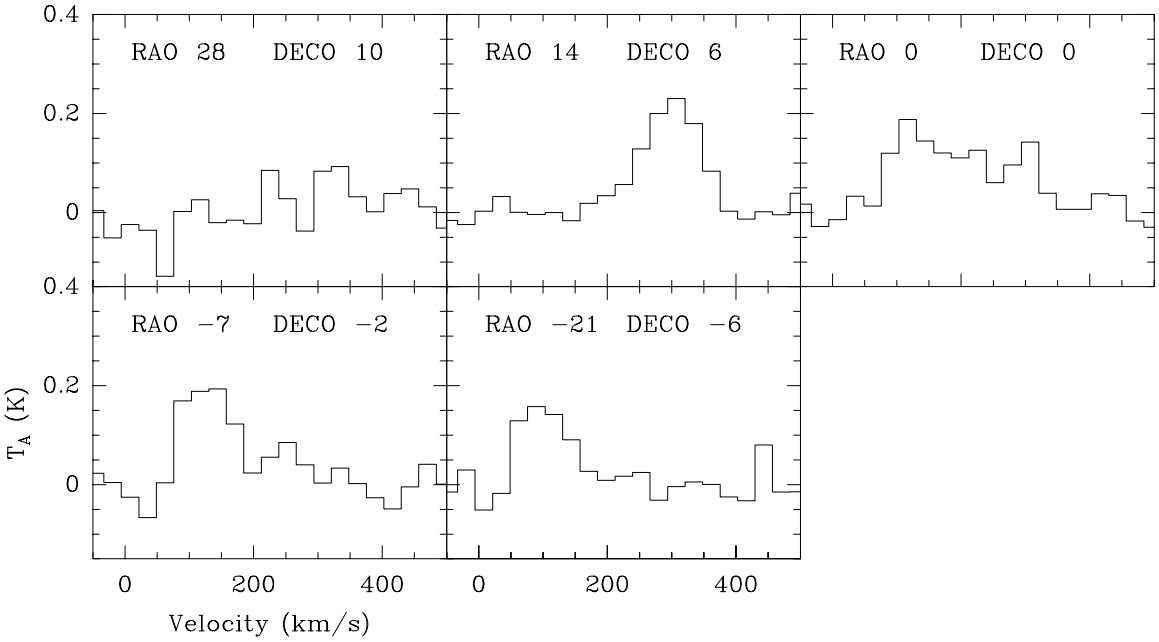

Figure C.2 ^{13}CO J=3→2 spectra. The beam FWHP was 25.5". The spectra were corrected for an efficiency of 50% based on observations of Mars. The results were scaled up an additional 14% to correct for sideband imbalance due to atmospheric transmission. A zeroth order baseline was subtracted from each spectrum. The pointing offsets are in seconds of arc from RA $09^h55^m51.2^s$ Dec 69°40′44″ J2000.

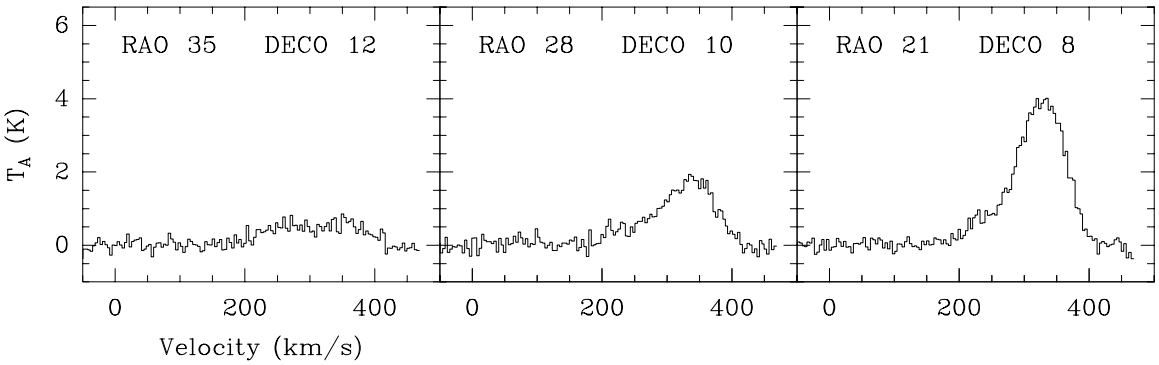

Figure C.3 ^{12}CO J=4→3 spectra. The beam FWHP is was 16.4". The spectra were corrected for an efficiency of 45% based on observations of Mars and Saturn. A first order baseline was subtracted from each spectrum. The pointing offsets are in seconds of arc from RA $09^h55^m51.2^s$ Dec 69°40′44″ J2000.

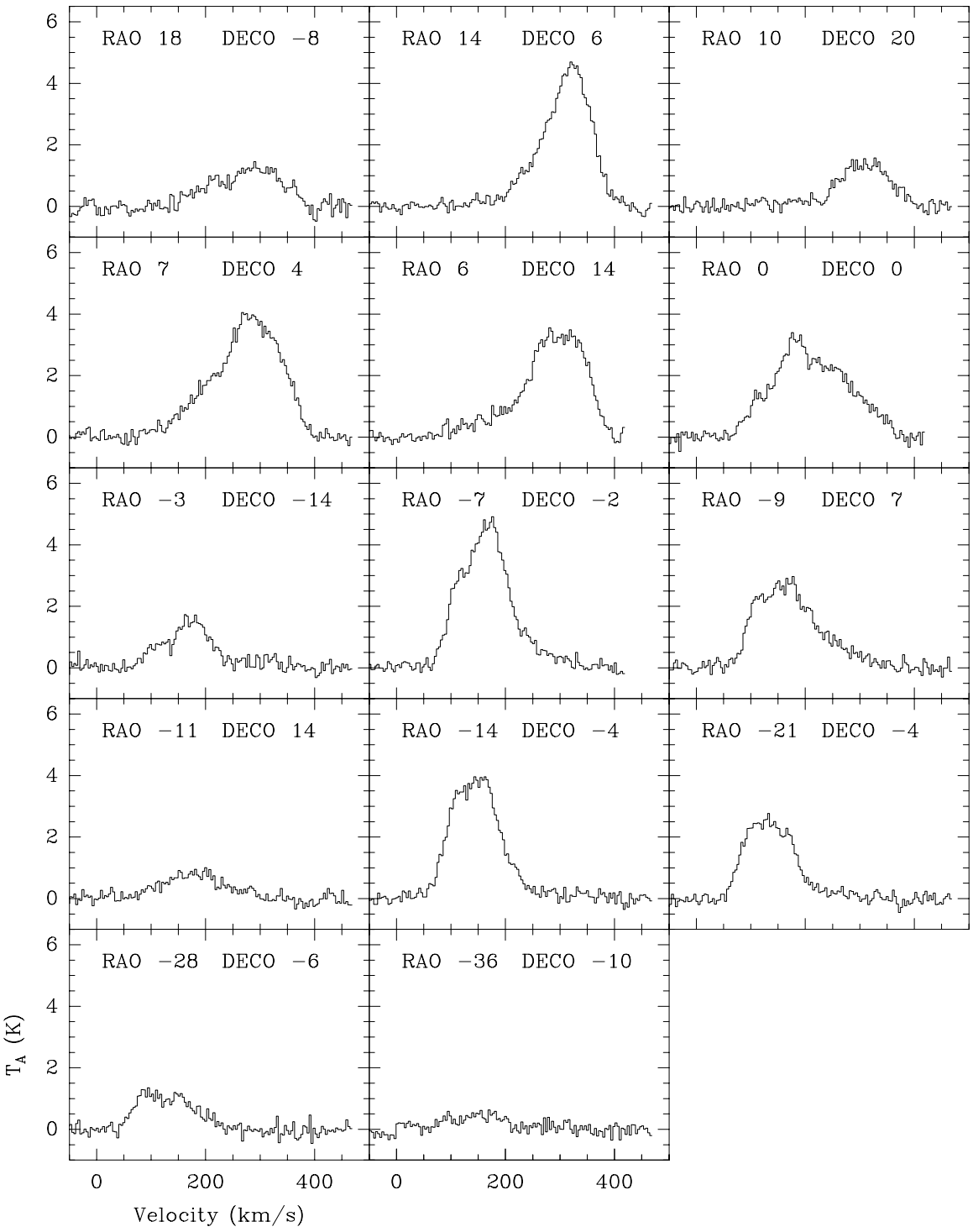

Figure C.3 — *Continued*

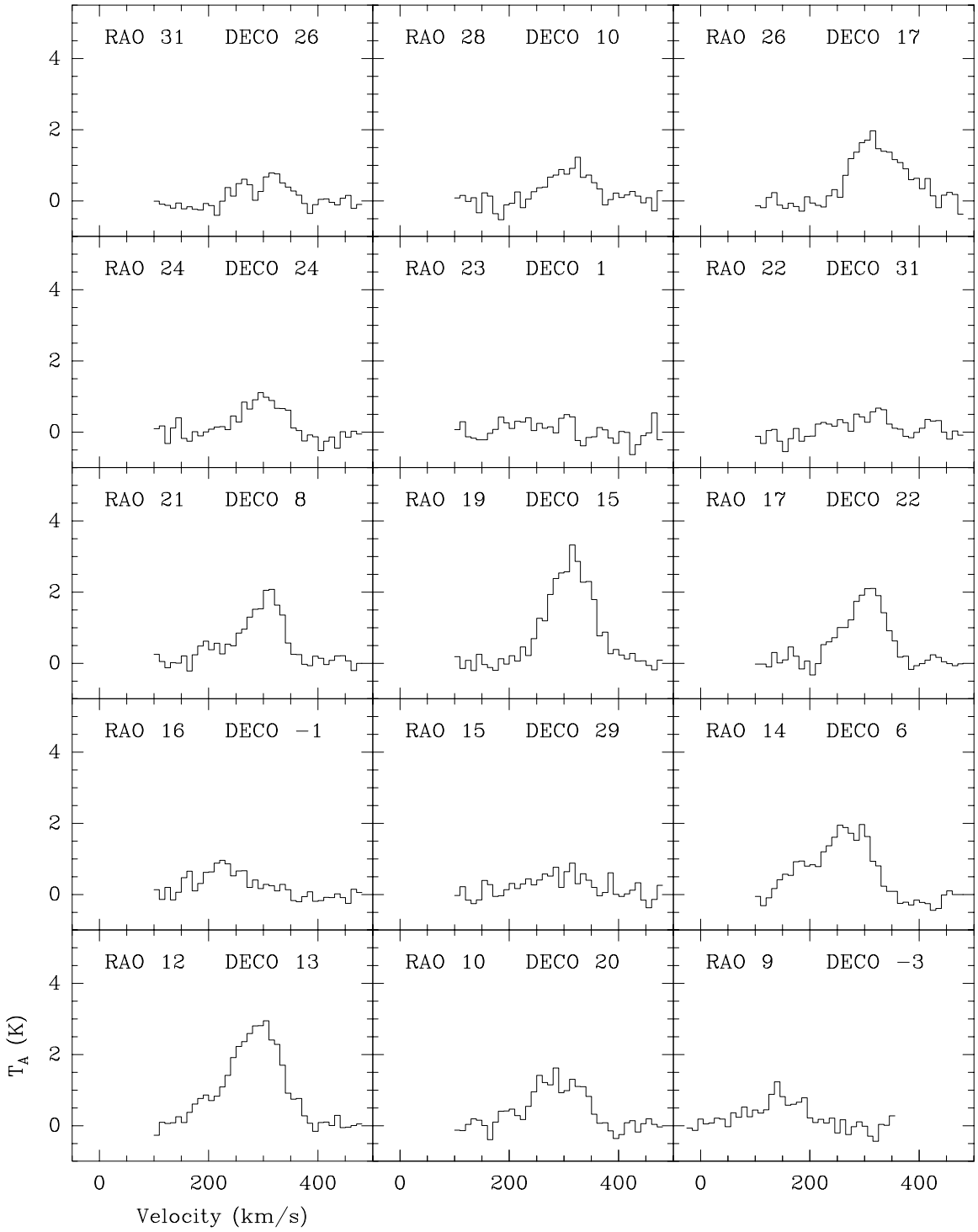

Figure C.4 ^{12}CO J=6→5 spectra. The beam FWHP was 14". The spectra were corrected for an efficiency of 30% based on observations of Saturn. A zeroth order baseline was subtracted from each spectrum. The pointing offsets are in seconds of arc from RA $09^h55^m50.3^s$ Dec $69°40'37''$ J2000.

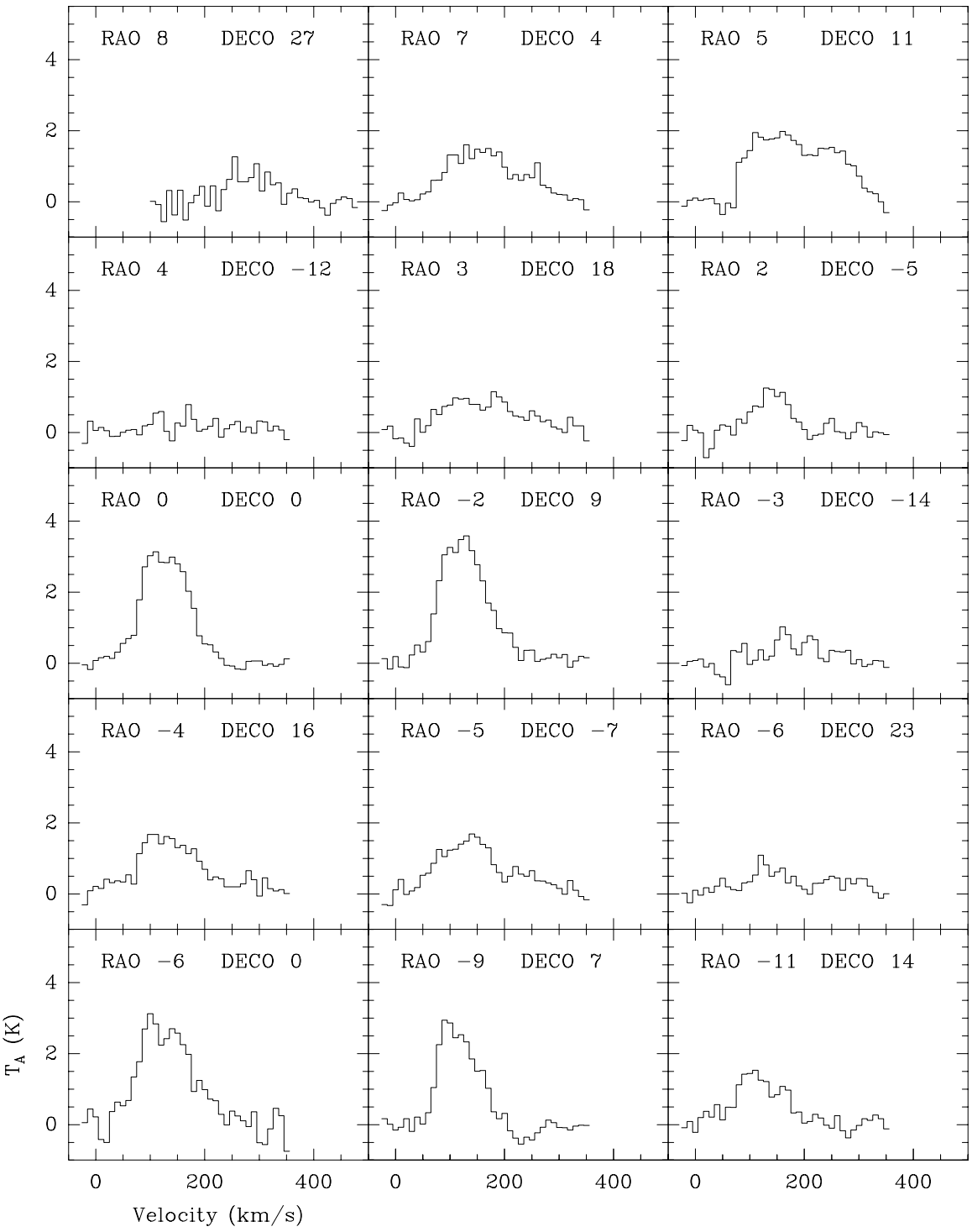

Figure C.4 — *Continued*

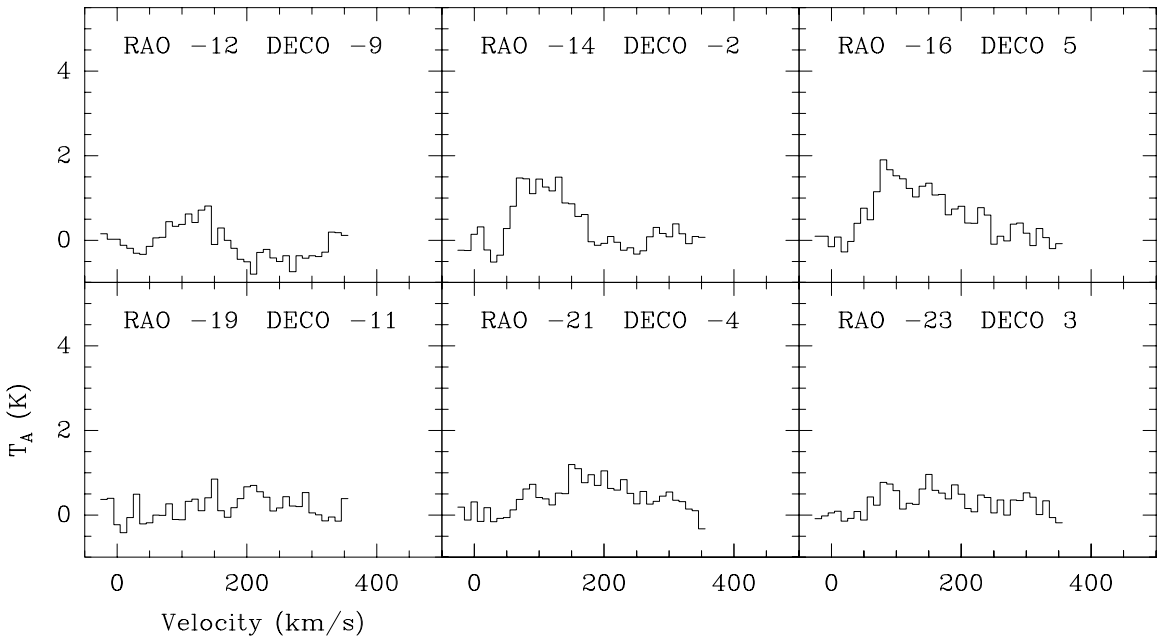

Figure C.4 — *Continued*

Appendix D Ratio Map Calculation

A straightforward approach to computing a ratio between two maps is to smooth the higher-resolution map to the resolution of the lower, and divide integrated intensities directly. This technique has three drawbacks. First, it throws away the line profile information, which from inspection of Figure C.1 can be seen to contain information about position. Secondly, smoothing throws away spatial information. Finally, noise causes the error in division to become large as the signal levels decrease.

I have employed a calculus of variations approach to compute a line ratio map that uses all available information, and is well behaved as the signal-to-noise ratio decreases away from bright centers. Furthermore, with this method, a Lagrange multiplier provides a natural way to adjust the resolution of the resulting ratio map. This method is similar to the linear regularization methods described in *Numerical Recipes in C* (Press et al. 1992).

In general, we expect any region of a galaxy with ^{12}CO J=6-5 emission to also emit in ^{12}CO J=2-1. Furthermore, the spectral line profiles at any given location in a galaxy in the two transitions are likely to be similar if observed at high spatial resolution. Therefore, we assume that the measured J=6-5 emission can be modeled as the interferometric J=2-1 data times a line ratio map, convolved to the resolution of the measured J=6-5 data,

$$T_{6-5}(\mathbf{r}, v) = \int G(\mathbf{r} - \mathbf{r}\,') \; T_{2-1}(\mathbf{r}\,', v) \; \rho(\mathbf{r}\,') \; d\mathbf{r}\,' \; , \tag{D.1}$$

where $\mathbf{r}$ is the mapping offset, $G(\mathbf{r} - \mathbf{r}\,')$ is the smoothing kernel which convolves the J=2-1 beam to the J=6-5 beam, $\rho(\mathbf{r})$ is the unknown ratio map, and v is the velocity.

All spectra are resampled so that the velocity channels are the same for both maps. The positions observed, on the other hand, will typically be different. Since

the data are discrete, we define matrix F as follows:

$$F_{ij} \equiv G(\mathbf{r}_i - \mathbf{r}_j{}') \; T_{2-1}(\mathbf{r}_j{}', v_i) \,/\, \sigma(\mathbf{r}_i, v_i) \; , \tag{D.2}$$

where the index i represents a velocity channel at a particular mapping offset $(\mathbf{r}_i, v_i)$ in the J=6-5 data, j represents a spatial position $\mathbf{r}_j{}'$ in the J=2-1 map, and with $\sigma(\mathbf{r}_i, v_i)$ defined as the standard deviation of the channel $(\mathbf{r}_i, v_i)$ in the J=6-5 data.

The ratio map $\rho(\mathbf{r})$ is written as a vector $\boldsymbol{\rho}$, where each element ρ_j represents the line ratio at offset $\mathbf{r}_j$ in the map. The ratio map is sampled on the same coordinate grid as the ^{12}CO J=2-1 map. The J=6-5 map is represented as a vector $\mathbf{t}$, where t_i is the sigma-normalized antenna temperature of channel i,

$$t_i = T_{6-5}(\mathbf{r}_i, v_i) \,/\, \sigma(\mathbf{r}_i, v_i) \; . \tag{D.3}$$

With these definitions, we can now calculate the sigma-normalized chi squared,

$$\chi^2 \equiv [\, F\,\boldsymbol{\rho} - \mathbf{t}\,]^2 \;\; . \tag{D.4}$$

If $\boldsymbol{\rho}$ is adjusted to minimize χ^2, the resultant ratio map will tend to track the noise in the J=6-5 map. To avoid this undesirable behavior, we define a function that is minimized when $\boldsymbol{\rho}$ is smooth. The integral of the square of the gradient of $\rho(\mathbf{r})$ has this property. We define

$$S \equiv \int |\nabla \rho(\mathbf{r}\,)|^2 \, d\mathbf{r} \; . \tag{D.5}$$

In the discrete case, a symmetric nonnegative-definite matrix D can be found such that

$$S = \boldsymbol{\rho}\, D\, \boldsymbol{\rho} \; . \tag{D.6}$$

We introduce a Lagrange multiplier, λ, and solve $\delta\,(\chi^2 + \lambda S) = 0$ to minimize S for

a constant χ^2. This expression reduces to

$$\left(F^T F + \lambda D\right) \boldsymbol{\rho} = F^T \, \mathbf{t} \; . \tag{D.7}$$

For $\lambda > 0$, $F^T F + \lambda D$ is symmetric and positive definite, and therefore nonsingular. Thus, there exists a unique solution for $\boldsymbol{\rho}\,(\lambda)$.

Large values of λ will weight the smoothness function S more heavily in the minimization, resulting in a smoother ratio map and a higher χ^2. Small λ will result in a lower χ^2 but a noisier ratio map. Thus, the parameter λ can be adjusted to obtain a suitable trade-off between spatial resolution and noise. Note that large values of λ introduce the systematic effect of forcing the entire ratio map to a constant value. If the signal-to-noise ratio of the data is sufficiently high and the smoothing kernel G is well-known, λ can be made small enough that the ratio map will approach the resolution of the denominator map. Thus, this technique is a deconvolution since the ratio map can be at a higher resolution than the numerator map.

I computed ratio maps for a variety of values of λ, and selected Figure 6.7 based primarily on visual inspection. To aid this selection, I also calculated residuals by finding the difference between the measured J=6-5 data and $T_{6-5}(\mathbf{r}, v)$ computed in equation D.1. The RMS residual per channel of the fit shown in Figure 6.7 is 0.34 K. The integrated intensity of the residuals are shown in Figure D.1.

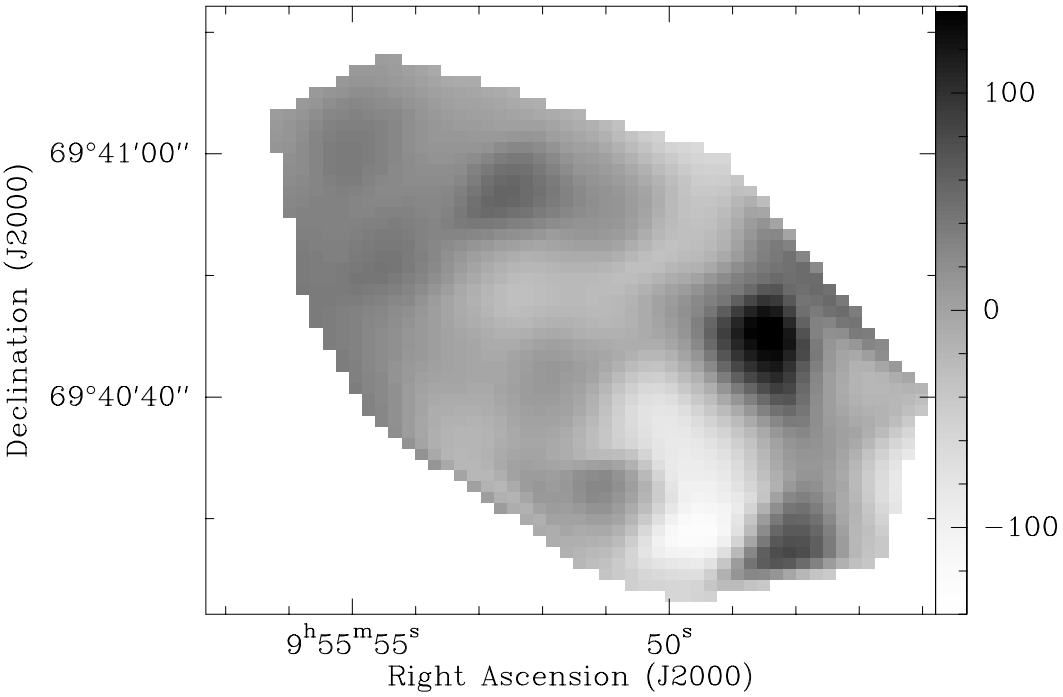

Figure D.1 Residuals of the ^{12}CO J=6-5 / J=2-1 line ratio map shown in Figure 6.7. The units are K km s^{-1}. The larger errors in the SW end of the galaxy may be due to a pointing drift during the observations.

Appendix E A Fast LVG Solver

In the following review of excitation analysis in the large velocity gradient approximation, the math and algorithms used in the computer codes described in Chapter 6 will be presented along with example results.

E.1 The CO Rate Balancing Equation

The primary processes by which a CO molecule in an interstellar molecular cloud can change rotational quantum state J are collisions with H_2 and He, spontaneous emission, stimulated emission, and absorption. Define $C_{J,J'}$ as the rate per CO molecule of collision-induced transitions from state J to state J' in frequency units. This will be proportional to the number density of the exciting particles (H_2 and He) and depends on the velocity distribution and quantum state populations of the exciting particles. Assume that the velocity distribution can be described by a kinetic temperature T_{kin} and that the temperature is too low to excite the H_2 out of the lowest-energy ortho and para states. One can then decompose $C_{J,J'}$ as

$$C_{J,J'}(T_{kin}) = n_{para} \times \gamma^{para}_{J,J'}(T_{kin}) \; + \; n_{ortho} \times \gamma^{ortho}_{J,J'}(T_{kin}) \; + \; n_{He} \times \gamma^{He}_{J,J'}(T_{kin}) \; , \tag{E.1}$$

where $\gamma_{J,J'}$ is the collisional excitation rate per exciting molecule.

For spectral emission with intensity I_ν and a normalized isotropic line shape $\phi(\nu)$, the average radiation field is

$$J = \frac{1}{4\pi} \int d\Omega \int d\nu \, I_\nu(\Omega) \, \phi(\nu) \; . \tag{E.2}$$

Since the only allowed electric dipole rotational transitions for linear molecules are for $\Delta L = \pm\hbar$, the radiation field J can be expressed as a vector $\boldsymbol{J}$, where $J_j \equiv J_{j,j-1}$.

One can use the collision rate matrix $\mathcal{C}$ and the average radiation field $\boldsymbol{J}$ to write an equation for the rate of change of the number density n_j of a particular state j of the CO:

$$\frac{dn_j}{dt} = n_{j+1}\,(A_{j+1,j} \,+\, B_{j+1,j}\,J_{j+1}) \,+\, n_{j-1}\,B_{j-1,j}\,J_j \,+\, \sum_{i\neq j} n_i\,C_{ij} \\ -\, n_j\,(A_{j,j-1} \,+\, B_{j,j-1}\,J_j \,+\, B_{j,j+1}\,J_{j+1}) \,-\, n_j \sum_{k\neq j} C_{jk}\,. \quad \text{(E.3)}$$

Define $C_{jj} \equiv 0$ to simplify the summation, and divide through by n_{CO} to make the equations independent of the CO density. To further simplify the notation, define $\chi_j \equiv n_j/n_{CO}$. For a steady-state solution, $dn_j/dt = 0$ and

$$\chi_{j+1}\,(A_{j+1,j} \,+\, B_{j+1,j}\,J_{j+1}) \,+\, \chi_{j-1}\,B_{j-1,j}\,J_j \,+\, \sum_{i} \chi_i\,C_{ij} \\ -\, \chi_j\,(A_{j,j-1} \,+\, B_{j,j-1}\,J_j \,+\, B_{j,j+1}\,J_j + 1) \,-\, \chi_j \sum_{k} C_{jk} \;=\; 0\,. \quad \text{(E.4)}$$

This equation defines the matrix relation

$$\mathcal{F}(\boldsymbol{J}, T_{kin}) \cdot \boldsymbol{\chi} \;=\; 0\,. \quad \text{(E.5)}$$

To have a non-zero solution for $\boldsymbol{\chi}$, $\mathcal{F}$ must be singular. To have a unique solution (to within a constant factor), the null space of $\mathcal{F}$ must be one-dimensional. For a closed system with N levels (J=0 to J=N-1), all transition rates into or out of the system, such as $A_{N,N-1}$, must be set to zero. Bearing that in mind, it can be shown that the N equations defined by equation E.4 are degenerate because they sum to 0. In other words, any single equation j of E.4 or row of $\mathcal{F}$ is equal to the opposite of the sum of all the other equations or rows. Equation E.5 can be repaired by replacing one degenerate row with a normalization relation for $\boldsymbol{\chi}$, since

$$\sum_j \chi_j = 1\,. \quad \text{(E.6)}$$

For example, set all elements of the last row of $\mathcal{F}$ to 1, and the corresponding element of the RHS also to 1. Define $b_j \equiv \delta_{j,N-1}$. Then, with this new definition of $\mathcal{F}$, the equation

$$\mathcal{F}(\boldsymbol{J}, T_{kin}) \cdot \boldsymbol{\chi} \;=\; \boldsymbol{b} \tag{E.7}$$

has a unique solution for the level populations $\boldsymbol{\chi}$.

E.2 The Optically Thin Limit

If a cloud is optically thin, then one may calculate $\boldsymbol{J}$ from the 2.7 K cosmic microwave background and solve equation E.7 directly for $\boldsymbol{\chi}$. If the line profile is expressed in terms of velocity v, then the optical depth is

$$\tau_{ul}(v) = \frac{h\,c\,N_{CO}}{4\pi}\,(\chi_l\,B_{lu} \;-\; \chi_u\,B_{ul})\,\phi(v)\;, \tag{E.8}$$

where the subscript u is for the upper state and l is for the lower.

Since the level populations $\boldsymbol{\chi}$ cannot in general be described by a single excitation temperature, the following source function must be used to compute the brightness temperature. In brightness temperature units,

$$S_{ul} \;=\; \frac{h\,\nu_{ul}}{k_B}\,\left[\frac{g_u\,\chi_l}{g_l\,\chi_u} \;-\; 1\right]^{-1}\;. \tag{E.9}$$

Finally, the antenna temperature can be calculated from the source function S, the optical depth τ, and the brightness temperature of the background T_B.

$$T_A \;=\; T_B\,e^{-\tau} \;+\; S\,\left(1 \;-\; e^{-\tau}\right)\;. \tag{E.10}$$

E.3 When the Optically Thin Limit Doesn't Apply

If the cloud is not optically thin, then I_ν must be known in all directions inside the cloud to use equation E.2 to compute $\boldsymbol{J}$ before equation E.7 can be solved for $\boldsymbol{\chi}$. This poses some difficulty, requiring knowledge of the detailed geometry of the cloud.

The intensity I_ν in a given direction can be computed by integrating the source function through the cloud:

$$I_\nu(\Omega) \;=\; \int_0^{\tau_\nu} e^{-\tau}\, S_\nu(\Omega,\tau)\, d\tau \;. \tag{E.11}$$

Assume azimuthal symmetry and insert equation E.11 into equation E.2:

$$J \;=\; \frac{1}{2}\int_{-1}^{1} d\,cos(\theta) \int_0^{\infty} d\nu\, \phi(\nu) \int_0^{\tau_\nu} e^{-\tau}\, S_\nu(\Omega,\tau)\, d\tau \;. \tag{E.12}$$

If the cloud is optically thick, S_ν is roughly independent of position and can be taken outside the integral. Solving the integral over $d\tau$ gives

$$J \;=\; S_\nu \left[1 \;-\; \frac{1}{2}\int_{-1}^{1} d\,cos(\theta) \int_0^{\infty} d\nu\, \phi(\nu)\, e^{-\tau_\nu}\right] \;. \tag{E.13}$$

The details of the cloud geometry can now be encapsulated in a new variable called β,

$$\beta \;\equiv\; \frac{1}{2}\int_{-1}^{1} d\,cos(\theta) \int_0^{\infty} d\nu\, \phi(\nu)\, e^{-\tau_\nu} \;, \tag{E.14}$$

which can then be used to write J:

$$J \;=\; S_\nu \;[1 \;-\; \beta] \;. \tag{E.15}$$

Note that since $\tau > 0$ and $\phi(\nu)$ is normalized, then

$$0 \;<\; \beta \;<\; 1 \;. \tag{E.16}$$

Inserting equation E.15 into equation E.4 allows the rate equation to be expressed in terms of β. After much simplifying,

$$\chi_{j+1}\, A_{j+1,j}\, \beta_{j+1,j} \;-\; \chi_j\, A_{j,j-1}\, \beta_{j,j-1} \;+\; \sum_i \chi_i\, C_{ij} \;-\; \chi_j \sum_k C_{jk} \;=\; 0\,. \qquad \text{(E.17)}$$

Like equation E.4, equation E.17 can be expressed as a matrix relation, where the matrix will also be singular with a one-dimensional null space equivalent to row degeneracy. This can be fixed as before by replacing the last row of the matrix equation with the normalization relation. Once again, $b_j \equiv \delta_{j,N-1}$ and

$$\mathcal{F}(\boldsymbol{\beta}, T_{kin}) \cdot \boldsymbol{\chi} \;=\; \boldsymbol{b}\,. \qquad \text{(E.18)}$$

E.4 Photon Trapping

Comparing equations E.4, E.16, and E.17, it can be seen that expressing $\boldsymbol{J}$ in terms of $\boldsymbol{\beta}$ recovers the equivalent of the rate equation for $J = 0$ (the optically thin limit), except now the A coefficients are reduced by the factor β. If a cloud is optically thick in transition $J \rightarrow J-1$, then when a CO molecule in state J emits a photon, the photon will probably be reabsorbed by some other molecule in state J-1 elsewhere in the cloud. There is no net change in the level populations of the cloud when this happens. Only when a photon escapes from the cloud is there a net change in the level populations. Thus the emission process effectively gets slowed down by the number of bounces it takes a photon to escape. For this reason, β is an "escape probability," and the reabsorbed photon is referred to as "trapped."

E.5 The Large Velocity Gradient Approximation

The spectral line width of a molecular cloud is typically about an order of magnitude larger than the expected thermal line width for characteristic temperatures associated with the cloud, i.e., kilometers per second compared to hundreds of meters per second.

If this velocity width is due to large-scale motion rather than small-scale turbulence, then because of Doppler shift, a molecule in the cloud can only "see" other molecules that are relatively near by. In this limit, calculation of β with equation E.14 becomes a local and thus substantially more tractable problem.

Goldreich and Kwan (1974) calculate β in this large velocity gradient (LVG) approximation for "a uniform-density, pressure-free sphere which has collapsed from infinite radius...." The infall velocity is proportional to the distance r from the cloud center,

$$v(r) = r \times \left(\frac{2\,G\,M}{R^3} \right)^{\frac{1}{2}} , \tag{E.19}$$

where M is the mass of the cloud and R is its radius. The escape probability for this model is

$$\beta \;=\; \frac{1 \,-\, e^{-\tau}}{\tau} \,. \tag{E.20}$$

Scoville and Solomon (1974) calculate β for a plane-parallel geometry where the velocity gradient is along the line of sight. As long as dv/dz doesn't change sign,

$$\beta \;=\; \frac{1 \,-\, e^{-3\,\tau}}{3\,\tau} \,. \tag{E.21}$$

E.6 A Fast Newton's Method LVG Solver

To find the antenna temperatures and optical depths of a cloud, first equation E.18 must be solved for $\boldsymbol{\chi}$. Then $\boldsymbol{\chi}$ is used in equations E.8, E.9, and E.10 to find the antenna temperatures and optical depths. Unfortunately, since the escape function β is a nonlinear function of the level populations $\boldsymbol{\chi}$, equation E.18 cannot be solved analytically. One can, however, approximate β with a Taylor expansion about a reasonable guess for $\boldsymbol{\chi}$.

Given $\boldsymbol{\chi}$ which is close to the solution, we can find $\delta\boldsymbol{\chi}$ such that $(\boldsymbol{\chi} + \delta\boldsymbol{\chi})$ is the solution to first order. Given an adequate initial guess, this technique can be iterated

as many times as necessary to converge upon the true value of $\boldsymbol{\chi}$. First, write the first-order Taylor expansion of the escape function:

$$\beta_{ul}(\boldsymbol{\chi} + \delta\boldsymbol{\chi}) \approx \beta_{ul}(\boldsymbol{\chi}) + \frac{\partial\beta_{ul}}{\partial\chi_l}(\boldsymbol{\chi})\,\delta\chi_l + \frac{\partial\beta_{ul}}{\partial\chi_u}(\boldsymbol{\chi})\,\delta\chi_u\,. \tag{E.22}$$

Since for linear molecules the only non-zero Einstein A coefficients are for $\Delta J = 1$, the notation can be simplified by dropping the second subscript. The notation can be further simplified by defining new variables to represent partial derivatives of the escape functions calculated at the initial value of $\boldsymbol{\chi}$:

$$\alpha_j \equiv \frac{\partial\beta_{j,j-1}}{\partial\chi_{j-1}} \quad \text{and} \quad \eta_j \equiv \frac{\partial\beta_{j,j-1}}{\partial\chi_j}\,. \tag{E.23}$$

Then

$$\beta_{ul}(\boldsymbol{\chi} + \delta\boldsymbol{\chi}) \approx \beta_u + \alpha_u\,\delta\chi_l + \eta_u\,\delta\chi_u\,. \tag{E.24}$$

Substitute this approximation for β into equation E.17 and replace χ_i everywhere with $\chi_i + \delta\chi_i$. Simplifying the result and throwing away terms higher than first order in $\delta\boldsymbol{\chi}$ gives

$$\begin{aligned}(\chi_{j+1} + \delta\chi_{j+1})\,A_{j+1}\,\beta_{j+1} - (\chi_j + \delta\chi_j)\left(A_j\,\beta_j + \sum_k C_{jk}\right) + \sum_i(\chi_i + \delta\chi_i)\,C_{ij} \\ + \chi_{j+1}\,A_{j+1}\,(\alpha_{j+1}\,\delta\chi_j + \eta_{j+1}\,\delta\chi_{j+1}) - \chi_j\,A_j\,(\alpha_j\,\delta\chi_{j-1} + \eta_j\,\delta\chi_j) = 0\,.\end{aligned} \tag{E.25}$$

The first line of equation E.25 is immediately recognized as the LHS of equation E.17, except χ_i has become $\chi_i + \delta\chi_i$. This first line then corresponds to the vector from the LHS of equation E.18:

$$\mathcal{F}(\boldsymbol{\beta}, T_{kin}) \cdot (\boldsymbol{\chi} + \delta\boldsymbol{\chi})\,. \tag{E.26}$$

The second line of equation E.25 is also equivalent to a vector defined by a matrix

multiplication:

$$\mathcal{G}\left(\boldsymbol{\chi}, \boldsymbol{\alpha}, \boldsymbol{\eta}\right) \cdot \delta\boldsymbol{\chi} \tag{E.27}$$

where $\mathcal{G}$ is a tri-diagonal matrix.

We can now rewrite equation E.25 in terms of $\mathcal{F}$ and $\mathcal{G}$:

$$\left(\mathcal{F} + \mathcal{G}\right) \cdot \delta\boldsymbol{\chi} = -\mathcal{F} \cdot \boldsymbol{\chi} \, . \tag{E.28}$$

Before solving equation E.28 for $\boldsymbol{\chi}$, note that $(\mathcal{F} + \mathcal{G})$ is still row degenerate. To preserve normalization of $\boldsymbol{\chi}$,

$$\sum_j \delta\chi_j = 0 \, . \tag{E.29}$$

Equation E.29 can be incorporated into equation E.28 by replacing the last row of $\mathcal{F}$ with 0s, and the last row of $\mathcal{G}$ with 1s.

To use equation E.28, first guess a reasonable starting value for $\boldsymbol{\chi}$. Use this value to calculate $\boldsymbol{\tau}$, $\boldsymbol{\beta}$, $\boldsymbol{\alpha}$, $\boldsymbol{\eta}$, $\mathcal{F}$, and $\mathcal{G}$. Solve equation E.28 for $\delta\boldsymbol{\chi}$. Add $\delta\boldsymbol{\chi}$ to $\boldsymbol{\chi}$ and iterate until $\boldsymbol{\chi}$ converges.

A good starting value for $\boldsymbol{\chi}$ for optically thick clouds with high H_2 densities is to assume that the level populations are thermalized at T_{kin}. This guess may not be adequate for lower H_2 densities if the gas becomes sub-critically excited. If the solver initially fails to converge, the H_2 density is increased until it converges. Then the density is gradually lowered back to the desired value, using the final value of $\boldsymbol{\chi}$ at the end of each step as the initial value for the next.

E.7 Example Solutions

Results from the LVG solver calculated with Goldreich & Kwan's spherical cloud model are shown in Figure E.1 and with Scoville & Solomon's plane-parallel model in Figure E.2. Collision rate constants for excitation of CO by para H_2 were taken from

Flower and Launay (1985) and scaled up by 21% to account for excitation by He. We see that at low column densities the results are the same for both models. This is because the escape function β approaches unity (i.e., becomes unimportant) for optically thin clouds. At high column densities and high H_2 density, the results are also the same for both models since in this limit the lines are optically thick and the level populations of the CO become thermalized. The details of the escape function thus become most important at high column densities and low H_2 densities, where the CO is sub-critically excited but not optically thin. In this regime, for a given measured J=6→5 / J=2→1 line ratio, the plane-parallel model will predict lower densities than the spherical model by a factor of a few.

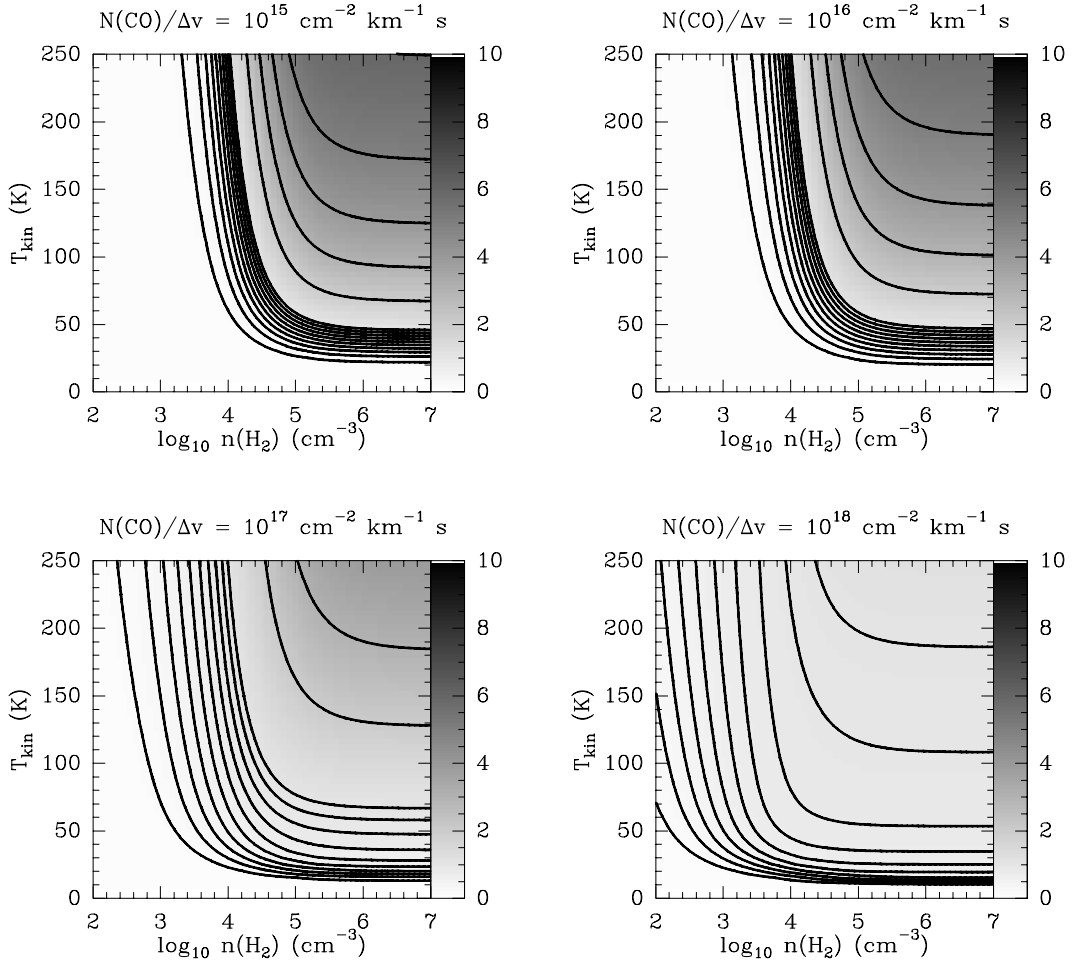

Figure E.1 LVG calculation of the ^{12}CO J=6→5 / ^{12}CO J=2→1 line ratio using β calculated for Goldreich & Kwan's spherical cloud model. Contours are from 0.1 to 1 in steps of 0.1, then integer valued.

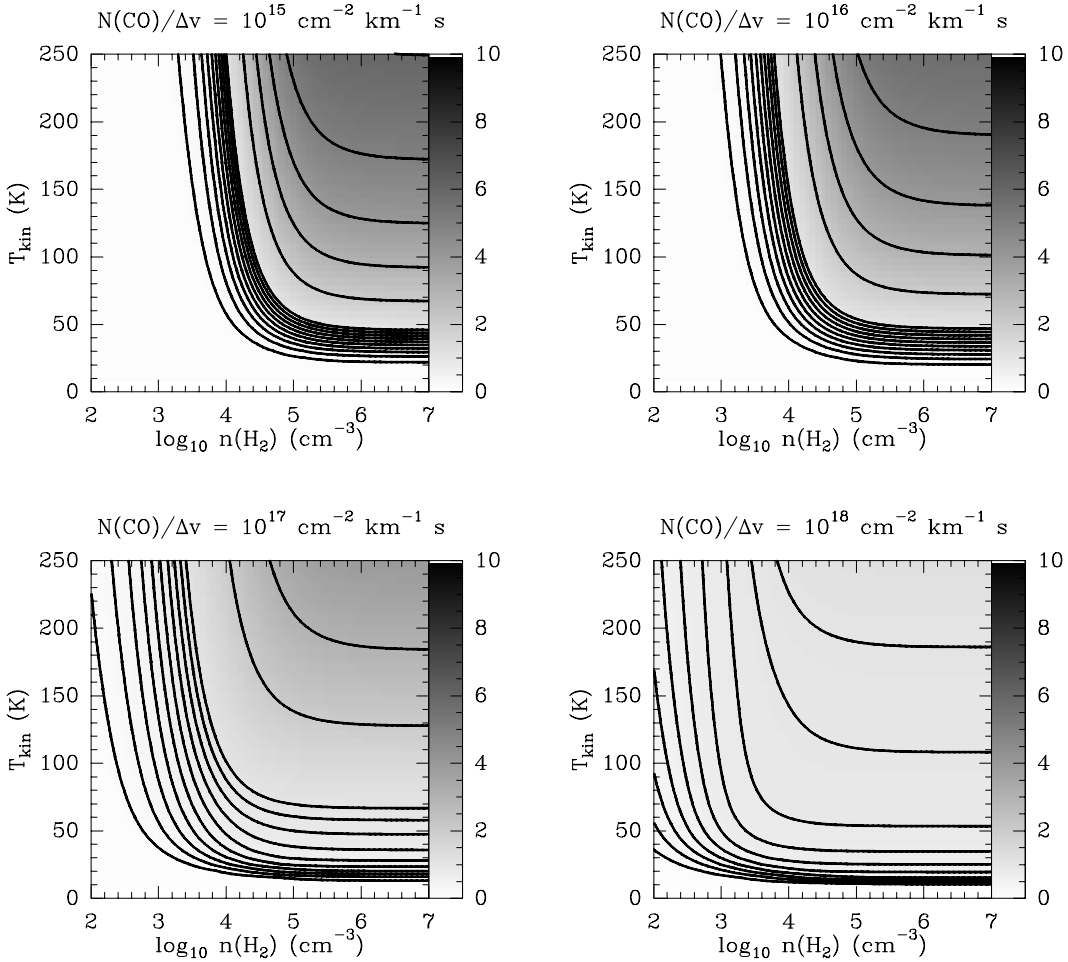

Figure E.2 LVG calculation of the ^{12}CO J=6→5 / ^{12}CO J=2→1 line ratio using β calculated for Scoville & Solomon's plane-parallel cloud model. Contours are from 0.1 to 1 in steps of 0.1, then integer valued.

Appendix F

SuperMix Amplifier Simulation

The following source code and output constitute the final, complete simulation of the 4–8 GHz QMMIC amplifier. Although initial simulations of the amplifier were performed entirely within SuperMix, the final simulation presented here imports scattering matrices calculated with Agilent's Momentum field simulator (Agilent Technologies) for many of the components. These matrices are read from files in the Touchstone format and interpolated as functions of frequency by the SuperMix class `sdata_interp`.

F.1 Source Code

```
#include "supermix.h"
#include "sdata_interp.h"
#include "wardhemt.h"

// Create a new device to have a JPL 160 um transistor with four ports.
// The ports are, as follows:
// Port 1:  Input
// Port 2:  Output
// Port 3:  Source
// Port 4:  Source
class fet_with_source : public data_ptr_nport
{
public:
  fet_with_source()
  {
    br = branch(4);

    fetckt.add_port(st1, 3);
    fetckt.add_port(st2, 3);
    fetckt.add_port(br, 3);
    fetckt.add_port(br, 4);

    fetckt.connect(st1, 1, trans, 1);
    fetckt.connect(trans, 2, st2, 1);
    fetckt.connect(st1, 2, br, 1);
    fetckt.connect(st2, 2, br, 2);
```

```
  }

  int size() { return 4; }

private:
  circuit fetckt;
  jpltrw160_bump_5mA_500mV trans;
  series_tee st1, st2;
  branch br;

  void recalc() { data_ptr = &fetckt.get_data(); }

};


int main(void) {

  // A circuit to hold the assembled components.
  circuit intamp;

  // Transistors, one per stage.
  fet_with_source t1, t2, t3;

  // Gate tuning and bias components (one each for 3 stages)
  branch bg1, bg2, bg3; // Gate bias line connects with a branch.
  sdata_interp rg1, rg2, rg3; // 1 K gate bias resistors.
  sdata_interp gsc1a, gsc2a, gsc3a;
  resistor g50ohm1, g50ohm2, g50ohm3;
  sdata_interp gsc1b, gsc2b, gsc3b;
  open_term got1, got2, got3; // This is where the bias is connected.
  sdata_interp spiral1, spiral2, spiral3;

  // Drain tuning and bias components (one each for 3 stages)
  sdata_interp ld1, ld2, ld3;
  sdata_interp rd1, rd2, rd3;
  branch bd1, bd2, bd3; // Drain bias line connects with a branch.
  sdata_interp dsc1a, dsc2a, dsc3a; // Shorts drain bias resistors to ground.
  resistor d50ohm1, d50ohm2, d50ohm3;
  sdata_interp dsc1b, dsc2b, dsc3b; // Shorts drain bias resistors to ground.
  open_term dot1, dot2, dot3; // This is where the bias is connected.
  sdata_interp dcblock2, dcblock3, dcblock4, dcblock5;

  inductor in_bond, out_bond;
  in_bond.L = 0.25 * Nano * Henry;
  out_bond.L = 0.25 * Nano * Henry;

  // Set up input and output cpw lines.
  const_diel gaas;
  gaas.eps.set(12.9);
  gaas.tand.set(0.);
  // Set up gold film, conductivity for 295 K, from Kittel page 144
  normal_film copper;
  copper.Thick = 0.5 * Micron;
```

```
copper.rho = 2.2 * Micro * Ohm * Centi * Meter;
// Make the cpw lines
cpw in_cpw, out_cpw;
in_cpw.top_strip(copper);
in_cpw.substrate(gaas);
in_cpw.bottom_plane(copper);
in_cpw.sub_thick.set(250.*Micron);
in_cpw.length.set(100.*Micron);
in_cpw.width.set(80.*Micron);
in_cpw.space.set(61.9*Micron);
out_cpw = in_cpw;

resistor rpad1, rpad2;
rpad2.parallel();
rpad1.R = 30. * Ohm;
rpad2.R = 200. * Ohm;

sdata_interp sterm1(1), sterm2(1), sterm3(1), sterm4(1), sterm5(1), sterm6(1);
sterm1.touchstone("Lsource_270x10_250um_4k.s1p");
sterm2.touchstone("Lsource_270x10_250um_4k.s1p");
sterm3.touchstone("Lsource_270x10_250um_4k.s1p");
sterm4.touchstone("Lsource_270x10_250um_4k.s1p");
sterm5.touchstone("Lsource_270x10_250um_4k.s1p");
sterm6.touchstone("Lsource_270x10_250um_4k.s1p");

// Set initial values for amplifier components.
rg1.touchstone("res_1k_241x12_250um_4k.s2p");
rg2.touchstone("res_1k_241x12_250um_4k.s2p");
rg3.touchstone("res_1k_241x12_250um_4k.s2p");
gsc1a.touchstone("cap_200x200_250um_4k_parallel.s2p");
gsc2a.touchstone("cap_200x200_250um_4k_parallel.s2p");
gsc3a.touchstone("cap_200x200_250um_4k_parallel.s2p");
dsc1a.touchstone("cap_340x300_250um_4k_parallel.s2p");
dsc2a.touchstone("cap_300x439_250um_4k_parallel.s2p");
dsc3a.touchstone("cap_320x420_250um_4k_parallel.s2p");
g50ohm1.R = 50. * Ohm;
g50ohm2.R = 50. * Ohm;
g50ohm3.R = 50. * Ohm;
d50ohm1.R = 50. * Ohm;
d50ohm2.R = 50. * Ohm;
d50ohm3.R = 50. * Ohm;
gsc1b.touchstone("cap_300x300_250um_4k_parallel.s2p");
gsc2b.touchstone("cap_300x300_250um_4k_parallel.s2p");
gsc3b.touchstone("cap_300x300_250um_4k_parallel.s2p");
dsc1b.touchstone("cap_300x300_250um_4k_parallel.s2p");
dsc2b.touchstone("cap_300x300_250um_4k_parallel.s2p");
dsc3b.touchstone("cap_300x300_250um_4k_parallel.s2p");
spiral1.touchstone("spiral6_5_250um_4k.s2p");
spiral2.touchstone("spiral4_5_250um_4k.s2p");
spiral3.touchstone("spiral3_5_250um_4k.s2p");
ld1.touchstone("drainline_240x5_250um_4k.s2p");
ld2.touchstone("drainline_240x5_250um_4k.s2p");
ld3.touchstone("drainline_240x5_250um_4k.s2p");
```

```
rd1.touchstone("res_150_259x86_250um_4k.s2p");
rd2.touchstone("res_43_136x117_250um_4k.s2p");
rd3.touchstone("res_68_117x86_250um_4k.s2p");
dcblock2.touchstone("cap_10pF_250um_4k.s2p");
dcblock3.touchstone("cap_10pF_250um_4k.s2p");
dcblock4.touchstone("cap_10pF_250um_4k.s2p");
dcblock5.touchstone("cap_10pF_250um_4k.s2p");

// Specify the input port.
intamp.add_port(in_bond, 1);

// Assemble the amplifier.
intamp.connect(in_bond, 2, in_cpw, 1);
intamp.connect(in_cpw, 2, dcblock2, 1);
intamp.connect(dcblock2, 2, bg1, 1);

intamp.connect(bg1, 3, rg1, 1);
intamp.connect(rg1, 2, gsc1a, 1);
intamp.connect(gsc1a, 2, g50ohm1, 1);
intamp.connect(g50ohm1, 2, gsc1b, 1);
intamp.connect(gsc1b, 2, got1, 1);

intamp.connect(bg1, 2, spiral1, 1);
intamp.connect(spiral1, 2, t1, 1);
intamp.connect(t1, 3, sterm1, 1);
intamp.connect(t1, 4, sterm2, 1);
intamp.connect(t1, 2, ld1, 1);
intamp.connect(ld1, 2, bd1, 1);

intamp.connect(bd1, 3, rd1, 1);
intamp.connect(rd1, 2, dsc1a, 1);
intamp.connect(dsc1a, 2, d50ohm1, 1);
intamp.connect(d50ohm1, 2, dsc1b, 1);
intamp.connect(dsc1b, 2, dot1, 1);

intamp.connect(bd1, 2, dcblock3, 1);
intamp.connect(dcblock3, 2, bg2, 1);

intamp.connect(bg2, 3, rg2, 1);
intamp.connect(rg2, 2, gsc2a, 1);
intamp.connect(gsc2a, 2, g50ohm2, 1);
intamp.connect(g50ohm2, 2, gsc2b, 1);
intamp.connect(gsc2b, 2, got2, 1);

intamp.connect(bg2, 2, spiral2, 1);
intamp.connect(spiral2, 2, t2, 1);
intamp.connect(t2, 3, sterm3, 1);
intamp.connect(t2, 4, sterm4, 1);
intamp.connect(t2, 2, ld2, 1);
intamp.connect(ld2, 2, bd2, 1);

intamp.connect(bd2, 3, rd2, 1);
intamp.connect(rd2, 2, dsc2a, 1);
```

```
intamp.connect(dsc2a, 2, d50ohm2, 1);
intamp.connect(d50ohm2, 2, dsc2b, 1);
intamp.connect(dsc2b, 2, dot2, 1);

intamp.connect(bd2, 2, dcblock4, 1);
intamp.connect(dcblock4, 2, bg3, 1);

intamp.connect(bg3, 3, rg3, 1);
intamp.connect(rg3, 2, gsc3a, 1);
intamp.connect(gsc3a, 2, g50ohm3, 1);
intamp.connect(g50ohm3, 2, gsc3b, 1);
intamp.connect(gsc3b, 2, got3, 1);

intamp.connect(bg3, 2, spiral3, 1);
intamp.connect(spiral3, 2, t3, 1);
intamp.connect(t3, 3, sterm5, 1);
intamp.connect(t3, 4, sterm6, 1);
intamp.connect(t3, 2, ld3, 1);
intamp.connect(ld3, 2, bd3, 1);

intamp.connect(bd3, 3, rd3, 1);
intamp.connect(rd3, 2, dsc3a, 1);
intamp.connect(dsc3a, 2, d50ohm3, 1);
intamp.connect(d50ohm3, 2, dsc3b, 1);
intamp.connect(dsc3b, 2, dot3, 1);

intamp.connect(bd3, 2, dcblock5, 1);
intamp.connect(dcblock5, 2, rpad1, 1);
intamp.connect(rpad1, 2, rpad2, 1);
intamp.connect(rpad2, 2, out_cpw, 1);
intamp.connect(out_cpw, 2, out_bond, 1);

// Specify the output port.
intamp.add_port(out_bond, 2);

// Set the global temperature to liquid He.
device::T = 4.2 * Kelvin;

complex::out_degree();
cout << fixed << right;

cout << "  Freq   S21(dB)    S11(dB)  S22(dB)     Tn(K)"
     << "   |delta|         K" << endl << endl;
ampdata sd;
for(double freq = 4.0; freq <=8.1; freq += 0.5)
{
  device::f = freq * GHz;
  sd = intamp.get_data();
  cout << setw(6) << setprecision(3)
       << freq << "  " << setw(8)
       << sd.SdB(2,1) << "  " << setw(8)
       << sd.SdB(1,1) << "  " << setw(8)
       << sd.SdB(2,2) << "  " << setw(8)
```

```
        << sd.tn(2,1)/Kelvin << "  " << setw(8)
        << zabs(sd.delta()) << "  " << setw(8)
        << sd.k();
    if(sd.unconditionally_stable()) cout << "  Stable";
    cout << endl;
  }
}
```

F.2 Output

Freq	S21(dB)	S11(dB)	S22(dB)	Tn(K)	|delta|	K	
4.000	31.216	-8.073	-29.732	5.023	0.015	119.857	Stable
4.500	31.405	-10.584	-31.659	4.338	0.013	85.332	Stable
5.000	31.618	-14.159	-35.643	3.726	0.011	60.998	Stable
5.500	31.835	-20.751	-44.166	3.231	0.011	43.830	Stable
6.000	32.010	-28.988	-35.972	2.900	0.016	31.764	Stable
6.500	32.081	-16.225	-30.445	2.784	0.023	23.298	Stable
7.000	32.011	-10.924	-28.984	2.942	0.026	17.277	Stable
7.500	31.777	-7.620	-33.315	3.437	0.026	12.892	Stable
8.000	31.264	-5.174	-32.071	4.348	0.048	9.718	Stable

Appendix G

SuperMix Receiver Simulation

The following program uses the SuperMix library to calculate the entire 690 GHz receiver, from the beam splitter to the output of the IF LNA. Total system gain, including optics loss, mixer conversion loss, and IF amplifier gain, is calculated for each sideband, as is the total SSB noise temperature. The amplifier gain and noise are calculated by a different SuperMix program (presented in Appendix F) and read from a file in the Touchstone format.

G.1 Mixer Chip Definition

The include file defines the SIS mixer as `class mixer`. Noise and loss from the optics are simulated with attenuators at the appropriate temperatures.

```
// mixer72.h
// Builds 72 device from batch 970218.01
//
// Mixer can be used by creating a device of type mixer72.
//
// WARNING: Some parameters are used only at creation.  Changing them
// later may have no effect.
//
// A 2-port IF circuit must be passed as a parameter to the constructor.
// This circuit should include all wire bonds from the chip, DC blocking
// capacitors, any IF matching circuitry, and the IF amplifier.  In other
// words, all IF circuitry not already on the mixer chip.
//
// The mixer is built up into several compenents:
//    left and right radial stubs
//    IF output line
//    left and right RF tuning circuits
//    transmission line between the junctions
//    twin-slot antenna
//    lossy optics
//
// These pieces are then connected into RF and IF circuits.  The antenna
```

```
// is a short circuit at low frequencies, and so is left out of the IF
// circuit.  The output of the IF output line is assumed to be open at
// the RF frequency.
//
// Finally, the RF circuit, IF circuit, and junctions are assembled into
// a mixer.
//

#include "supermix.h"

class mixer72: public nport
{
public:

  // Various parameters for the mixer.
  parameter Rn; // Normal state resistance.
  parameter Cap; // Capacitance of the junction.
  parameter Vn; // Normalization voltage for IV curve
  parameter Vbias; // Bias voltage
  int harmonics; // Number of harmonics being used
  parameter LO_freq;
  parameter LO_power;
  parameter diel_thick1; // Dielectric thickness (about 4500 A)
  parameter diel_thick2; // Dielectric thickness (about 2500 A)

  // Components for the antenna
  // The impedance of the twin-slot antenna is read from a touchstone file
  sdata_interp z_ant;
  twin_slot_antenna antenna;

  // Metal films and dielectrics
  super_film nb; // Niobium film.
  super_film nbtin; // NbTiN film.
  const_diel vacuum;
  const_diel sio;
  const_diel si;

  // RF tuning circuit elements between the stubs
  microstrip ms1; // Tuning microstrips from slot to SIS junction.
  microstrip ms2;
  microstrip ms3;
  branch junction_br; // Use a branch to connect to the junction.
  circuit left_ckt; // Build half of RF matching network
  circuit right_ckt; // Then copy it to make the other half

  // Tuning microstrip between SIS junctions.
  microstrip ltune;

  // Radial stubs, and open circuit terminator for the right stub.
  radial_stub left_stub;
  radial_stub right_stub;
  open_term open_stub_end;
```

```
// IF transmission line, to be connected to the left stub.
circuit ifline;
microstrip ifline1; // Components of output transmission line.
microstrip ifline2;
microstrip ifline3;
cpw ifline4;

// The IF amplifier
nport *IFmatch;

// Lossy optical elements (simulate losses with attenuators)
circuit optics;
attenuator splitter; // Beam splitter
attenuator window; // Pressure window
attenuator ir_block; // Infared block
attenuator poly_lens; // Plastic lens
attenuator si_lens; // Silicon hyperhemisphere

// The IF and RF circuits
circuit IF; // IF circuit to add to mixer
circuit RF; // RF circuit to add to mixer
open_term open_IF; // Leave the IF port open for the RF circuit

// The actual mixer, fully built.
mixer m;

// SIS junctions, IV curves, and bias circuitry
sis_basic_device j1, j2; // The SIS junctions
ivcurve iv; // The IV curve (read from a file)
circuit bias; // The bias circuit
voltage_source j1_bias,// Voltage bias for SIS junctions
               j2_bias;

// Local oscillator source
generator LO_source;


// Get the data from the mixer, m.
void recalc()
{
  data = m.get_data();
}

// Return the size of the mixer, m.
int size()
{
  return m.size();
}

// Return the total current on the junctions
double current()
{
  return (j1.I().read(0).real + j2.I().read(0).real);
```

```
}

// The constructor builds the mixer.
mixer72(nport & IFcircuit) : z_ant(1),
            IFmatch(&IFcircuit),
            iv("surfer.idc","surfer.ikk")
{
  z_ant.touchstone("Zslot.750");
  antenna.set(z_ant);

  // Define niobium wiring.
  nb.Vgap = 2.9*mVolt;
  nb.Tc = 9.56*Kelvin;
  nb.rho_normal = 5.*Micro*Ohm*Centi*Meter;
  nb.Thick = 3000.*Angstrom;

  // Define NbTiN ground plane.
  nbtin.Vgap = 5.0*mVolt;
  nbtin.Tc = 15.75*Kelvin;
  nbtin.rho_normal = 59.25*Micro*Ohm*Centi*Meter;
  nbtin.Thick = 3000.*Angstrom;

  // Define vacuum dielectric.
  vacuum.eps = 1.0;
  vacuum.tand = 0.0;

  // Define SiO dielectric.
  sio.eps = 5.6; // dielectric constant
  sio.tand = 0.0; // loss tangent

  // Define Si dielectric (used on IF output CPW)
  si.eps = 11.7;
  si.tand = 0.0;

  // Define dielectric thicknesses
  diel_thick1 = 4500.0 * Angstrom;
  diel_thick2 = 2500.0 * Angstrom;

  // Make a microstrip line with Nb wiring, a NbTiN ground plane,
  // vacuum superstrate, and SiO insulator.
  // Later, when a new microstrip is needed, just copy this one.
  ms1.top_strip(nb) ; // Use Nb film for top strip
  ms1.ground_plane(nbtin) ; // Use NbTiN film for ground plane
  ms1.superstrate(vacuum) ; // Nothing above
  ms1.substrate(sio) ; // SiO insulator
  ms1.sub_thick = &diel_thick1 ;  // SiO thickness

  // Create the tuning transmission lines.
  ms1.width = 5.8*Micron ;
  ms1.length = 11.2*Micron ;
  ms1.sub_thick = &diel_thick1;

  ms2 = ms1; // copy microstrip
```

```
ms2.width = 3.3*Micron;
ms2.length = 15.0*Micron;
ms2.sub_thick = &diel_thick1;

ms3 = ms1;
ms3.width = 5.0*Micron ;
ms3.length = 2.5*Micron ;
ms3.sub_thick = &diel_thick2;

// Tuning inductance between the junctions.
// The center is a virtual ground from the symmetry of the circuit.
ltune = ms1;
ltune.width = 5.0*Micron ;
ltune.length = 6.9*Micron ;
ltune.sub_thick = &diel_thick2;

// Now that the individual components of one half of the RF matching
// network are created, connect them into a circuit.  We will then copy
// the circuit to make the right half.
left_ckt.add_port(ms1, 1);
left_ckt.connect(ms1, 2, ms2, 1);
left_ckt.connect(ms2, 2, ms3, 1);
left_ckt.connect(ms3, 2, junction_br, 1);
left_ckt.add_port(junction_br, 2);
left_ckt.add_port(junction_br, 3);
right_ckt = left_ckt;

// Create a radial stub and transmission line feeding it.
// Then copy it to make the other stub.
left_stub.top_strip(nb);
left_stub.ground_plane(nbtin);
left_stub.superstrate(vacuum);
left_stub.substrate(sio);
left_stub.radius = 36. * Micron;
left_stub.angle = 90. * Degree;
left_stub.width = 5.8*Micron ;
left_stub.length = 3.3*Micron ;
left_stub.sub_thick = &diel_thick1;
right_stub = left_stub;

// Create the IF transmission line
ifline1 = ms1;
ifline1.width = 2.0*Micron;
ifline1.length = 37.0*Micron;
ifline2 = ifline1;
ifline2.width = 10.0*Micron;
ifline2.length = 36.0*Micron;
ifline3 = ifline1;
ifline3.width = 5.0*Micron;
ifline3.length = 3.0*Micron;
ifline4.top_strip(nb);
ifline4.substrate(si);
ifline4.sub_thick = 250.*Micron;
```

```
ifline4.width = 5.0*Micron;
ifline4.space = 5.0*Micron;
ifline4.length = 333.0*Micron;
ifline.connect(ifline1, 2, ifline2, 1);
ifline.connect(ifline2, 2, ifline3, 1);
ifline.connect(ifline3, 2, ifline4, 1);
ifline.add_port(ifline1, 1);
ifline.add_port(ifline4, 2);

// Account for optics losses before twin slot
splitter.Temp = 300. * Kelvin;
splitter.dB = 0.7; // 1 mil mylar (25 microns) n=1.75
window.Temp = 300. * Kelvin;
window.dB = 0.22;
ir_block.Temp = 77. * Kelvin;
ir_block.dB = 0.22;
poly_lens.dB = 0.4; // 2 surfaces, n=1.55
si_lens.dB = 0.5;
optics.connect(splitter, 2, window, 1);
optics.connect(window, 2, ir_block, 1);
optics.connect(ir_block, 2, poly_lens, 1);
optics.connect(poly_lens, 2, si_lens, 1);
optics.add_port(splitter, 1);
optics.add_port(si_lens, 2);

// Assemble the IF circuit
// IF circuit must have SIS junctions on ports one and two.
// The IF signal comes out of port 3.
IF.add_port(left_ckt, 3); // Left SIS
IF.add_port(right_ckt, 3); // Right SIS
IF.add_port(*IFmatch, 2); // Output of IF output circuit
IF.connect(ifline, 2, *IFmatch, 1);
IF.connect(ifline, 1, left_stub, 2);
IF.connect(left_stub, 1, left_ckt, 1);
IF.connect(left_ckt, 2, ltune, 1);
IF.connect(ltune, 2, right_ckt, 2);
IF.connect(right_ckt, 1, right_stub, 1);
IF.connect(right_stub, 2, open_stub_end, 1);

// Assemble the RF circuit
// RF circuit must have SIS junctions on ports one and two.
// The RF and LO couple into the dewar on port 3.
RF.add_port(left_ckt, 3); // Left SIS
RF.add_port(right_ckt, 3); // Right SIS
RF.add_port(optics, 1); // RF and LO input
RF.connect(open_IF, 1, ifline, 2); // Terminate IF line.
RF.connect(ifline, 1, left_stub, 2);
RF.connect(left_stub, 1, antenna, 2);
RF.connect(antenna, 3, left_ckt, 1);
RF.connect(left_ckt, 2, ltune, 1);
RF.connect(ltune, 2, right_ckt, 2);
RF.connect(right_ckt, 1, antenna, 4);
RF.connect(antenna, 5, right_stub, 1);
```

```
    RF.connect(right_stub, 2, open_stub_end, 1);
    RF.connect(antenna, 1, optics, 2);

    // Junction resistance is nominally 20 Ohm / sq micron
    // But guess that RnA = 21.8 Ohm / sq micron from measured 51 device
    // So expect 15.1 Ohms for a (1.2 * 1.2) sq micron junction
    // Use Rn measured from IV curve.
    Rn = 16.6*Ohm;

    // Junction capacitance, 82 fF/sq micron, * (1.3)^2  sq microns = 185 fF
    // but guess 0.1 micron undercut, so 118 fF
    Cap = 120.*fFarad;

    // The normalization voltage used in the IV curve file
    Vn = 2.85*mVolt;

    harmonics = 1;

    j1.set_iv(iv);
    j1.Rn = &Rn;
    j1.Vn = &Vn;
    j1.Cap = &Cap;

    j2.set_iv(iv);
    j2.Rn = &Rn;
    j2.Vn = &Vn;
    j2.Cap = &Cap;

    j1_bias.source_voltage = &Vbias;
    j2_bias.source_voltage = &Vbias;

    bias.add_port(j1_bias, 1);
    bias.add_port(j2_bias, 1);

    // Give the mixer a local oscillator:
    LO_source.source_f = &LO_freq;
    LO_source.source_width = 1*MHz;
    LO_source.source_power = &LO_power;
    LO_source.Temp = 0.0;
    m.LO = &LO_freq;
    m.harmonics(harmonics);

    // now connect both junctions and voltage bias sources to the mixer:
    m.add_junction(j1);
    m.add_junction(j2);
    m.set_bias(bias);

    // Set the RF and IF circuits
    m.set_if(IF);
    m.set_rf(RF);
    m.set_balance_terminator(LO_source, 3);
  }
};
```

G.2 Receiver Source Code

The SIS mixer definition is read from the include file. DC blocking capacitors and wire bonds are added. A TMM10 microstrip circuit transforms the IF impedance to 50 Ω. An isolator is simulated as a lossy circulator, and followed by the IF amplifier read from a Touchstone file. Note that the complete receiver, including the IF circuit, is included in the harmonic balance calculation.

```
#include "mixer72.h"

int main(int argc, char** argv)
{
  error::messages = 1;

  // Set default temperature and impedance.
  device::T = 4.2*Kelvin;
  device::Z0 = 50.*Ohm;
  device::f = 6.0*GHz; // IF frequency

  // Build the IF circuit, including wire bonds, IF matching circuit,
  // and low-noise amplifier.
  circuit IF_circuit;

  // Components needed to simulate the mixer
  capacitor dcblock_sig, dcblock_gnd;
  inductor lbond_sig, lbond_gnd;
  series_tee st;
  short_term shrt;

  // The chip is connected through wire bonds and blocking
  // capacitors.  Conservatively assume wire bond lengths of
  // 1.2 mm.  (It may be possible to shorten them slightly.)
  // The wire bonds are connected in pairs to reduce the
  // inductance.  Assume 1 pair has an inductance of 0.4 nH/mm.
  // Thus, for our case that will be .48 nH / pair.

  // The signal is connected through one pair of wire bonds
  lbond_sig.L = 0.48 * Nano * Henry;
  dcblock_sig.C = 10. * Pico * Farad;

  // The ground has two pairs of wire bonds.
  // Each pair goes to a 10 pF capacitor.
  // Add impediances into an equivalent single bond and capacitor.
  lbond_gnd.L = 0.24 * Nano * Henry;
  dcblock_gnd.C = 20. * Pico * Farad;

  // Create microstrip on TMM10

  const double Mil = 25.4 * Micro * Meter;
```

```
// Define 1/2 ounce copper plate.
normal_film copper;
copper.Thick = 17.5 * Micro * Meter;

// 10 * conductivity for 295 K, from Kittel page 144
copper.rho = 0.17 * Micro * Ohm * Centi * Meter;

// Define vacuum dielectric.
const_diel vacuum;
vacuum.eps = 1.0;
vacuum.tand = 0.0;

// Define TMM10 dielectric.
const_diel tmm10;
tmm10.eps = 9.8;        // dielectric constant
tmm10.tand = 0.0;       // loss tangent

// The matching microstrip
microstrip trl1, trl2;
trl1.top_strip(copper);
trl1.ground_plane(copper);
trl1.superstrate(vacuum);
trl1.substrate(tmm10);
trl1.sub_thick = 25. * Mil;
trl1.width = 144.0 * Mil;
trl1.length = 332.0 * Mil;

trl2 = trl1;
trl2.width = 54.8 * Mil;
trl2.length = 183.1 * Mil;

// Add the IF amplifier, along with an isolator and some loss.
circulator circ;
zterm circ_term;
attenuator circ_loss;
sdata_interp lna;

circ_term.Z = 50. * Ohm;
circ_loss.dB = 1.0;
lna.touchstone("lna-jsw-b.s2p");

IF_circuit.connect(shrt, 1, dcblock_gnd, 1);
IF_circuit.connect(dcblock_gnd, 2, lbond_gnd, 1);

IF_circuit.connect(st, 2, lbond_gnd, 2);

IF_circuit.connect(st, 3, lbond_sig, 1);
IF_circuit.connect(lbond_sig, 2, dcblock_sig, 1);

// Connect the IF matching network
IF_circuit.connect(dcblock_sig, 2, trl1, 1);
IF_circuit.connect(trl1, 2, trl2, 1);
```

```
// Add the isolator and LNA
IF_circuit.connect(trl2, 2, circ, 1);
IF_circuit.connect(circ, 3, circ_term, 1);
IF_circuit.connect(circ, 2, circ_loss, 1);
IF_circuit.connect(circ_loss, 2, lna, 1);

// Specify the input and output ports.
IF_circuit.add_port(st, 1);
IF_circuit.add_port(lna, 2);

// Create a 72 mixer
mixer72 mix(IF_circuit);

real_interp power(mix.LO_freq, "lo_power.dat", GHz, Nano*Watt);
mix.LO_power = &power;

mix.Vbias = 2.15*mVolt;
mix.LO_freq = 680.0*GHz;

// Find the IF port
int if_port = mix.m.port(3, 0);   // port 3 of harmonic 0 (IF)
int usb_port = mix.m.port(3, 1);  // port 3 of harmonic 1 (USB)
int lsb_port = mix.m.port(3, -1);  // port 3 of harmonic -1 (LSB)

mix.m.initialize_operating_state();
if(mix.m.balance())
  error::warning("Mixer balance failed!");

double LO;
double IF;
sdata sd;
double Phot, Pcold, Pnoise, Thot, Tcold, Y;
Thot = 295. * Kelvin;
Tcold = 77. * Kelvin;
double tn_usb, tn_lsb, tn_dsb;

cout << setprecision(3) << showpoint;
cout << setw(3)
     << "LO"
     << setw(7)
     << "IF"
     << setw(10)
     << "Idc(uA)"
     << setw(10)
     << "Gusb(dB)"
     << setw(10)
     << "Glsb(dB)"
     << setw(9)
     << "Tusb(K)"
     << setw(9)
     << "Tlsb(K)"
     << setw(9)
```

```
      << "Tdsb(K)"
      << endl;

  for(LO=600.0*GHz; LO<=701.0*GHz; LO+=10.0*GHz)
  {
    mix.LO_freq = LO;
    if(mix.m.balance())
      error::warning("Mixer balance failed!");

    for(IF=4.0 * GHz; IF<= 8.1*GHz; IF+=1.0*GHz)
    {
      device::f = IF;

      // Put in the hot load.
      mix.LO_source.Temp = Thot;
      sd = mix.m.get_term_data();
      Phot = abs(sd.C.read(1, 1));

      // Put in the cold load.
      mix.LO_source.Temp = Tcold;
      sd = mix.m.get_term_data();
      Pcold = abs(sd.C.read(1, 1));

      // Get the IF noise power with 0 K load
      mix.LO_source.Temp = 0.0;
      sd = mix.m.get_term_data();
      Pnoise = abs(sd.C.read(1,1));

      // Calculate the upper and lower sideband noise temperatures.
      sd = mix.get_data();
      tn_usb = Pnoise / norm(sd.S.read(if_port, usb_port));
      tn_lsb = Pnoise / norm(sd.S.read(if_port, lsb_port));

      Y = Phot / Pcold;
      tn_dsb = (Thot - Tcold) / (Y - 1) - Tcold;

      cout << setw(4) << LO/GHz << setw(6)
           << setprecision(2)
           << IF/GHz << setw(9)
           << setprecision(3)
           << mix.current() / (Micro*Amp) << setw(10)
           << sd.SdB(if_port, usb_port) << setw(10)
           << sd.SdB(if_port, lsb_port) << setw(9)
           << tn_usb/Kelvin << setw(9)
           << tn_lsb/Kelvin << setw(9)
           << tn_dsb/Kelvin
           << endl;
    }
    cout << endl;
  }
}
```

G.3 Output

The following simulation results were calculated at a bias voltage of 2.15 mV. It is interesting to note that the double sideband noise temperatures are substantially less than the expected values of half the single sideband noise temperatures. The double sideband noise temperatures listed below were calculated by simulating the standard laboratory technique of measuring the Y-factor $Y \equiv P_h/P_c$ with 295 and 77 K loads, then computing the noise temperature as

$$T_{DSB} = \frac{T_h - T_c}{Y - 1} - T_c \,. \tag{G.1}$$

This formula implicitly assumes that the brightness temperatures of the loads are equal to their physical temperatures, i.e., it assumes the Rayleigh-Jeans approximation. The single sideband noise temperatures listed below should be considered correct since they were not calculated under this false assumption. The calculated double sideband noise temperatures are useful for comparison to lab measurements.

LO	IF	Idc(uA)	Gusb(dB)	Glsb(dB)	Tusb(K)	Tlsb(K)	Tdsb(K)
600.	4.0	62.2	24.8	24.5	284.	305.	134.
600.	5.0	62.2	26.3	25.8	263.	288.	124.
600.	6.0	62.2	26.7	26.2	256.	286.	122.
600.	7.0	62.2	26.0	25.4	259.	295.	125.
600.	8.0	62.2	24.6	24.0	260.	301.	127.
610.	4.0	52.5	24.2	24.0	290.	302.	135.
610.	5.0	52.5	25.7	25.5	267.	281.	124.
610.	6.0	52.5	26.1	25.9	261.	278.	121.
610.	7.0	52.5	25.4	25.1	265.	286.	124.
610.	8.0	52.5	24.0	23.7	267.	290.	126.
620.	4.0	56.4	24.5	24.5	288.	293.	132.
620.	5.0	56.4	26.0	25.9	267.	273.	122.
620.	6.0	56.4	26.4	26.3	263.	269.	120.
620.	7.0	56.4	25.6	25.5	267.	276.	123.
620.	8.0	56.4	24.2	24.1	270.	280.	124.
630.	4.0	63.0	24.9	24.9	287.	288.	130.
630.	5.0	63.0	26.4	26.3	269.	269.	121.
630.	6.0	63.0	26.7	26.7	265.	265.	119.
630.	7.0	63.0	25.9	25.9	270.	271.	122.
630.	8.0	63.0	24.5	24.5	272.	274.	123.
640.	4.0	62.2	24.8	24.8	290.	288.	131.

640.	5.0	62.2	26.2	26.2	271.	269.	121.
640.	6.0	62.2	26.6	26.7	267.	265.	119.
640.	7.0	62.2	25.8	25.9	272.	270.	122.
640.	8.0	62.2	24.4	24.5	275.	272.	123.
650.	4.0	57.9	24.5	24.5	292.	290.	132.
650.	5.0	57.9	25.9	26.0	272.	270.	122.
650.	6.0	57.9	26.3	26.4	268.	265.	120.
650.	7.0	57.9	25.6	25.6	274.	271.	122.
650.	8.0	57.9	24.2	24.2	276.	273.	124.
660.	4.0	53.7	24.2	24.2	294.	294.	133.
660.	5.0	53.7	25.6	25.6	273.	273.	122.
660.	6.0	53.7	26.0	26.1	268.	268.	120.
660.	7.0	53.7	25.3	25.3	274.	274.	123.
660.	8.0	53.7	23.9	23.9	277.	276.	124.
670.	4.0	49.7	24.0	23.9	296.	297.	134.
670.	5.0	49.7	25.4	25.3	273.	275.	123.
670.	6.0	49.7	25.8	25.7	268.	270.	120.
670.	7.0	49.7	24.9	24.9	275.	277.	124.
670.	8.0	49.7	23.5	23.5	278.	280.	125.
680.	4.0	45.0	23.6	23.6	299.	301.	136.
680.	5.0	45.0	25.0	25.0	275.	277.	124.
680.	6.0	45.0	25.3	25.3	270.	271.	121.
680.	7.0	45.0	24.5	24.5	278.	279.	125.
680.	8.0	45.0	23.1	23.1	282.	283.	127.
690.	4.0	39.2	22.9	23.0	313.	308.	141.
690.	5.0	39.2	24.3	24.4	286.	280.	127.
690.	6.0	39.2	24.6	24.8	280.	273.	124.
690.	7.0	39.2	23.8	23.9	290.	282.	128.
690.	8.0	39.2	22.4	22.5	295.	286.	131.
700.	4.0	33.0	21.9	22.0	341.	327.	152.
700.	5.0	33.0	23.2	23.5	306.	291.	135.
700.	6.0	33.0	23.6	23.9	300.	282.	131.
700.	7.0	33.0	22.8	23.1	313.	292.	136.
700.	8.0	33.0	21.3	21.7	320.	295.	139.

Glossary

antenna temperature – A measure of the power spectral density received by a radio telescope. The antenna temperature is equal to the temperature of a hypothetical matched load that would generate the equivalent spectral density in noise; however, antenna temperature is calculated in the Rayleigh-Jeans limit, such that it is proportional to the received power. Antenna temperature is corrected for atmospheric loss and optionally spillover losses in the telescope. See Kutner and Ulich (1981).

brightness temperature – A measure of intensity that originates from the assumption that the intensity of a source is proportional to its temperature. It is equivalent to the temperature that would result if the intensity were inserted into the Rayleigh-Jeans law. This unit is convenient since the brightness temperature of a warm opaque "black" object at low frequency is equal to its physical temperature. Unfortunately, in many cases, especially at submillimeter frequencies, this is not true, and the use of brightness temperature can lead to some confusion.

class – A user-defined data type in object oriented programming that contains both data and functions. See **object oriented programming**.

CO – Carbon monoxide. Depending on the context, when submillimeter astronomers refer to CO, they are usually referring to the $^{12}C^{16}O$ isotopomer.

column density – The number of atoms or molecules in a cloud in a thin column along the line of sight. Column density is usually expressed as the number of particles per centimeter squared.

dBm – A measure of microwave power on a logarithmic scale. Power in dBms equals $10\times\log_{10}$ of the power in milliwatts.

DSB – Double sideband. See **sideband**.

excitation temperature – A measure of the ratio of the population densities of two quantum states in a gas. It is the temperature for which the Boltzmann factor would predict the actual ratio of states. This unit is convenient because it is used to calculate line intensities. In local thermodynamic equilibrium, the excitation temperature is equal to the kinetic temperature. This is often not the case with carbon monoxide in molecular clouds. In some cases, especially with the CO J=1-0 line at 115 GHz, the excitation temperature can be much larger than the kinetic temperature, and can even take on negative values.

GaAs – Gallium Arsenide. A semiconductor used for making high-speed microwave circuits. See **MMIC**.

HEMT – High Electron Mobility Transistor. A type of field-effect transistor (FET) that can provide gain up to very high frequencies ($\sim$100 GHz) with low noise. See Duh et al. (1988).

heterodyne mixer – An electronic device that reduces a signal to a lower frequency by mixing it with a sine wave. Typically, the original signal is called the radio frequency, or RF, the sine wave is called the local oscillator, or LO, and the output is called the intermediate frequency, or IF. The frequencies are related by IF=|RF-LO|.

IF – Intermediate Frequency. See **heterodyne mixer**.

instance – A variable, as opposed to a class or data type. For example, `r1`, `r2`, and `r3` could be instances of `class resistor`. See **object oriented programming**.

interferometer – In this work, refers to an astronomical observatory that uses several radio telescopes to synthesize a single large telescope with very high resolution.

IV curve – A plot of current versus voltage in an electronic device. If the IV curve is not linear, e.g., for a diode, then the device can mix frequencies. See **heterodyne mixer** and **SIS mixer**.

kinetic temperature – The usual meaning of temperature, related to the random kinetic energy of the particles that make up a substance.

LNA – Low-Noise Amplifier. Typically refers to transistor amplifiers at frequencies above about a gigahertz.

LO – Local Oscillator. See **heterodyne mixer**.

LSB – Lower sideband. See **sideband**.

LVG – Large Velocity Gradient. An approximation that takes advantage of the large Doppler shifts in molecular clouds to simplify calculation of the radiation field. In a nutshell, radiative transfer calculations become a local problem when spectral lines in different parts of a system are Doppler shifted to sufficiently different frequencies. See Appendix E.

MMIC – Monolithic Microwave Integrated Circuit. Typically, MMICs are small analog integrated circuits a few millimeters square, fabricated on gallium-arsenide substrates, and often used for microwave amplifiers. See **GaAs**.

NbTiN – Niobium titanium nitride. A high-temperature superconductor ($T_c = 15$ K, compared to niobium at $T_c = 9.5$ K) that is used to make low-noise SIS mixers from about 700 GHz to 1.2 THz because it has a larger energy gap than niobium. See Bumble et al. (2001).

noise temperature – A measure of the noise power generated in a high-frequency circuit. This measure is primarily useful when the Rayleigh-Jeans limit ($T_n \gg h\nu/k_B$) applies. A circuit with noise temperature T_n is equivalent to a noiseless circuit plus a noise power spectral density of $k_B\,T_n$ at its input.

object oriented programming – An approach to computer programming that combines data with functions into user-defined data types called classes, and provides a way for subclasses to inherit functionality from parent classes. For example, SuperMix represents resistors with a class, since a resistor has both data (such as a resistance and a temperature) and functions (such as to calculate its scattering matrix), and inherits properties common to all circuit elements from a device parent class. See Booch (1994).

parsec – A measure of distance equal to 3.26 light-years, or 3.086×10^{16} meters. Abbreviated pc.

PDR – Photodissociation region, sometimes called photon dominated region. Regions where hot, bright stars illuminate opaque molecular clouds with far-ultraviolet radiation. The radiation creates layers of ionized atoms and dissociated molecules, and heats the gas in the region to temperatures in the range of ∼100 to ∼1,000 K. See Hollenbach and Tielens (1997) and Hollenbach and Tielens (1999).

QMMIC – Quasi-MMIC. An analog microwave circuit with all components integrated except the transistors, which are fabricated separately and bump-bonded to the QMMIC substrate. See **MMIC**.

quasi-optical – A term describing systems that treat submillimeter radiation like optical light by focusing it on a detector with a lens instead of with a feedhorn.

RF – Radio Frequency. See **heterodyne mixer**.

sideband – In a heterodyne receiver, the signal frequency can be higher or lower than the local oscillator frequency. Upper sideband (USB) refers to the case when RF>LO, and lower sideband (LSB) when RF<LO. A single sideband (SSB) receiver only detects one of the sidebands, whereas a double sideband (DSB) receiver detects both sidebands simultaneously. See **heterodyne mixer**.

SIS mixer – Superconductor-Insulator-Superconductor mixer. A heterodyne mixer based on an SIS superconducting tunnel junction. The mixing process involves quantum tunneling through the insulating layer. SIS mixers are currently the most sensitive coherent detectors in the range from around 100 GHz to over 1 THz. See Tucker and Feldman (1985), Zmuidzinas and LeDuc (1992), and Bin (1997).

SSB – Single sideband. See **sideband**.

USB – Upper sideband. See **sideband**.

velocity – Since the shape of spectral lines in molecular clouds is typically determined by Doppler shifts, spectra are often plotted as functions of Doppler velocity rather than frequency. Spectral lines in galaxies are typically hundreds of kilometers per second wide.

WASP – Wideband Analog SPectrometer. A lag correlation spectrometer being developed at the University of Maryland that has a moderate number of channels (128) and can be configured for large frequency coverage, normally 4 GHz. See Harris and Zmuidzinas (2001).

Bibliography

Agilent Technologies. http://www.agilent.com.

ALMA web page. http://www.alma.nrao.edu.

Ansoft Corporation. http://www.ansoft.com.

Belitsky, V. Y., S. W. Jacobsson, L. V. Fileppenko, C. Holmstedt, V. P. Koshelets, and E. L. Kollberg (1995). Fourier transform spectrometer studies (300 – 1000 GHz) of Nb-based quasi-optical SIS detectors. *IEEE Trans. Applied Superconductivity* **5**, 3445–3451.

Bin, M. (1997). *Low-Noise Terahertz Niobium SIS Mixers*. Ph.D. thesis, California Institute of Technology.

Blum, E. (1959). Sensibilité des radiotélescopes et récepteurs à correlation. *Annales d'Astrophysique* **22**, 139–163.

Bode, H. W. (1945). *Network Analysis and Feedback Amplifier Design*. New York: Van Nostrand.

Booch, G. (1994). *Object-Oriented Analysis and Design*. Menlo Park, California: Benjamin/Cummings.

Bosma, H. (1967). On the theory of linear noisy systems. *Philips Res. Repts. Suppl.* **10**.

Brouillet, N. and P. Schilke (1993). The clouds of M82 I. HCN in the South-West part. *Astronomy and Astrophysics* **277**, 381–396.

Bumble, B., H. G. LeDuc, J. A. Stern, and K. G. Megerian (2001). Fabrication of Nb / Al-N_x / NbTiN junctions for SIS mixer applications. *IEEE Trans. Applied Superconductivity* **11**, 76–79.

Callen, H. B. and T. A. Welton (1951). Irreversibility and generalized noise. *Phys. Rev.* **83**, 34–40.

Carlstrom, J. (1988). *The Interstellar Medium of a Starburst Galaxy; Millimeter Interferometric Observations of M82*. Ph.D. thesis, University of California at Berkeley.

Carlstrom, J. E., R. L. Plambeck, and D. D. Thornton (1985). A continuously tunable 65–115 GHz Gunn oscillator. *IEEE Trans. Microwave Theory Tech.* **33**(7), 610–619.

Chattopadhyay, G., D. Miller, H. G. LeDuc, and J. Zmuidzinas (2000). A dual-polarized quasi-optical SIS mixer at 550 GHz. *IEEE Trans. Microwave Theory Tech.* **48**(10), 1680–1686.

Colbert, J. W., M. A. Malkan, P. E. Clegg, P. Cox, J. Fischer, S. D. Lord, M. Luhman, S. Satyapal, H. A. Smith, L. Spinoglio, G. Stacey, and S. J. Unger (1999). ISO LWS spectroscopy of M82: a unified evolutionary model. *Astrophysical Journal* **511**, 721–729.

Devyatov, I. A., L. S. Kuzmin, K. K. Likharev, V. V. Migulin, and A. B. Zorin (1986). Quantum-statistical theory of microwave detection using superconducting tunnel junctions. *J. Appl. Phys.* **60**, 1808–1828.

Dickman, R. L. (1978). The ratio of carbon monoxide to molecular hydrogen in interstellar dark clouds. *Astrophysical Journal Supplement Series* **37**, 407–427.

Dobrowolski, J. A. and W. Ostrowski (1996). *Computer-Aided Analysis, Modeling, and Design of Microwave Networks*. Boston: Artech House.

Duh, K. H. G., M. W. Pospieszalski, W. F. Kopp, P. Ho, A. A. Jabra, P. C. Chao, P. M. Smith, L. F. Lester, J. M. Ballingall, and S. Weinreb (1988). Ultra-low-noise cryogenic high-electron-mobility transistors. *IEEE Trans. Electron Devices* **35**, 249–254.

Fano, R. M. (1950a). Theoretical limitations on the broadband matching of arbitrary impedances. *Journal of the Franklin Institute* **249**, 57–83.

Fano, R. M. (1950b). Theoretical limitations on the broadband matching of arbitrary impedances. *Journal of the Franklin Institute* **249**, 139–154.

Faris, J. J. (1967). Sensitivity of a correlation radiometer. *Journal of Research of the National Bureau of Standards – C* **71C**, 153–170.

Fixsen, D. J., C. L. Bennett, and J. C. Mather (1999). COBE far infrared absolute spectrophotometer observations of Galactic lines. *Astrophysical Journal* **526**, 207–214.

Flower, D. R. (2001). The rotational excitation of CO by H_2. *J. Phys. B: At. Mol. Opt. Phys.* **34**, 2731–2738.

Flower, D. R. and J. M. Launay (1985). Rate coefficients for the rotational excitation of CO by ortho- and para-H_2. *Monthly Notices of the Royal Astronomical Society* **214**, 271–277.

Freedman, W. L., S. M. Hughes, B. F. Madore, J. R. Mould, M. G. Lee, P. Stetson, R. C. Kennicutt, A. Turner, L. Ferrarese, H. Ford, J. A. Graham, R. Hill, J. G. Hoessel, J. Huchra, and G. D. Illingworth (1994). The Hubble Space Telescope Extragalactic Distance Scale Key Project. I. The discovery of Cepheids and a new distance to M81. *Astrophysical Journal* **427**, 628–655.

Frerking, M. A., W. D. Langer, and R. W. Wilson (1982). The relationship between carbon monoxide abundance and visual extinction in interstellar clouds. *Astrophysical Journal* **262**, 590–605.

Gaidis, M. C., H. G. LeDuc, M. Bin, D. Miller, J. A. Stern, and J. Zmuidzinas (1996). Characterization of low-noise quasi-optical SIS mixers for the submillimeter band. *IEEE Trans. Microwave Theory Tech.* **44**, 1130–1139.

Goldreich, P. and J. Kwan (1974). Molecular clouds. *Astrophysical Journal* **189**, 441–453.

Güsten, R. (1989). Gas and dust in the inner few degrees of the Galaxy. In M. Morris (Ed.), *The Center of the Galaxy*. Dordrecht: Kluwer.

Harris, A. I., R. E. Hills, J. Stutzki, U. U. Graf, A. P. G. Russel, and R. Genzel (1991). First observations of the CO J=6−5 transition in starburst galaxies. *Astrophysical Journal* **382**, L75–L79.

Harris, A. I., J. Stutzki, R. Genzel, J. B. Lugten, G. J. Stacey, and D. T. Jaffe (1987). Submillimeter and far-infrared spectroscopy of M17 and S106: UV-heated, quiescent molecular gas? *Astrophysical Journal* **322**, L49–L54.

Harris, A. I. and J. Zmuidzinas (2001). A wideband lag correlator for heterodyne spectroscopy of broad astronomical and atmospheric spectral lines. *Review of Scientific Instruments* **72**, 1531–1538.

Haus, H. A. and R. B. Adler (1958). Optimum noise performance of linear amplifiers. *Proceedings of the IRE* **46**, 1517–1533.

Hollenbach, D. J. and A. G. G. M. Tielens (1997). Dense photodissociation regions (PDRs). *Annu. Rev. Astron. Astrophys.* **35**, 179–215.

Hollenbach, D. J. and A. G. G. M. Tielens (1999). Photodissociation regions in the interstellar medium of galaxies. *Reviews of Modern Physics* **71**, 173–230.

Hughes, D. H., W. K. Gear, and E. I. Robson (1994). The submillimetre structure of the starburst nucleus in M82: a diffraction-limited 450-μm map. *Monthly Notices of the Royal Astronomical Society* **270**, 641–649.

Kaufman, M. J., M. G. Wolfire, D. J. Hollenbach, and M. L. Luhman (1999). Far-infrared and submillimeter emission from Galactic and extragalactic photodissociation regions. *Astrophysical Journal* **527**, 795–813.

Kawamura, J., J. Chen, D. Miller, J. Kooi, J. Zmuidzinas, B. Bumble, H. G. LeDuc, and J. A. Stern (1999). Low-noise submillimeter-wave NbTiN superconducting tunnel junction mixers. *Applied Physics Letters* **75**, 4013–4015.

Ke, Q. and M. Feldman (1992). Reflected power effects in computer simulations using the quantum theory of mixing. *1992 IEEE MTT-S International Microwave Symposium Digest* **43**, 1425–1428.

Kennicutt, R. C. (1998). The global Schmidt law in star-forming galaxies. *Astrophysical Journal* **498**, 541–552.

Kerr, A. R. (1995). Some fundamental and practical limits on broadband matching to capacitive devices, and the implications for SIS mixer design. *IEEE Trans.*

Microwave Theory Tech. **43**, 2–13.

Knapp, G. R., T. G. Phillips, P. J. Huggins, R. B. Leighton, and P. G. Wannier (1980). Detection of the CO J=2→1 line in M82 and IC 342. *Astrophysical Journal* **240**, 60–64.

Kooi, J. W., F. Rice, G. Chattopadhyay, S. Sundarum, S. Weinreb, and T. G. Phillips (1999). Regarding the IF output conductance of SIS tunnel junctions and the integration with cryogenic InP MMIC amplifiers. *Proceedings, Tenth International Symposium on Space Terahertz Technology*, 100–117.

Kooi, J. W., P. L. Schaffer, B. Bumble, H. LeDuc, and T. G. Phillips (1998). Heterodyne instrumentation at the CSO. *Proc. SPIE* **3357**, 22–32.

Kooi, J. W., C. K. Walker, H. G. LeDuc, P. L. Schaffer, T. R. Hunter, D. J. Benford, and T. G. Phillips (1994). A low-noise 665 GHz SIS quasi-particle wave-guide receiver. *International Journal of Infrared and Millimeter Waves* **15**, 477–492.

Kutner, M. L. and B. L. Ulich (1981). Recommendations for calibration of millimeter-wavelength spectral line data. *Astrophysical Journal* **250**, 341–348.

Lacy, J. H., R. Knacke, T. R. Geballe, and A. T. Tokunaga (1994). Detection of absorption by H_2 in molecular clouds: a direct measurement of the H_2:CO ratio. *Astrophysical Journal* **428**, L69–L72.

Lo, K. Y., K. W. Cheung, C. R. Masson, T. G. Phillips, S. L. Scott, and D. P. Woody (1987). Molecular gas in the starburst nucleus of M82. *Astrophysical Journal* **312**, 574–591.

Loiseau, N., N. Nakai, Y. Sofue, R. Wielebinski, H.-P. Reuter, and U. Klein (1990). ^{12}CO (J=2–1) mapping of M82. *Astronomy and Astrophysics* **228**, 331–340.

Lord, S. D., D. J. Hollenbach, M. R. Haas, R. H. Rubin, S. W. J. Colgan, and E. F. Erickson (1996). Interstellar properties of a dual nuclear starburst: Far-infrared spectroscopy of M82. *Astrophysical Journal* **465**, 703–716.

Mao, R. Q., C. Henkel, A. Schulz, M. Zielinsky, R. Mauersberger, H. Störzer, T. L. Wilson, and P. Gensheimer (2000). Dense gas in nearby galaxies III.

CO submillimeter line emission from the starburst galaxy M82. *Astronomy and Astrophysics* **358**, 433–450.

Mattis, D. C. and J. Bardeen (1958). Theory of the anomalous skin effect in normal and superconducting metals. *Phys. Rev.* **111**, 412–417.

National Instruments. http://www.natinst.com/labview.

Neininger, N., M. Guélin, U. Klein, S. García-Burillo, and R. Wielebinski (1998). ^{13}CO at the centre of M82. *Astronomy and Astrophysics* **339**, 737–744.

Nishimura, T., F. J. Low, and R. F. Kurtz (1980). Far-infrared survey of the Galactic plane. *Astrophysical Journal* **239**, L101–L106.

Noguchi, T., S. C. Shi, and J. Inatani (1995). Parallel connected twin SIS junctions for millimeter and submillimeter-wave mixers – analysis and experimental verification. *IEICE Trans. Elect.* **E78C**, 481–489.

Padin, S. and G. G. Ortiz (1991). A cooled 1–2 GHz balanced HEMT amplifier. *IEEE Trans. Microwave Theory Tech.* **39**, 1239–1243.

Padin, S., D. P. Woody, J. A. Stern, H. G. LeDuc, R. Blundell, C. Y. E. Tong, and M. W. Pospieszalski (1996). An integrated SIS mixer and HEMT IF amplifier. *IEEE Trans. Microwave Theory Tech.* **44**(6), 987–990.

Pierce-Price, D., J. S. Richer, J. S. Greaves, W. S. Holland, T. Jenness, A. N. Lasenby, G. J. White, H. E. Matthews, D. Ward-Thompson, W. R. F. Dent, R. Zylka, P. Mezger, T. Hasegawa, T. Oka, A. Omont, and G. Gilmore (2000). A deep submillimetre survey of the Galactic Centre. *Astrophysical Journal* **545**, L121–L125.

Pöpel, R. (1989). Surface impedance and reflectivity of superconductors. *J. Appl. Phys.* **66**, 5950–5957.

Pospieszalski, M. W. (1989). Modeling of noise parameters of MESFET's and MODFET's and their frequency and temperature dependence. *IEEE Trans. Microwave Theory Tech.* **37**, 1340–1350.

Pospieszalski, M. W., S. Weinreb, R. D. Norrod, and R. Harris (1988). FET's and HEMT's at cryogenic temperatures — Their properties and use in low-noise amplifiers. *IEEE Trans. Microwave Theory Tech.* **36**, 552–559.

Predmore, C. R., N. R. Erickson, G. R. Hugeunin, and P. F. Goldsmith (1985). A continuous comparison radiometer at 97 GHz. *IEEE Trans. Microwave Theory Tech.* **33**, 44–51.

Press, W. H., S. A. Teukolsky, W. T. Vetterling, and B. P. Flannery (1992). *Numerical Recipes in C*. New York: Cambridge University Press.

Rice, F., J. Ward, G. Chattopadhyay, and J. Zmuidzinas (1999). Fast harmonic balance of SIS mixers with multiple junctions and superconducting circuits. *Proceedings, Tenth International Symposium on Space Terahertz Technology*, 282–297.

Rogers Corporation. http://www.rogers-corp.com.

Sanders, D. B., P. M. Solomon, and N. Z. Scoville (1984). Giant molecular clouds in the galaxy. I. the axisymmetric distribution of H_2. *Astrophysical Journal* **276**, 182–203.

Scoville, N. Z. and P. M. Solomon (1974). Radiative transfer, excitation, and cooling of molecular emission lines (CO and CS). *Astrophysical Journal* **187**, L67–L71.

Shen, J. and K. Y. Lo (1995). Locations of starbursts in M82. *Astrophysical Journal* **445**, L99–L103.

Shi, S. C. and T. Noguchi (1998). Low-noise superconducting receivers for millimeter and submillimeter wavelengths. *IEICE Trans. Elect.* **E81C**, 1584–1594.

Stroustrup, B. (1997). *The C++ Programming Language*. Reading, Massachusetts: Addison-Wesley.

Sutton, E. C., C. R. Masson, and T. G. Phillips (1983). The distribution of the CO J=2–1 emission from M82. *Astrophysical Journal* **275**, L49–L53.

Telesco, C. M. and D. Y. Gezari (1992). High-resolution 12.4 micron images of the starburst region in M82. *Astrophysical Journal* **395**, 461–465.

Tong, C. Y. E., L. Chen, and R. Blundell (1997). Theory of distributed mixing and amplification in a superconducting quasi-particle nonlinear transmission line. *IEEE Trans. Microwave Theory Tech.* **45**(7), 1086–1092.

Tucker, J. R. and M. J. Feldman (1985). Quantum detection at millimeter wavelengths. *Reviews of Modern Physics* **57**(4), 1055–1113.

Wedge, S. (1991). *Computer-Aided Design of Low Noise Microwave Circuits*. Ph.D. thesis, California Institute of Technology.

Wedge, S. W. and D. B. Rutledge (1991). Noise waves and passive linear multiports. *IEEE Microwave Guided Wave Letters* **1**, 117–119.

Wedge, S. W. and D. B. Rutledge (1992). Wave techniques for noise modeling and measurement. *IEEE Trans. Microwave Theory Tech.* **40**, 2004–2012.

Weiß, A., N. Neininger, S. Hüttemeister, and U. Klein (2001). The effect of violent star formation on the state of the molecular gas in M82. *Astronomy and Astrophysics* **365**, 571–587.

Wengler, M. J. and D. P. Woody (1987). Quantum noise in heterodyne detection. *IEEE J. Quantum Electronics* **23**, 613–622.

Wild, W., A. I. Harris, A. Eckart, R. Genzel, U. U. Graf, J. M. Jackson, A. P. G. Russell, and J. Stutzki (1992). A multi-line study of the molecular interstellar medium in M82's starburst nucleus. *Astronomy and Astrophysics* **265**, 447–464.

Withington, S. and E. L. Kollberg (1989). Spectral-domain analysis of harmonic effects in superconducting quasiparticle mixers. *IEEE Trans. Microwave Theory Tech.* **37**, 231–238.

Young, J. S. and N. Z. Scoville (1984). Molecular clouds in M82. *Astrophysical Journal* **287**, 153–166.

Yun, M. S., P. T. P. Ho, and K. Y. Lo (1993). HI streamers around M82: tidally disrupted outer gas disk. *Astrophysical Journal* **411**, L17–L20.

Zimmermann, P. Radiometer Physics.

Zmuidzinas, J. and H. G. LeDuc (1992). Quasi-optical slot antenna SIS mixers. *IEEE Trans. Microwave Theory Tech.* **40**, 1797–1804.

Zmuidzinas, J., H. G. LeDuc, J. A. Stern, and S. R. Cypher (1994). Two-junction tuning circuits for submillimeter SIS mixers. *IEEE Trans. Microwave Theory Tech.* **42**, 698–706.

Zmuidzinas, J., N. G. Ugras, D. Miller, M. Gaidis, H. G. LeDuc, and J. A. Stern (1995). Low-noise slot antenna SIS mixers. *IEEE Trans. Applied Superconductivity* **5**, 3053–3056.